Ph.D. in Water and Territory Management Engineering (25th cycle)

POLITECNICO DI TORINO
Department of Structural, Geotechnical and Building Engineering

May 2013

Design of an experimental procedure and set up for the detection of ice segregation phenomena in rock by acoustic emissions

....
Silvia Duca
Author

....
Prof. Claudio Scavia (Politecnico di Torino)
Supervisor

....
Prof. Luigi Sambuelli (Politecnico di Torino)
Co-Supervisor

....
Ing. Massimiliano Mattone (Politecnico di Torino)
Co-Supervisor

....
Prof. Claudio Scavia
Head of the Ph.D. Programme in Water and Territory Management Engineering

a Clara

Abstract

Large slope failures in steep alpine bedrock present a significant geological hazard in many high mountain areas throughout the world. An increased number of periglacial rock falls have been identified in recent decades as a consequence of climate changes. Starting from the Matterhorn site field observations (Italy), a comparative analysis between temperature spatial-temporal distribution and microseismic activity, showed that the hypocentres seemed to be localized close to the permafrost boundary. Ice segregation has been interpreted as one of the mechanisms involved in high mountain bedrock degradation and its associated instability. The aim of this research is to design and set up a down scaled physical simulation of this frost weathering mechanism. Ice segregation phenomenon has been analyzed in depth through numerical simulations and laboratory tests. Fully coupled thermo-hydro-mechanical analyses have been carried out using the FEM code CODE_BRIGHT, by coupling a description of transient heat and mass transfer in porous, freezing media. These studies have addressed the mechanics of ice growth, particularly the role of the premelted films in lens growth, in order to do some prediction of the timing and depth of potential macrocrack originating perpendicular to the water flow from ice segregation processes. Uncoupled numerical analyses have also been performed using the FEM code ABAQUS: they highlighted how steady temperature gradients play a fundamental role in crack propagation and they permitted to chose the temperature interval that would maximize the frost cracking mechanism in the rock sample. Finally, two long-term freezing tests has been set up: the first experimental test was aimed to reproduce the ice lens growth mechanism due to the onset of ice segregation processes at the interface active layer-permafrost table, building up a physical model. During the second trial, acoustic emission monitoring system has been installed, deepening the understanding of the processes operating in evolving fault zone due to the ice lens growth.

Acknowledgments

"Scrivere può essere un'attività solitaria, mentre pensare non lo è". Un grande regalo dell'esperienza di dottorato è stato proprio il fatto di aver avuto l'opportunità di riflettere con persone di enorme valore intellettuale, scientifico e morale, e prendere esempio da loro. Questa tesi non sarebbe la stessa senza la numerosa squadra di (talvolta inconsapevoli) collaboratori. Quello che segue è il mio modo di ringraziare tutte le persone che hanno contribuito direttamente a questo lavoro. Numerosi sono coloro la cui competenza ha forgiato il mio modo di pensare o mi ha spinto a cambiarlo.

Ringrazio prima di tutto i miei tre tutori. Il Professor Scavia per avermi proposto questa stimolante attività di ricerca. Il Professor Sambuelli, non solo per aver contribuito a portare a compimento questo lavoro, ma anche per essere stato fonte di ispirazione per alcuni dei suoi spunti migliori, sollecitando una continua riflessione critica. L'Ingegner Mattone ha fatto di tutto per tirare fuori il meglio dal mio lavoro (e da me). Che ci sia riuscito o meno, io ho imparato moltissimo da lui, e gli sono grata per questo, e apprezzo enormemente il suo impegno, gli stimoli scientifici e le impareggiabili chiaccchierate.

I mesi trascorsi a Barcellona sono stati davvero fondamentali; a questo proposito vorrei ringraziare il Professor Alonso e il Professor Olivella, dai quali ho imparato veramente molto e mi sento fortunata per aver potuto lavorare con loro. Ringrazio anche la Dottoressa Casini, che è stata davvero preziosa, e i miei colleghi catalani, Natàlia, Alba, Claudia e Victor, per i loro consigli e per la loro compagnia.

Grazie alla Professoressa Marini e all'Ingener Bellopede, che mi hanno aiutata con il loro brillante entusiasmo e passione nella caratterizzazione dei provini utilizzati nella sperimentazione.

Ringrazio sinceramente il Professor Maurino che mi ha accolta nel suo laboratorio di chimica, e il Dottor Sordello, il cui aiuto è stato fondamentale

Table of contents

Chapter 1

Introduction

1.1 Motivation

Degrading permafrost in rock walls is considered to be an increasing hazard in alpine environments due to both, rockfall activity and slow rock deformation endangering infrastructure and potentially causing casualties ([81] Krautblatter et al., 2013). The increasing importance of hydro-electric power generation and storage in high topography settings and the high-alpine winter and adventure tourism, increases the vulnerability to permafrost rock slope failure and requires improved assessment and monitoring strategies for permafrost rock walls ([61] Haeberli et al., 1997).

It has been postulated, that permafrost distribution can significantly influence the stability of permafrost rock slopes and it responds quickly to climatic fluctuations ([45] Fischer & Huggel, 2008). Detachment zones of rock-ice avalanches indicate thermal disturbances caused by the interaction of permafrost, glacial ice, and climate changes.

Krautblatter (2013) explained how permafrost dynamics influence rock slope stability due to increasing shear stresses and reducing shear resistance. Fischer et al. (2010) modelled the effects of enhanced hydrostatic pressure due to a perched water level sealed by permafrost ([80] Krautblatter et al., 2010). Upward freezing due to ice segregation could cause propagating ice-filled fractures, which may provide a slip plane during thawing ([93] Matsuoka & Murton, 2008). While macrogelivation (frost wedging) is postulated to operate in rock discontinuities close to the surface ([92] Matsuoka, 2001),

microgelivation (i.e. ice segregation) could physically operate in several meters depth, where permafrost is found in Alpine environments.

In this context, the processual and mechanical understanding of the permafrost-related failure mechanisms is also a crucial issue to decipher its impact among multiple other factors that influence rock slope stability, as explained in Chapter 2.

Monitoring rock instabilities and deformation in high elevation slopes was proposed as one of the activities of the Interreg IIIA Alcotra project n. 196 "PERMAdataROC", in which microseismic (MS) investigation technique was adopted as a measure of the stability. Matterhorn peak was selected as instrumented site, where a thermometric monitoring system was coupled with the MS network, assuring the possibility of performing crossed analysis.

The original idea of the study was that rock mass instabilities could be related to the failure of intact rock bridges connecting non-persistent discontinuities, often conditioned by subcritical crack growth: from a mechanical point of view, the presence of permafrost can increase shear stress due to changing water pressure and cryostatic pressure, provided by ice segregation phenomena.

1.2   Aim of the research

Starting from the hypothesis derived from field observations at the Matterhorn site and described in Chapter 3, several approaches to study the ice segregation phenomenon in rock will be presented in the present dissertation.

The aim of this research has been to design and set up a down scaled physical simulation of this frost weathering mechanism: ice segregation phenomenon has been analyzed in depth through numerical simulations and laboratory tests.

Numerical analysis have been performed in order to validate the experimental procedure as well as to evaluate some predictions (Chapter 4). These studies have addressed the mechanics of ice growth, particulary the role of the premelted films in lens growth, and the fracturing mechanism in rock under steady temperature gradients.

Due to the complexity of the phenomena involved, a pilot trial has been necessary in order to test the methodology and to identify the difficulties connected with the application of thermal cycles to a saturated rock sample, monitoring microcrack activities. The experimental laboratory prototype has been modeled and set up, as shown in Chapter 5.

During the test design, many efforts have been spent for the sample characterization and preparation: in Chapter 6 the ways in which the sample has been treated prior to the experimental set up are explained in details.

Another sensitive point of the laboratory procedure is to monitor with acoustic emission techniques the microcracks propagation induced by ice growth. The importance of a correct receiver array distribution and the details of the adopted source location approach have been evidenced in Chapter 7.

Finally, two laboratory tests concerning the verification of ice segregation mechanism and resulting crack growth in hard, intact rock, have been presented in Chapter 8. The first experimental test was aimed to reproduce the ice lens growth mechanism due to the onset of ice segregation processes at the interface active layer-permafrost table. During the second trial, acoustic emission monitoring system has been installed, yielding valuable new insights into the processes operating in evolving fault zone due to the ice lens growth.

Chapter 2

Permafrost characteristics and its response to climate changes

2.1 Permafrost: definitions and classification

The term permafrost, also known as perennially frozen ground, was first defined by Miller (1947): "Permanently frozen ground or permafrost is defined as a thickness of soil or other superficial deposit, or even of bedrock, at a variable depth beneath the surface of the earth, in which a temperature below freezing has existed continually for a long time" ([97] Miller, 1978).

Brown and Kupsch (1974) defined permafrost as soil or rock having temperatures below 0°C during at least two consecutive winters and the intervening summer: that is, permafrost is defined purely on the basis of temperature irrespective of texture, water content or lithological character ([22] Brown & Kupsch, 1974). The difference to non-frozen ground and the practical relevance of permafrost, however, comes with the ice contained in the underground (e.g., pore ice, ice-filled fractures, ice lenses), which can significantly change its characteristics (geotechnical properties, water permeability, etc.) ([105] Noetzli, 2008).

The formation and existence of this frozen condition in earth materials is controlled by climate and various terrain factors. Temperature conditions

required for the existence of permafrost are illustrated by temperature profile shown in Figure 2.1.
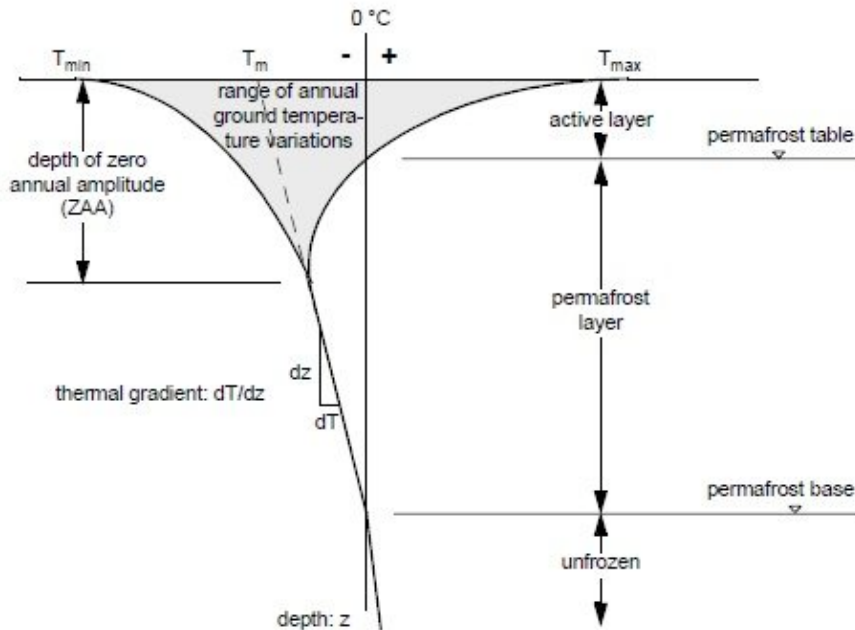
Figure 2.1: Temperature profile in permafrost ([10] Andersland & Ladanyi, 2004).

The thickness of the frozen ground is determined by the mean annual surface temperature (T_m) and the heat flow from the earth's interior corresponding to the geothermal gradient. In Figure 2.1, the active layer is shown at the surface and unfrozen soil exists below the permafrost base, where temperatures are equal or greater than 0°C ([10] Andersland & Ladanyi, 2004).

The top layer of the ground in which temperature fluctuates above and below 0°C during the year, is defined as the active layer and it extends downward to the permafrost table. Its thickness depends on many factors, including the severity of the winter temperatures (freezing index), soil and rock types, ground moisture content, snow cover, surface vegetation, drainage, and the degree and the orientation of the slopes ([10] Andersland & Ladanyi, 2004).

Seasonal frost penetration is associated with an annual thermal cycle where the heat extracted in the winter is largely that entering the ground in the summer. The depth of freezing (0°C isotherm) is dependent on the surface freezing index and creates a temperature profile, as shown in Figure 2.1. Below the level of zero annual temperature amplitude, ground temperature will increase with depth an amount dependent on the local geothermal gradient ([10] Andersland & Ladanyi, 2004). The freezing and thawing of the active layer acccours either on diurnal basis, or on seasonal basis: the rate of the spring thaw influences the spring runoff while the autumn freeze-back controls the nature of frost heaving and ice segregation mechanisms (Figure 2.2).
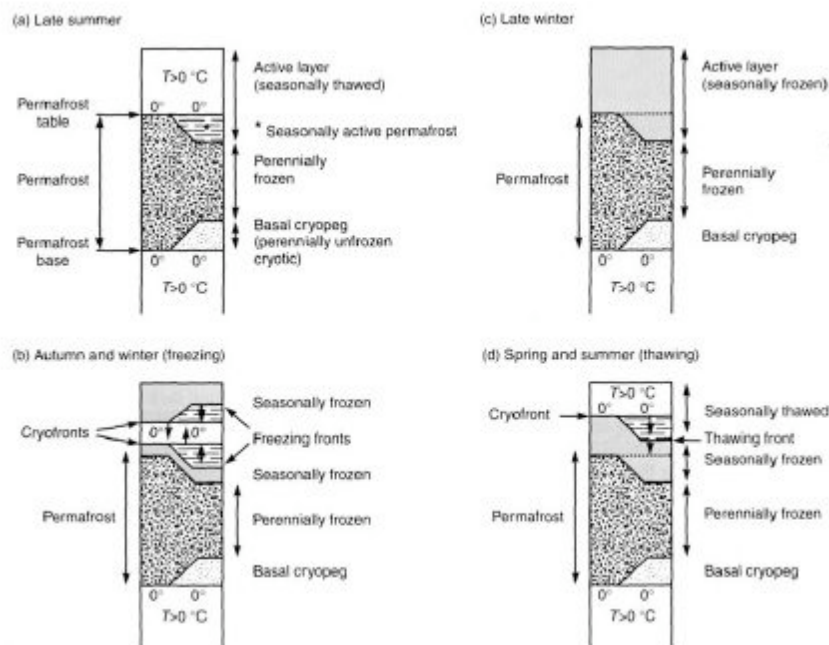
Figure 2.2: Seasonal changes in the active layer ([44] French, 1988).

Usually the spring thaw occurs quickly during the first 4-5 weeks in which air temperatures are above 0°C. Thawing is one sided, from surface downwards. Ground thermal regimes are also closely related to snow thickness and density

([44] French, 1988).

Autumn freeze-back is an equally complex process: in regions underlain by continuous permafrost, freezing is two-sided, occurring both downwards from the surface and upwards from the perennially frozen ground beneath (permafrost table). Moreover the freezing period is much longer and may persist for 6-8 weeks. During the majority of this time the soil or the rock remain in a near isothermal condition, sometimes referred to as the "zero curtain". This phenomenon results from release of latent heat upon freezing, thereby retarding the drop in temperature. Initially, freezing progresses at a slow rate from the surface downwards, but then dramatically speeds up at depth. This is because of the occurrence of upward freezing from the permafrost beneath (Figure 2.2 (a)) and the fact that moisture decreases with depth since water is initially drawn upwards to the freezing plane (Figure 2.2 (b)), thereby preferentially increasing the latent heat effects in the surface layers ([44] French, 1988).

In contrast to the so called arctic, antarctic or polar permafrost, mountain permafrost can be found under moderate climatic conditions at higher elevations.

Mountain permafrost, or alpine permafrost, simply is permafrost in high-mountain areas and is characterized by the influence of mountain topography on its properties. For high mountains, numerous definitions exist, which generally relate to elevation, steep slopes, rocky terrain, and the presence of snow and ice ([105] Noetzli, 2008).

At high elevations in mid-latitude mountains, permafrost is widespread where the mean annual air temperature is below -3°C . It often exists far below the altitudes to which glaciers extend, and even below the tree line in continental areas. Mountain permafrost exists in different forms: in steep bedrock, in rock glaciers, in debris deposited by glaciers or in vegetated soil, and contains variable amounts of ice. Since topography causes large variability in local climate, snow cover, and ground and surface properties through the processes of erosion, transport and deposition, mean annual ground temperatures in mountain regions can vary by 5-8°C over distances as small as 100m (Figure 2.3). For this reason, the distribution and characteristics of permafrost in mountain regions are very patchy ([125] Romanovsky & Osterkamp, 1995).

Steep terrain and strong variability in surface temperatures are typical of mountain permafrost. The cross section in the foreground shows the complex distribution of subsurface temperatures characteristic of mountains, with the isotherms (lines linking points of equal temperature) nearly vertical in the ridge of the mountain. In the background, the colors on the mountain surface illustrate the strong variability in ground temperatures caused by differences

.
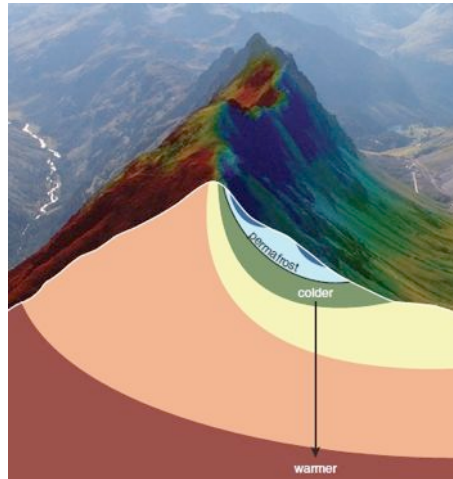
Figure 2.3: Temperatures in a mountain range containing permafrost (blue colors bordered by the black line), ranging from colder (blue) to warmer (red). Source: S. Gruber, photo from Christine Rothenbühler ([125] Romanovsky & Osterkamp, 1995)

in elevation, exposure to the sun, snow cover and ground properties. In the far background, one can only guess at this complex pattern of permafrost distribution because permafrost is invisible at the ground surface ([125] Romanovsky & Osterkamp, 1995).

The definition of permafrost includes all rock systems where ice can persist for at least two years in open and confined space. Ice can occur both in the form of pore ice whether more or less continuous lenses of varying thickness, interspersed with rocky layers and filling the discontinuities (Figure 2.4). Rock permafrost is generally not synonymous with perennially frozen rock as rock often only freezes significantly below the datum freezing point.

The systemic difference between non-permafrost rocks and permafrost rocks is, thus, the perennial presence of ice, that has a number of serious implications on the system ([79] Krautblatter, 2009):

- Ice significantly alters thermal properties of permafrost rocks at the surface and at depth. On the rock surface, ice occurs as snow, unfrozen ice and glacier ice and significantly alters heat exchange due to long- and

9

Figure 2.4: Ice-filled discontinuity (Image Courtesy of U. Morra di Cella).

short-wave radiation and due to sensible and latent heat fluxes. Inside the rock mass, the good thermal conduction of ice in pores and rock discontinuities increases heat flux especially across otherwise air-filled discontinuities. The enormous latent melting energy buffers frozen rock systems at the surface and at depth and can result in persistent high thermal gradients between frozen rock and the atmosphere with effective heat conduction.

- Hydraulic properties of permafrost rocks are affected by the sealing of rock discontinuities and decreased permeability of the intact rock mass. Perched water-tables result in enormous hydrostatic pressures that significantly alter rock stability. Ice effectively stores water in permafrost rocks and dispenses water in summer and autumn with implications for weathering, ice segregation and rock stability.

- Mechanical properties undergo significant alterations around the freezing point. Compressive and tensile rock mass strength in frozen rocks strongly decreases with increasing temperature close to thawing point. Ice mechanical properties of deformation and cracking become increasingly important. The presence of ice creates cohesive connections in rock discontinuities which are otherwise often absent. Ice segregation may play an important role due to the dilatation and dislocation of shear surfaces.

- The geomorphological systems of permafrost rocks is significantly

different from other rock environments. While temperate rocks are affected by changing climate mostly at the surface due to alterations in weathering, mechanical and hydraulic properties of permafrost rocks in all depths undergo permanent changes due to thermal signals of climatic fluctuations. The described sensitivity in combination with long relaxation times in respect to the slow speed of thermal conduction turns permafrost rocks into a highly path-dependent system. The interplay of slow and reversible heat conduction processes and the rapid, irreversible heat transfers evoked by cleft water in an anisotropic medium causes complex behavior that is not exactly predictable in deterministic terms.

2.2 Permafrost distribution

About one fifth to one fourth of the Earth's land area is currently underlaid by permafrost, according to the Circum-Arctic Map of Permafrost and Ground Ice Conditions, which was prepared under the auspices of the International Permafrost Association (IPA) (Figure 2.5).

Depending on the model applied, a 25-44% reduction in total area is expected for the next century assuming a 2°C increase in mean global temperature. In particular, this retreat happens in regions with small permafrost thicknesses and areas of discontinuous permafrost. As a consequence, the lower limit of permafrost will move up to higher altitudes in regions of high-elevation or to more extreme latitudes mainly around the northern hemisphere ([11] Arenson, 2002).

Awareness of the presence of perennially frozen grounds is mainly limited to the northern hemisphere, where large areas are covered by it. Some permafrost can be found also in the southern circumpolar regions, even though further investigations are necessary.

The climatic environments characterizing the periglacial areas are different: polar desert, tundra, cold continental climate and alpine areas of middle and lower latitudes. All these types are characterized by low precipitations, usually less than 500mm per year (but sometimes up to 1700-2000mm) and the mean annual temperature less than or equal to 3°C ([58] Guglielmin, 2004).

About 6-7% of the permafrost is mountain permafrost. Of that, however, only about 0.2% is in the European Alps, whereas the main part (80.4%) can be found in Asia. Another 19.4% are in the American mountains ([11] Arenson, 2002). Those percentages have to be applied with caution since they may change with the ongoing trend of global warming.
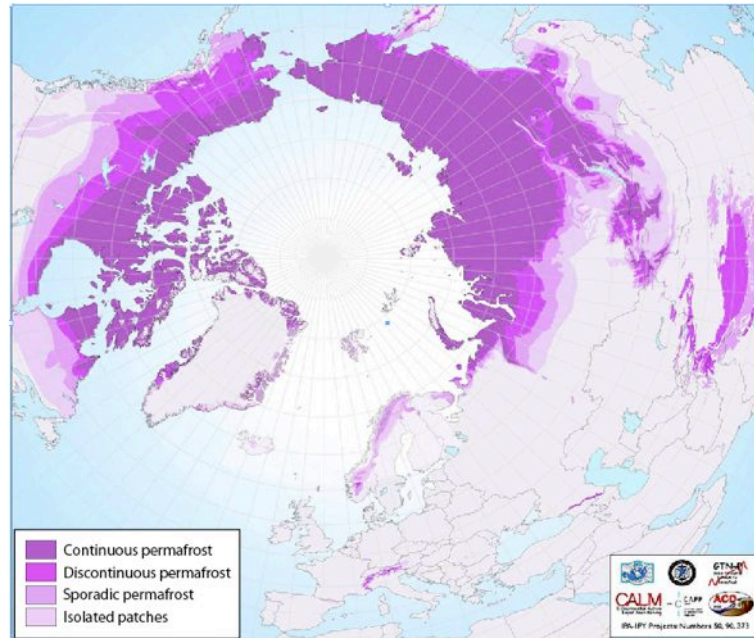
Figure 2.5: Permafrost extent in the Northern Hemisphere (http://ipa.arcticportal.org).

In Italy, permafrost may be present from elevations of about 2100m a.s.l., depending on the exposure of the location. Recent modeling of the permafrost distribution and the research of geomorphological features (which are only present due to the steep environment within mountain permafrost regions, such as rock glaciers, ice core moraines, gelifluction lobes etc.) have allowed the creation of empirical maps of the cryosphere, as shown in Figure 2.6 and Figure 2.7.

The permafrost thickness, which is is the distance between the permafrost table and the permafrost base, is also variable and depends crucially on the thermal properties of the substrate, as well as the surface temperature of course: in Italy the thickness varies from few meters to an average of 20-30m, although in the Stelvio Pass at 3000 m a.s.l. (the only site investigated by deep drilling) it should exceed 230 m ([58] Guglielmin, 2004).
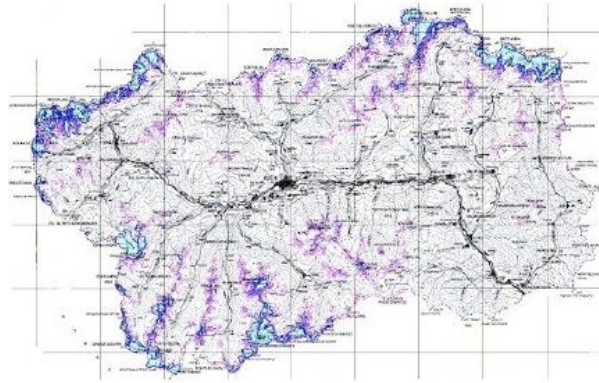
Figure 2.6: Permafrost distribution in Aosta Valley ([58] Guglielmin, 2004).
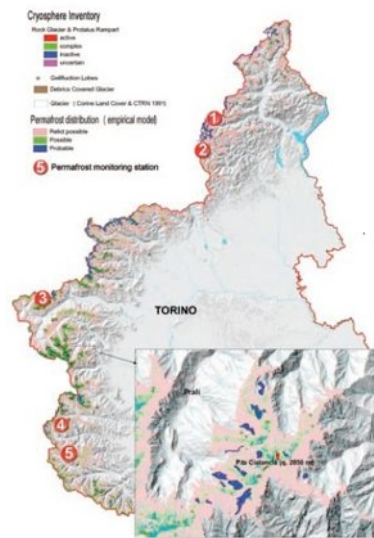
Figure 2.7: Permafrost distribution in Piemonte (http://www.arpa.piemonte.it/).

2.3   Permafrost interactions

Since permafrost is a thermal state, determination of the energy balance to the ground is very important for its modeling and prediction of future changes. Many different factors and effects have major influence on the thermal regime in the ground. The complexity of the interactions between the atmosphere and the active layer, and their influences on the permafrost are shown in Figure 2.8 ([11] Arenson, 2002). A central factor in high mountain permafrost is the effect between the snow cover and the active layer; furthermore, attempts have been made to model the influence of the snow cover on soil freezing as well as analyzing the effect on the soil temperature and the energy balance ([11] (Arenson, 2002).
Kraublatter proposes a conceptual approach to major sources of heterogeneity on active layer dynamics and permafrost distribution on a meter to decameter scale, based on the following assumptions ([79] Kraublatter, 2009), as shown in Figure 2.9 :

- Active layer thickness at the surface decreases with altitude ([54] Gruber et al., 2004).

- Unfrozen glaciers and cold glaciers are situated directly on perennially frozen rocks.

- Debris accumulations in rock faces have maximum angles of 45° (max. angle of repose) and are therefore snow-covered in winter. They usually do not consist of large blocks as preferably small particles accumulate on small and inclined ledges.

- Warm glaciers conduct massive advective heat transfer with adjacent rocks.

- The active layer can be considered as "semiconductive" since thermal conduction in the frozen intact rock mass and across ice-filled rock discontinuities performs better than in unfrozen rock and across air-filled rock discontinuities.

In addiction, there are effects of unfrozen water on the active layer and permafrost: the unfrozen water brings in a spatially distributed latent heat and therefore changes the thermal properties of the active layer and, if the water has the possibility to flow, through the permafrost body.
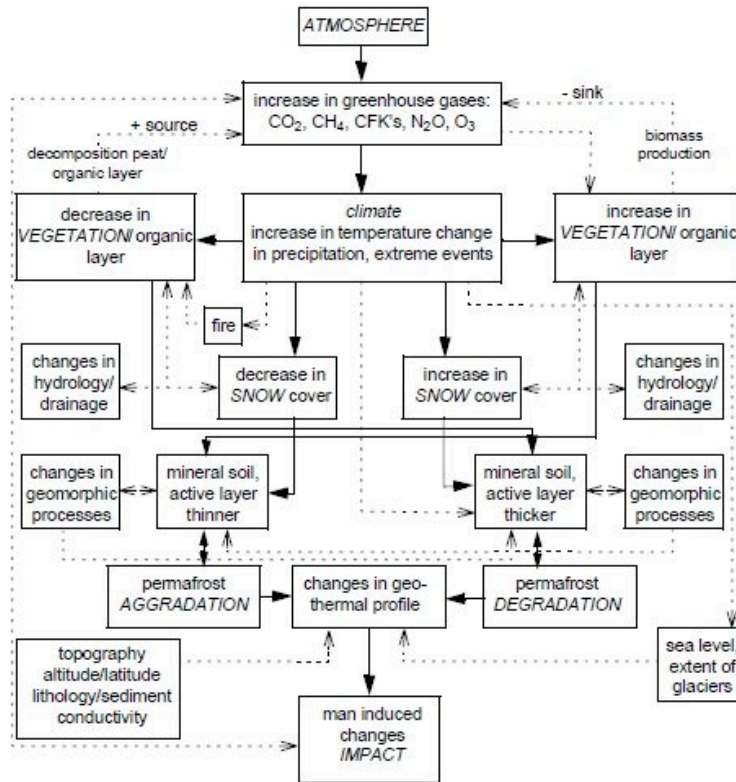
Figure 2.8: Schematic representation of the complex interaction of the active layer and the permafrost with the atmosphere including biological, hydrological and geomorphological processes ([11] (Arenson, 2002).

2.4   Permafrost and global warming

"Warming of the climate system is unequivocal, as it is now evident from observations that confirm the increased air and ocean temperature, widespread melting of snow and glaciers and rising sea levels" ([68] IPCC, 2007).
An increasing number of hazardous rockfalls and rock slides of all magnitudes observed in the Alpine environment during the last decade, is one of the events

15
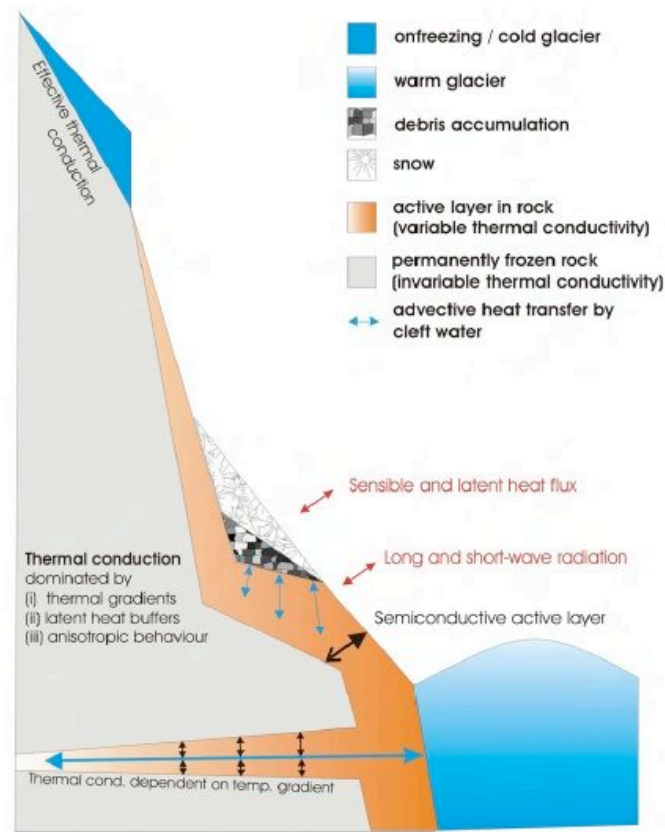
Figure 2.9: A conceptual model for the thermal development of rock permafrost including two-dimensional sources of heterogeneity ([79] (Kraublatter, 2009).

recognized as consequences of the climate change ([65] Harris et al., 2001). Mountain permafrost also contains valuable information on climate change: it influences the evolution of mountain landscapes and affects human infrastructure and safety. Permafrost warming or thaw affects the potential for natural hazards such as rock falls, debris flows and secondary events triggered by them and also affects the topography itself in steep terrain. As in Arctic permafrost regions, construction in mountain permafrost regions requires

special precautions and warming permafrost poses problems to infrastructure. Measurements of permafrost temperature, as well as providing information on present-day permafrost stability, offer data on past climate changes.The speed of most monitored alpine rock glaciers, a form of mountain permafrost in which frozen debris and/or ice underlie a layer of debris and which move downslope, has increased significantly during recent years. This acceleration is likely due to a reduction in viscosity of the underlying permafrost as a result of warming. Warming can reduce the stability of permafrost in steep areas and thus cause increased rock falls. At least four large events involving rock volumes over 1 million m^3 took place in the Alps during the last decade ([125] Romanovsky & Osterkamp, 1995). Ice-rock avalanches were documented e.g. at Mt. Steller, Alaska (5*10^{7}m^3) in 2005, at Dzhimarai-Khokh, Russian Caucasus (4*10^{6}m^3) in 2002 as well as at the Brenva (2*10^{6}m^3) and the Punta Thurwieser (2*10^{6}m^3) in the Italian Alps in 1997 and 2004 ([79] Krautblatter, 2009). Accordingly, enhanced activity of cliff falls (10^4-10^{6}m^3), block falls (10^2-10^{4}m^3), boulder falls (10^1-10^{2}m^3) and debris falls (<10 m^3) was observed from permafrost-affected rock faces ([45] Fischer et al., 2007).

As most permafrost rock walls in lower altitudes face northerly directions ([54] Gruber et al., 2004), changes in air temperatures will play a vital role in permafrost degradation. According to Beniston, "minimum temperatures have exhibited the strongest warming in the second half of the 20th century, and there is a distinct amplification of this warming at high elevations" ([15] Beniston, 2003). Warming of winter temperatures at high elevations systematically corresponds to an increased NAO (North Atlantic Oscillation) Index and is, therefore, believed to proceed with global warming. In the twentieth century, global temperatures have risen by 0.74°C. In the Alps, the increase was much greater, amounting to +1.2°C from 1890 ([23] Brunetti et al., 2006). The trend is especially pronounced for winter minimum temperatures, which are a key factor for rock permafrost development.

Present climate change scenarios for Alpine areas herald a rise in temperature of 3°C by 2050 and between 1.5 and 5.4°C in the Aosta Valley ([143] SMS, 2006), with possibly increased precipitation in winter and substantial decrease in summer ([14] Beniston, 2004). This points towards an increase in factors (minimum temperatures, maximum temperatures, summer radiation) to which rock permafrost degradation is very susceptible ([79] Krautblatter, 2009).

Mountain glaciers and permafrost are key scientific indicators for global and regional climate variation: due to their proximity to melting conditions under terrestrial conditions, they are particularly sensitive to climate changes. In fact, the Intergovernmental Panel on Climate Change (IPCC) recognizes

glaciers as the best terrestrial indicator of climate change, due to their sensitivity to climatic variations. Mountain and lowland permafrost are similarly sensitive to climate changes because of their strong dependency on climatic conditions at the ground-atmosphere interface and the subsurface ice often involved (e.g., [125] Romanovsky & Osterkamp, 1995; [65] Harris et al., 2001).

However, much less is known about the response of permafrost to changes in boundary conditions due to the wide variety of surface and ground conditions, and the complex interplay of the processes involved. Permafrost reacts in a much delayed and attenuated way to climatic changes compared to glaciers. Thus, both glaciers and permafrost together make up a key set of targets for monitoring climate change and its impact on terrestrial systems in cold regions ([55] Haeberli et al., 2007). Glaciers constitute a straightforward and clearly visible indicator, permafrost a long-term and invisible one.

While extreme responses to the warm last two decades were reported for all permafrost environments, permafrost decay in high-alpine environments is more difficult to predict for a number of reasons. These include the high importance of local topography, aspect, shading, microclimate, local wind patterns, glacier-permafrost interconnectivity and human interaction. In addition, there is certain evidence that alpine permafrost systems react more sensitive than Nordic permafrost systems: observed permafrost temperature changes are more variable in the Alps than in the Nordic permafrost boreholes due to the effects of topography, aspect and local heat transfer ([67] Harris et al., 2003).

In addition, Alpine permafrost is warmer and closer to thawing. The temperature of alpine permafrost in the upper tens of meters has increased by about 0.5-0.8°C in the last century ([67] Harris et al., 2003b). This corresponds to an increase of the altitude of the lower permafrost line of 100 m ([61] Haeberli & Wegmann, 1997).

An extensive review of permafrost boreholes temperatures by Harris et al. (2009) yielded that shorter-term extreme climatic events are equally important as they are immediately reflected by changes in active layer thickness ([79] Krautblatter, 2009). The thickness of the active layer will increase and may cause problems, in particular related to nearby structures ([11] Arenson, 2002). In addition, climate change may result in new different ground freezing conditions, thereby influencing the surface velocity and the maximum depth of solifluction processes ([92] Matsuoka, 2001).

A rise in elevation of the lower permafrost boundary has to be expected within mountain permafrost areas, causing local degradation of frozen slopes ([61]

Haeberli et al., 1997) and loss of stability within ice-filled rock discontinuities, even at temperatures still below the freezing point ([32] Davies et al., 2001).

2.4.1 Alpine permafrost research: a short review

Early permafrost research was conducted in high-latitude lowlands, mainly motivated by the expansion of infrastructure and with considerable financial interest involved (e.g., mining, pipeline construction, petroleum exploration). A wealth of basic and engineering knowledge is therefore available from polar and arctic permafrost studies (see [44] French 1988). Only in the 1970s, graphologists begin systematic studies on mountain permafrost in Europe, mainly provoked by the distinct landforms of rock glaciers. Since then, mountain permafrost has become a research discipline of its own, dealing with its specific characteristics and problems, which for the most part are related to steep topography and high spatial variability. This complexity is the major challenge for the interpretation of observations and measurements, as well as for the design, parameterization, and validation of models.

In recent years, mountain permafrost studies focused more and more on steep rock slopes. On the one hand this was motivated by an increase in rock fall observations from permafrost areas (e.g., [34] Deline 2001, [109] Noetzli et al. 2003, [121] Ravanelet al., 2010) and rising scientific as well as public awareness of the relation of permafrost degradation and slope stability ([32] Davies et al. 2001, [55] Gruber & Haeberli 2007, [61] Haeberli et al. 1997, [65] Harris et al. 2001). On the other hand, corresponding measurement strategies and modeling tools have been developed ([54] Gruber et al. 2004, [55] Gruber et al. 2007), which made permafrost research in steep bedrock slopes possible in the first place. So far, studies primarily concentrate on the European Alps. Here, considerable infrastructure exists, which facilitates access and, at the same time, increases the vulnerability of the area. However, phenomena and problems related to mountain permafrost are similar for all mountain regions and start to be recognized in other areas, such as the Canadian Rocky Mountains, the Southern Alps in New Zealand, Iceland, or the Kazbek massif in the eastern Caucasus.

Chapter 3

Thermal regime and microseismic activity: the case study of Matterhorn peak

3.1 Introduction

An increasing number of rockfalls and rock slides of all magnitudes observed in the Alpine environment during the last decade, is one of the events recognized as consequences of the climate change.

Permafrost warming affects the potential for natural hazards such as rock falls, debris flows and secondary events triggered by them and also affects the topography itself in steep terrain ([56] Gruber et al. 2004).

Many ice-rock avalanches have been documented in the Italian Alps, e.g. Brenva 1997, Grandes Jorasses 2002, Matterhorn 2003, Thurwieserspitze 2004, Dru 2005, Aiguille des Toules 2008, Tré-la-Tête 2008, Patrí Peak 2008, Refuge Vittorio Emanuele II 2008, Mont Crammont 2008 , Aiguille du Dru 2011; accordingly, enhanced activity of cliff falls, block falls, boulder falls and debris falls has been observed from permafrost-affected rock faces ([34] Deline, 2001, [121] Ravanel et al. 2010, [35] Deline et al., 2008, [122] Ravanel & Deline 2012).

A rise in elevation of the lower permafrost boundary has to be expected within mountain permafrost areas, causing local degradation of frozen slopes and loss of stability within ice-filled rock discontinuities, even at temperatures still below the freezing point (e.g. [61] Heaberli et al., 1997, [32] Davies et al., 2001, [109] Noetzli et al., 2003, [55] Gruber & Heaberli, 2007).

The awareness of rock slope instabilities in high mountain raised in alpine European countries after summer 2003, when an exceptional heat wave hit central Europe and was accompanied by an unusually high number of rock-falls ([15] Beniston, 2003).

Focusing on the Italian Alpine region, the Matterhorn (4478 m a.s.l., NW Italian Alps), a rock pyramid made of highly fractured gneisses and gabbros, has suffered rock deformation and rock-falls since summer 2003.

The most relevant rockfall event in the area was the "Cheminée" rockfall (2000 cubic meters) occurred on August 18th, 2003 just below the Carrel hut. This event was of particular scientific interest since a large ice lens (of about 15 m high and 7 m large) was observed on the detachment surface, calling for a possible role of permafrost degradation and, thus, climate warming in the event initiation (Figure 3.1). Similar events occurred nearby in the following summers also revealed massive ice presence.

Rock fracture in Alpine regions has often been attributed to the freezing and volumetric expansion of water trapped within pores and cracks (Hales and Roering, 2007). Ice segregation is an alternative process of bedrock fracture ([157] Walder & Hallet, 1985, [63] Hallet et al., 1991): it occurs when temperature gradient induces suction in freezing ground or rock and this drives unfrozen water, held in capillaries and adsorbed on the surfaces of mineral particles, through a porous medium toward freezing sites where lenses or layers of ice grow. If ice segregation fractures bedrock permafrost, the fractures and ice lenses are expected to concentrate just beneath the top of the permafrost and in the base of the active layer; subsequent warming and thawing weakens or loosens the fractured rock ([93] Matsuoka & Murton, 2008).

The study of the complex mechanisms linking climate changes and permafrost degradation to the increased number of rock slope instabilities recorded at high altitude in the last years, has become a topical subject.

The development of a new methodology involving both in situ and in laboratory analyses has been investigated and validated through the application to the Matterhorn case of study.
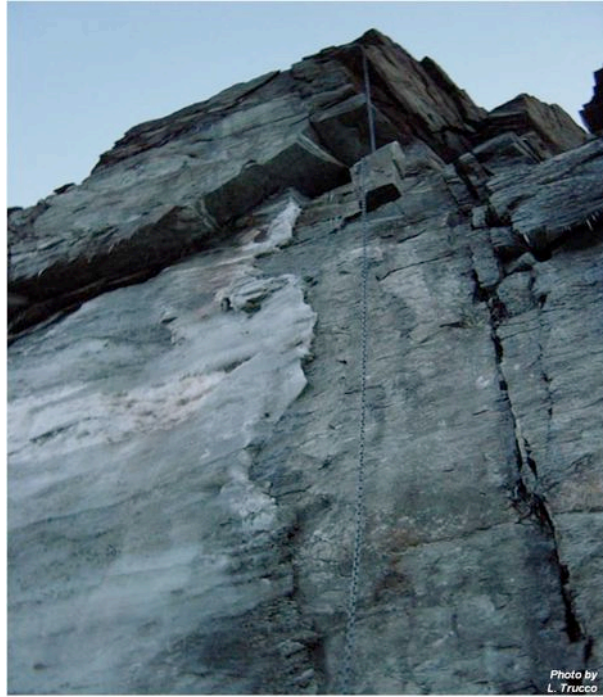
Figure 3.1: The ice lens (of about 15 m high and 7 m large) observed on the detachment surface after the "Cheminée" rockfall occurred on August 18th, 2003 (Photo by L. Trucco).

3.2 The Matterhorn peak case study

The formation and propagation of cracks in rock material, considered as factors that could lead to collapse, give rise to elastic waves which can be detected by a suitable transducer array. As a consequence, monitoring the microseismic (MS) activity can be considered a suitable investigation tool to measure and analyze the deformation and the instability of high mountain bedrock ([139] Senfaute et al., 2003).
This activity was proposed in the Interreg IIIA Alcotra project n. 196 "PERMAdataROC", and the MS investigation technique was adopted as a measure of the stability.

23

A monitoring system composed by geophones and thermometers was installed in 2007 at the Carrel hut (3829 m a.s.l., Matterhorn, NW Alps). In 2010, in the framework of the Interreg 2007-2013 Alcotra project n. 56 MASSA, the monitoring system has been empowered and renovated by CNR IRPI Torino, in cooperation with Regione Valle d'Aosta, and by ARPA Valle d'Aosta

Among the instrumented sites, the Matterhorn case of study is considered of particular interest since it represents one of the very few cases in which the MS activity is employed to the rock slope stability assessment in high mountain. Moreover a thermometric monitoring system is coupled with the MS network assuring the possibility of performing a crossed analysis.

Figure 3.2: The Matterhorn study site.

The MS monitoring system (DIMAS - 16 "CERVINO") (Figure 3.3) is made of:

1) A 18 channel acquisition system installed inside the hut;

2) 5 triaxial transducers (geophones with an own frequency of 100 Hz); in

2010, 3 low frequency geophones were installed;

3) A power supply group connected to soar panels and a wireless transmission system.

The installed thermometric monitoring system consists of two station on the South side and on the North-West side; each station is equipped to measure:

1) The air temperature;

2) The rock temperature at three different depths (3 cm, 30 cm, 55 cm).
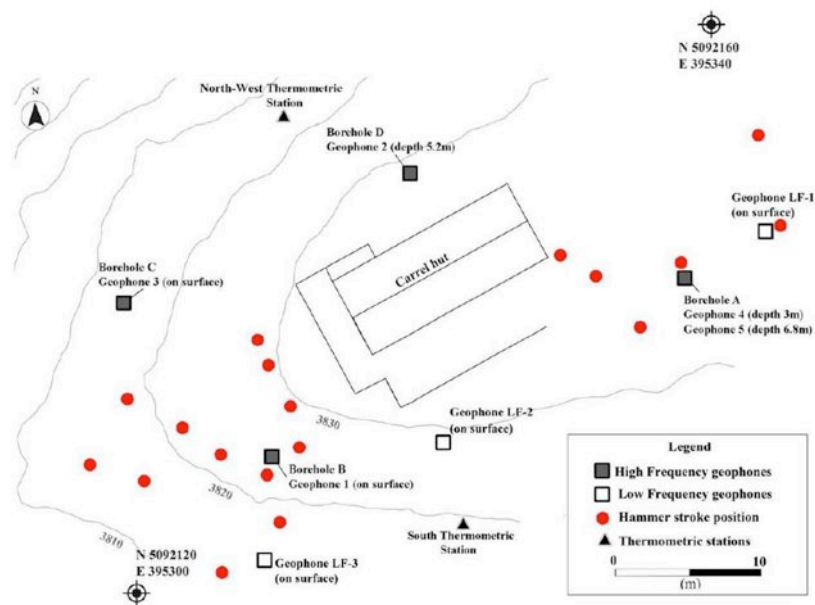
Figure 3.3: The J. A. Carrel hut and the position of the geophones, of the hammer strokes and of the thermometric stations ([111] Occhiena, 2011).

25

3.2.1 Natural events location

Within the Ph.D. thesis of Cristina Occhiena ([111] Occhiena 2011) the location of 615 events, characterizing the whole MS data set, has been performed mainly to identify the source distribution during the first six months of monitoring. Observing Figure 3.4 it is possible to notice that most of the points located inside the network boundaries correspond to more superficial events.
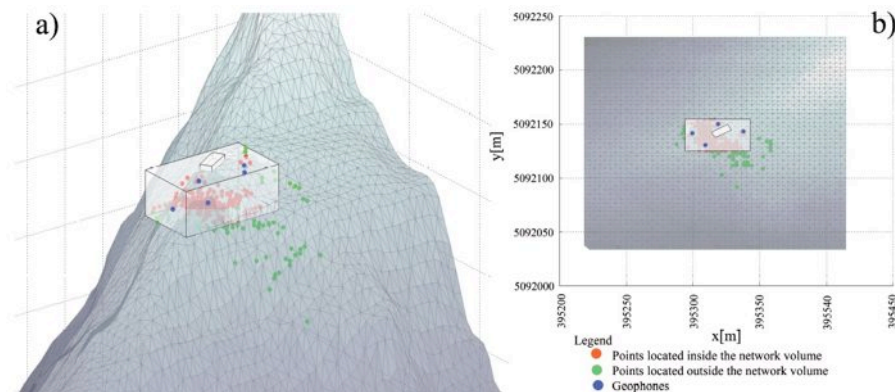
Figure 3.4: Location results of the whole data set (615 events) in relation to the network volume; a) perspective view showing the points inside (in red) and outside (in green) the volume: it is possible to notice that most of the points located inside the network boundaries correspond to the more superficial events; b) projection of the results on the horizontal plane. ([111] Occhiena, 2011).

Moreover the application of cross-correlation analysis and coherency computation has allowed to identify similar events (with high coherency values) probably due to common failure mechanisms.

9 similar events belonging to the same class have been located using an heterogeneous multi-velocity model: the sources, all included in the network volume, appear aligned along a quite superficial plane. A multiple linear regression was carried out in order to identify the plane interpolating the positions of the sources. The computed plane interpolates with a good approximation the nine estimated hypocenters.

Plane coordinates have been represented in terms of dip and dip direction

angles and a comparison with the morphostructural survey results has been carried out. The dip direction of the plane was about 204°, while the dip angle was equal to 33°. Considering the main discontinuity systems measured in the morphostructural survey (Figure 3.5) it has been possible to notice a correspondence between the computed plane and the system characterized by NW-SE orientation, which is responsible of the main features of the Carrel ridge: a planar sliding has been identify as a potential instability mechanisms.
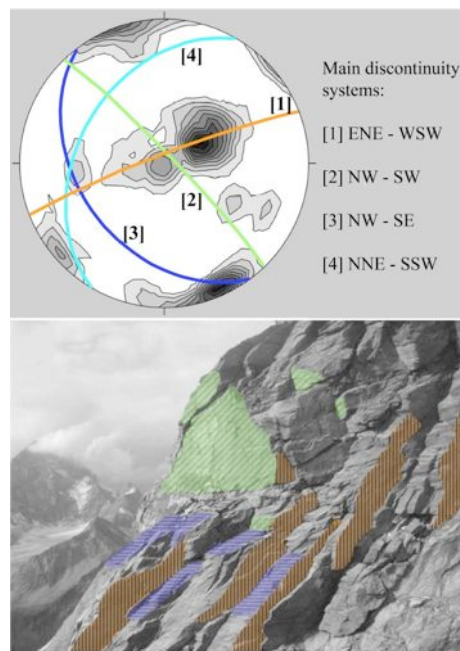
Figure 3.5: Discontinuity systems measured in the Carrel hut surroundings: a) stereographic projection of all the measured discontinuity systems; b) stereographic projection of the four main systems identified by the statistical analysis of the measured planes; c) identification of the four main systems on a portion of the slope near to the Chemine detachment area (images modified after Pogliotti, 2006) ([111] Occhiena, 2011).

3.3   Subsurface thermal regime

In order to assess if the superficial source location could be correlated to the bedrock thermal regime and if the thermal fluctuation could influence the increasing number of events, a simplified thermal model has been computed.

3.3.1   Subsurface temperature

Ground temperature are determined by air (or ground surface) temperature, heat flow from interior of the earth, and soil thermal properties. Surface temperature undergo approximately simple periodic fluctuations (Figure 3.6) on both a daily and an annual cycle. Meteorological data for a given location are used to provide the mean annual temperature (T_m) and the surface temperature amplitude (A_S). The ground surface temperature ($T_{S,t}$) can be reasonably estimated as a sinusoidal fluctuation that repeats itself daily and annually ([10] (Adersland, 2004):

$$T_{S,t} = T_m + A_S \sin \frac{2\pi t}{p} \tag{3.1}$$

where t is time and p is the period, 24 hours or 365 days. If time t is measured from January 1st and the coldest time of the year occurs about two weeks into January, the surface temperature curve (Figure 3.6a) will be shifted to the right. This can be accomplished by replacing the sin term in equation 3.2 by $-\cos(2\pi t/p - 2\pi\Phi/p)$. The term Φ represents a phase lag with the same units as the period p. This temperature pattern is attenuated with depth (z) and, in a homogeneous soil with no change of state, the temperature ($T_{z,t}$) at any depth and time can be calculated as ([10] (Adersland, 2004):

$$T_{z,t} = T_m + A_S \exp(-z\sqrt{\frac{\pi}{\alpha_T}}) \sin(\frac{2\pi t}{p} - z\sqrt{\frac{\pi}{\alpha_T}}) \tag{3.2}$$

whereα_T is the soil thermal diffusivity.
Equation 3.2 is that of a wave motion whose amplitude A_z rapidly decreases with increase in depth z, and it is given by:

$$A_z = A_s \exp(-z\sqrt{\frac{\pi}{\alpha_T}}) \tag{3.3}$$

The range in temperatures, or maximum variation, for any point below the ground surface is represented by the area between the trumpet-shaped curves

in Figure 3.6. These curves are given by

$$T_z = T_m \pm A_s \exp(-z\sqrt{\frac{\pi}{\alpha_T}}) \qquad (3.4)$$
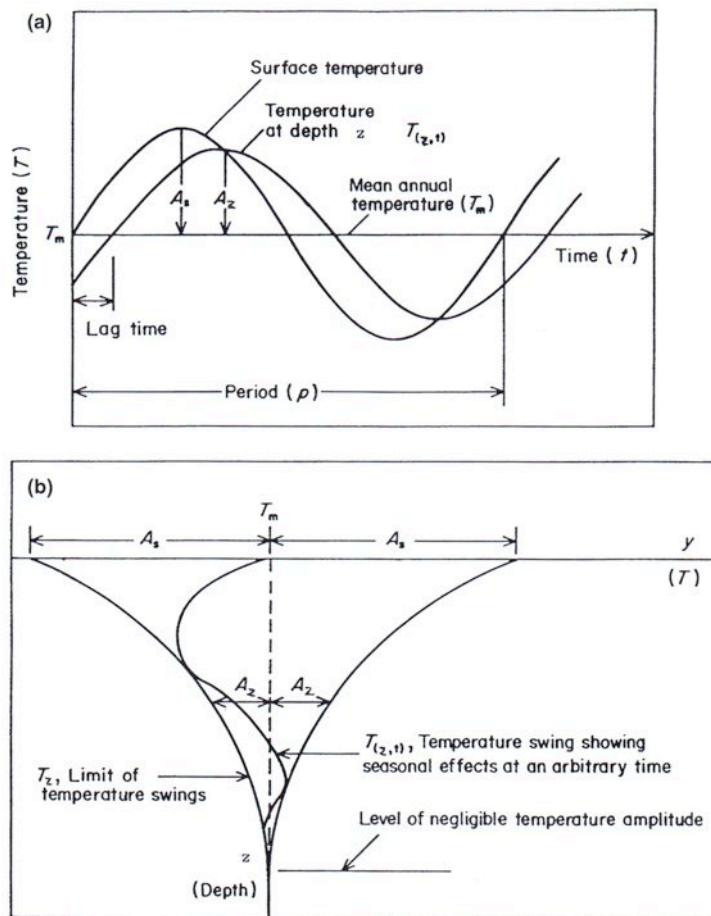
Figure 3.6: Surface and ground temperatures: (a) sinusoidal fluctuations; (b) temperature attenuation with depth ([10] (Adersland, 2004).

29

Equation 3.4 represents the maximum and the minimum ground temperature at depth z. The simple solution represented by equation 3.2 indicates the trends found in actual ground temperatures ([10] Adersland, 2004). But in practice, they can be modified significantly by the effects of soil latent heat, differences in frozen and thawed rock properties (conductivity and diffusivity) non-homogeneities and non symmetrical surface temperatures because of seasonal snow cover, vegetation, and other local climatic influences. No analytical closed form solution exists that consider all these effects, but numerical solutions that take some of these factors into account will be explained and developed in the following.

3.3.2 Heat transfer numerical model

In steep rock slopes, heat transfer at depth mainly results from conduction and it is driven by the temperature variations at the surface and upward heat flow from the interior of the earth (geothermal heat flux). As a first approximation, the effects of fluid flow have been neglected in bedrock permafrost ([82] Kukkonen & Safanda, 2001): therefore the analyses have been performed, assuming that heat exchanges are only due to conduction, which allows a realistic simulation of both, pattern and values of subsurface temperatures.
The near-surface temperature measurements obtained from the two boreholes sites (installed on the South side and on the North-West side of the Carrel hut ridge) provide the upper boundary condition for the numerical heat transfer model performed using the software package COMSOL Multiphysics.

Governing equations

For study of subsurface heat transport, the variation of temperature (T) with time (t) can be described by:

$$\nabla \cdot (\lambda_T \nabla T - \rho_f c_f T \mathbf{v}) + h = \frac{\partial T}{\partial t}(\phi \rho_f c_f + (1 - \phi)\rho_m c_m) \qquad (3.5)$$

The first term on the left describes the transport of heat by conduction with a thermal conductivity tensor λ_T (Wm^{1}K^1), whereas the second one specifies advection by motion of pore fluid with a Darcy velocity $\mathbf{v}$ (ms^1). ρ is density (kgm^3), c is heat capacity (JK^{1}kg^1), and h is volumetric heat production (Wm^3): in this model only conduction has been considered, as explained above. The subscripts f and m account for the two-phase mixture between solid rock (m) and fluid-filled pore space (f). This mixture is characterized by porosity ϕ ([98]

Mottaghy & Rath, 2006).

When modeling the thermal effects of freezing and thawing, obviously equation (3.5) has to include three phases: matrix, fluid and ice. To achieve this, the following volume fractions are defined:

$$\phi_m = 1 - \phi, \quad \phi_f = \phi \cdot \Theta, \quad \phi_i = \phi - \phi_f \tag{3.6}$$

where Θ denotes the fraction of pore space occupied by fluid, and an additional ice phase is introduced marked by index i. The constraint $\phi_m + \phi_1 + \phi_f = 1$ implies that pore space is saturated.

Latent heat effects during phase change

The latent heat effect (i.e., the effect of energy consumption during the phase change from ice to water) has been considered by introducing an apparent heat capacity which substitutes the volumetric heat capacity in the heat transfer equation within the freezing interval w, where phase transition takes place. The approach described by Mottaghy and Rath (2006) has been used: the concept of an apparent heat capacity $(\rho c)_a$ is invoked in order to account for the latent heat associated with thawing and freezing, defined by:

$$(\rho c)_a = (\rho c) + \rho_i L_f \phi \frac{\mathrm{d}\Theta}{\mathrm{d}T} \tag{3.7}$$

where ρ_i is the density of ice, L_f is the specific latent heat of fusion (333.6 kJkg^1), ϕ is the porosity and Θ is the volumetric unfrozen water content.

This function is characterized by a thawing temperature T_L (liquidus, usually 0°C) and a parameter w, which describes the temperature range where phase transition takes place and unfrozen water content is present: this corresponds to a freezing interval $\Delta T = T_L - T_S = 2$K, where T_S is the freezing temperature (solidus), at which almost all fluid is frozen.

Θ is thus assumed to be a function of temperature in a specified interval ([88] Lunardini, 1981), for example,

$$\Theta = \begin{cases} \exp\left[-\left(\frac{T - T_L}{w}\right)^2\right] & \text{if } T < T_L \\ 1 & \text{if } T > T_L \end{cases} \tag{3.8}$$

Considering the freezing range in rocks, equation (3.8) and (3.6) are used for taking into account the contributions of the fluid and the ice phase ([98] Mottaghy & Rath, 2006). Since the material phases are assumed to be

randomly distributed, the weighted thermal conductivity is espressed by the square-root mean ([98] Mottaghy & Rath, 2006):

$$k(\phi_{m,f,i}T) = \left[\phi_m\sqrt{k_m(T)} + \phi_f\sqrt{k_f(T)} + \phi_i\sqrt{k_i(T)}\right]^2 \qquad (3.9)$$

Boundary conditions and mesh definition

A purely 1D conductive transient thermal field in an isotropic and homogeneous medium has been considered. The simulated domain beneath the boreholes at Carrel hut ridge, has 20 m depth: complete mesh consisted of 400 edge elements.
The mean daily temperature measured at 3 cm depth by the near-surface thermometric monitoring system has been set as upper boundary condition of the modeled profile.
A uniform lower boundary heat flux of 0.05 W/m^2 (equal to the geothermal heat flow) has been set and thermal insulation has been assumed for the lateral boundaries of the geometry.

Subsurface properties

Subsurface material properties has been assigned on the generated FE mesh. In purely diffusive and transient simulations, thermal conductivity, volumetric heat capacity, and the ice/ water content are the petrophysical parameters of importance. However, only little is known on the subsurface characteristics below steep topography: some parameters have been set based on published values and others determined in laboratory tests, as reported in Table 3.1.
The freezing parameter w, which describes the steepness of the unfrozen water content curve, has been taken equal to 2 ([106] Noetzli & Gruber, 2009), while the freezing range as been defined as follows ([98] Mottaghy & Rath, 2006):

$$\begin{cases} T_L = 0°\text{C} = 273.15°\text{K} \\ T_S = -3°\text{C} = 270.15°\text{K} \end{cases} \qquad (3.10)$$

Highly fractured rock mass has been considered to behave as equivalent porous media, isotropic and homogeneous: it is characterized by a porosity which has been estimated through Wyllie time-average equation. It relates the wave's phase velocity v to porosity ϕ, fluid velocity v_f, and rock matrix velocity v_m:

$$\frac{1}{v} = \frac{\phi}{v_f} + \frac{1 - \phi}{v_m} \qquad (3.11)$$

Table 3.1: Subsurface material properties.

	Density [Kg/m^3]	Thermal conductivity [W/mK]	Heat capacity [J/KgK]
Gneiss	2774.46	2.711	800
	(Lab. test DIATI Torino)	(Lab. test CNR Pisa)	(William, 1989)
Water	1000	0.613	4180
	(Shulson, 2009)	(Cengel, 2003)	(Cengel, 2003)
Ice	916.4	2.4	2110
	(Shulson, 2009)	(Shulson, 2009)	(Shulson, 2009)

Through this relationship, it has then been calculated a porosity $\phi = 6$ % for the jointed rock mass, by inserting the P-waves velocities v=2958 m/s based on estimations from geophysical measurements ([111] Occhiena, 2011), an average fluid velocity $v_f = 340$ m/s ([162] Wyllie et al., 1958) and a rock matrix velocity $v_m = 6080$ m/s which is an average velocity for the material characterized by a mixed mineralogy ([95] Mavko et al., 1998).

3.3.3 Results

Figure 3.7 shows the simulated T(z)-profiles obtained from the North-West side thermometric monitoring station. It can be noticed that this rockwall located at 3829 m a.s.l. experiences seasonal frost/thaw penetration to 2 m in depth.

Comparing the two spatial-temporal distributions of temperature and microseismic activites, it is possible to verify that the recording data can be correlated with thaw and solidification mechanism. In fact, the microseismic source localization has revealed that these are concentrated in the active layer. In particular the hypocenters of the selected class of nine events, which may belong to a disconinuity system, as explained in 3.2.1, seem to be localized close to the permafrost boundary, a layer characterized by ice-rich fracturated zones and ice-filled cracks.

Results from geophysical monitoring could confirm the hypothesis of ice segregation as a mechanism leading to steep bedrock degradation and its associated instability: this process can contribute to the destabilization of much larger volumes of rock than would expected due to volumetric expansion.

33
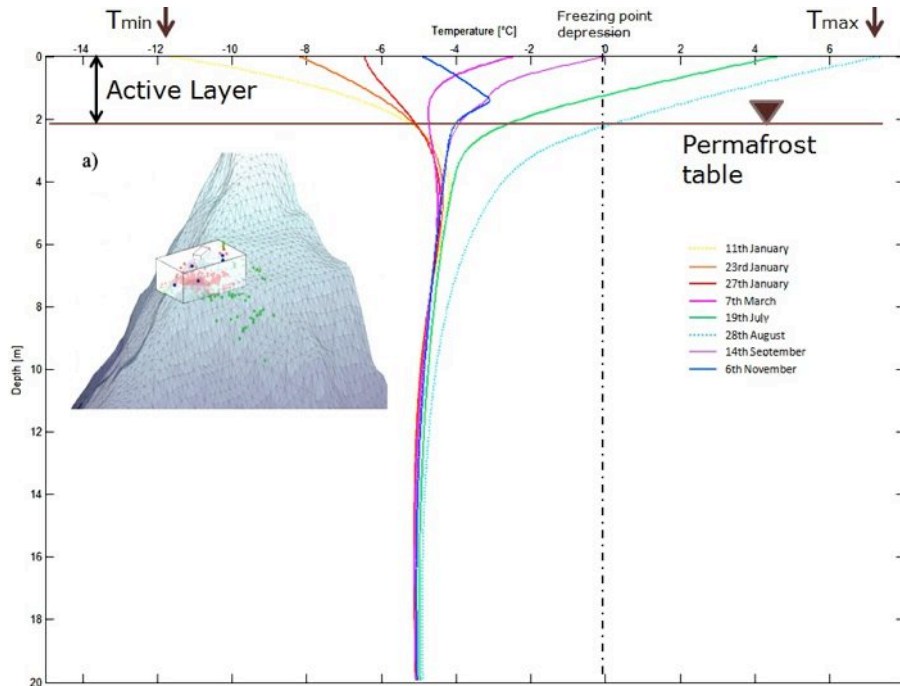
Figure 3.7: Simulated T(z)-profiles obtained from North-West side thermometric monitoring station and the hypocentres location results from geophysical monitoring (Carrel hut, Matterhorn).

3.4 Segregation ice growth as a mechanism for rock fracture

From the analysis in the preceding paragraphs, it has been seen how crack movements in the bedrock active layer detected by microseismic activity could contribute to the prediction of large scale rockfalls and rock avalanches triggered by permafrost degradation.

From the Matterhorn case study field observation, the presence of massive ice in the Cheminée rockfall detachment zone has been interpreted as a signal of ice segregation mechanism involved in high mountain bedrock degradation.

The hypothesis seems to be confirmed by several evidences of massive ice in Alpine bedrock, as described by Gruber and Haeberli (2007): during construction of the summit station (3820 m a.s.l.) of the Chli Matterhorn cable car near Zermatt, Switzerland, ice-filled cracks were found near the entrances of a tunnel traversing the summit pinnacle. The nearby construction of foundations for a cable car (3286 m asl.) to Rote Nase (3250 m asl.) revealed ice-filled fractures up to 20 cm wide at depth. Ice-filled joints have also been reported from the Sphinx station (3500 m asl.) of the Jungfraujoch railway, Switzerland and from the summit of Chli Titlis, Switzerland. Massive ice has also been found at depths of 42 and 90 m in a borehole drilled in bedrock near Stelvio Pass (3000 m asl.), Italy and in a highly fractured zone between 12 and 14 m depth in a borehole drilled in Cime Bianche (3100 m asl.), Aosta Valley, Italy. Technicians at the Aiguille du Midi cable car summit station (3830 m asl.) near Chamonix, France noticed water flow into the station tunnels for the first time during summer 2003.

Recent climate warming may have promoted thawing of permafrost that in turn may have triggered detachment of rock blocks thicker than the previous active layer. This effect is recognized by increasing observations of slab falls type of rock avalanches (e.g. [34] Deline, 2001; [55] Gruber & Haeberli, 2007). During abnormally warm summers in high mountain, the uppermost part of permafrost thaws deeply: the bedrock often includes a number of ice layers possibly formed during upward freezing and ice segregation processes (e.g. [99] Murton, 1996; [102] Murton et al., 2006). Warming permafrost could be linked to the destabilization of steep rock slopes by the fracture condition alterations, which may provide a slip plane during thawing ([93] Matsuoka & Murton, 2008).

3.5 Mechanisms of frost weathering

The fracture of bedrock is fundamental to debris production and landscape development. Rock fracture in alpine regions has often been attributed to the freezing and volumetric expansion of water trapped within pores and cracks. An alternative process of bedrock fracture, involving ice segregation, remains poorly characterized despite a number of theoretical and experimental studies over the past two decades.

Pore water influences rock damage through three mechanisms:

1) Volumetric expansion of nine per cent occurs as liquid water turns to ice. If the water completely fills spaces in rock and freezes in situ, then,

theoretically, at a temperature of -22°C ice growth can generate pressures up to 207 MPa inside cracks in a rock strong enough to withstand it. This ice-induced stress is easily enough to fracture any rock because the maximum tensile strength of rock is one to two orders of magnitude lower than 207 MPa; and even at warmer subzero temperatures the maximum stress is still substantial. However, the conditions necessary for frost weathering by volumetric expansion are unusual: the rock must be water-saturated, or nearly so (to avoid compression of air), and frozen rapidly from all sides (to freeze the water in situ). Thus the dominant role in frost weathering often attributed to volumetric expansion has been questioned ([157] Walder & Hallet, 1986). Where this process does appear to operate is within a few centimetres of the surface of rocks whose pores or cracks are water filled (or nearly so) and subject to rapid freezing; this results in prying away of mineral grains and rock flakes. At a larger scale of bedrock outcrops, volumetric expansion within existing, water-filled joints can widen joints and heave bedrock ([93] Matsuoka & Murton, 2008).

2) A second way in which volumetric expansion breaks up rock is by hydrofracture. The high pore-water pressures needed for hydrofracture may arise from pore-water expulsion in water-saturated rock with large, interconnected pores or where large hydraulic gradients exist. In addition, freezing of saturated rock with pores small enough normally to favour cryosuction and ice segregation can, if freezing is sufficiently rapid, instead expel water ([157] Walder & Hallet, 1986). If the water cannot drain away as quickly as it is expelled, pore-water pressure may sometimes rise sufficiently to deform or hydrofracture the rock. Potentially, therefore, intact rock may hydrofracture during rapid inward freezing of boulders, causing the rock to burst ([84] Lautridou, 1987) or, perhaps, during bidirectional freezing of an active layer. Hydrofracture may also cause widening of pre-existing cracks during rapid freezing of the surface centimetres of moist mountain rockwalls [136] Sass, 2004). In a bedrock active layer developed on the Canadian Shield, pore-water pressures as high as 400 kPa at depths of about 2m in water-filled cavities have been recorded as water freezes and expands, and are thought to induce bedrock heave [38] Dyke, 1984). But whether active-layer pore-water pressures can hydrofacture rock, perhaps loosening individual grains, lengthening existing cracks or generating new ones, is not known ([93] Matsuoka & Murton, 2008).

36

3) Ice segregation: temperature gradient-induced suction in freezing or frozen ground or rock drives unfrozen water, held in capillaries and adsorbed on the surfaces of mineral particles, through a porous medium toward freezing sites where lenses or layers of ice grow. If ice segregation fractures bedrock permafrost, the fractures and ice lenses are expected to concentrate in wet, porous rock just beneath the top of the permafrost and in the base of the active layer ([102] Murton et al., 2006).
A number of clear distinctions exist between the segregation ice and volume-expansion models, as it has been summarized in Table 3.2.

A number of rock properties would contribute to intact rocks frost weathering. These properties are classified into

1) those affecting ice formation and the expansive force-;

2) those constraining the resistance ([91] Matsuoka, 1991).

Properties affecting the expansive force include:

- porosity: governs volumetric expansion by delimiting the capacity of ice volum ([96] Mellor, 1970);

- specific surface area: contributes to suction ([89] Matsuoka, 1990);

- pore geometry: influences the critical temperature;

- permeability: controls water migration.

The resistance is simply given by the tensile strength of a bulk rock, under the assumption of homogeneity of rock ([89] Matsuoka, 1990). When the growth of microfractures in rocks is considered, the fracture toughness controls the resistance ([157] Walder & Hallet, 1986). Other parameters associated with the resistance include the mineral composition, which mainly controls the granulometry of the debris produced.
Frost sensitivity is roughly proportional to the ratio of specific surface area to tensile strength, demonstrating the major role of ice segregation in microgelivation of intact rocks ([92] Matsuoka, 2001).

3.5.1 The ice segregation model

The segregation ice model of frost weathering treats freezing in water-saturated rocks as closely analogous to slow freezing in fine-grained soils.

Table 3.2: Comparison of frost weathering models ([63] Hallet et al., 1991).

Volumetric-expansion model	Segregation ice model
No frost weathering if pore water fluid contracts upon freezing	Frost weathering doesn't depend on the volumetric expansion of water during freezing
No frost weathering under conditions common in nature: saturation level less then about 91% and pores not effectively sealed off (hydraulically closed system)	Saturation level influences rate of water migration in hydraulically connected pores (open system). Low saturation does not preclude water migration and crack growth
Water may be expelled from freezing sites, but never drawn towards such sites	Water attraction to freezing sites, due to chemical potential gradients, is a key factor in frost weathering. If crack growth cannot accommodate water-to-ice expansion, water is expelled from freezing sites
Crack growth should occur in bursts as water freezes and expands	Slow, steady crack growth should occur as water migrates towards ice bodies within cracks. Predicted crack-growth rates are compatible with values inferred from experimental data
No clear precision of role of environmental conditions or material parameters	Specific prediction of the role of environmental conditions and material parameters emanates from the model and guides experimental work
A variety of other possible mechanisms of frost weathering are viewed as essentially independent	Various mechanisms of frost weathering may be unified within the framework of fundamental thermodynamic and fracture-mechanical principles

Frost weathering is due to the progressive growth of microcracks and relatively large pores wedged open by ice growth ([63] Hallet et al., 1991).

Ice lenses play the key role in frost induced heaving of soils and fracture of bedrock, which are fundamental to weathering in cold regions and high mountain areas. Frost heaving creates debris and dramatically shapes landscapes into complex patterns.

Ice lenses are formed when moisture, diffused within soil or rock, accumulates in a localized zone. The ice initially accumulates within small collocated

pores[1] or pre-existing crack, and, as long as the conditions remain favorable, continues to collect in the ice layer or ice lens, wedging the soil or rock apart. Ice lenses grow parallel to the surface and from several centimeters to several decimeters deep in the soil or rock, which may provide slip planes during thawing ([93] Matsuoka & Murton, 2008).

The present model of frost damage in rock, intends to analyse the initial stage of break-up of bedrock and large rock fragments, resulting from the slow growth of cracks pressurized internally by ice.

The existence of an unfrozen water film between ice and substrate could be explained if the free energy of water in close proximity to the surface of mineral grains is lowered. This film exerts an attractive force on water in pores to wich it is hydraulically connected, as well as a "disjoining pressure" that tends to separate ice from substrate ([156] Walder and Hallet, 1985).

As a matter of fact, the mechanism for driving water into ice-rich microfractures involves surface forces developed at the ice-water-mineral interfaces ([63] Hallet et al., 1991).

The water migration results from temperature gradient-induced suction, because as rock freezes and cools, a suction develops in the unfrozen water held in capillaries and adsorbed on the surfaces of mineral particles ([161] Williams & Smith, 1989): a temperature drop of 1°C induces a cryosuction of 1.2 MPa.

These forces generate heaving pressures in freezing soils that attain values up to 20 MPa, approaching the equilibrium ice pressure. Such pressures are nearly twice as large as the tensile strength of the stronger rocks. This fact provided the initial incentive for developing the segregation ice model of frost weathering ([156] Walder and Hallet, 1985), as it implies that ice growth in pre-existing microfractures is capable of progressively fracturing any rock type, if water is available and temperatures are sufficiently low.

At subfreezing temperatures microfractures are progressively wedged in domains that are cold enough to permit sufficient ice-generated pressure to cause progressive microcrack growth, and yet not so cold as to inhibit the water migration required to sustain crack growth.

The migration of water in rocks at subfreezing temperatures decreases rapidly with temperature, because the flux of unfrozen water scales approximately

---

[1]Ice is able to crystallize in the very small pores of the rock: from literature (i.e. [138] Shulson & Duval, 2009), lattice parameters order of magnitude is the nm, so it could be enough in order to start the crystallization. In frozen geomaterials, the ice-type is Ih, hexagonal rings (diameter a) translated along the c-axis, which dimensions are: a=0.45nm, c=0.73nm (Madura 1994).

with the cube of the thickness of unfrozen films and the film thickness in turn decrease with temperature. The increase in water viscosity with decreasing temperature further decreases its mobility at low temperatures.

Anyway these conditions needed for ice segregation (slow rates of freezing or sustained subzero temperatures in moist, porous, fine-grained rock) are common in natural bedrock ([10] Andersland & Ladanyi, 2004).

Walder and Hallet (1985) studied the effect of water migration in rocks at subfreezing temperatures through a model that coupled water transport to cracks with the mechanics of slow penny-shaped fractures (a sketch in shown in Figure 3.8). Combining the ice segregation model with fracture mechanic, they showed that new fractures could propagate in mode I type, to more than 10^{-7} m/s if subjected to ice pressures of 10-12 MPa.
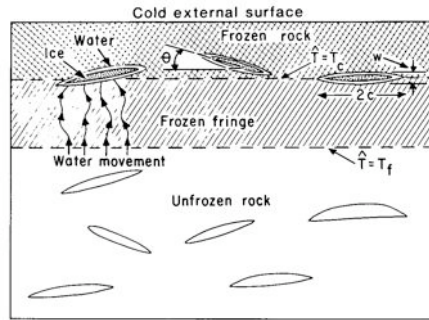
Figure 3.8: Idealization of freezing of cracked rock. Penny-shaped cracks of width w, diameter $2c$ are oriented at an angle Θ to the isotherms. $\hat{T}$, the temperature relative to $0°$C, equals T_c at the crack wall. Rock below $\hat{T} = T_f$ isotherm is unfrozen. Water migrates through the the frozen fringe to growing ice-filled cracks ([156] Walder and Hallet, 1985).

Numerical results obtained simulating mechanics of ice growth, particularly the role of the premelted films in lens growth, and the fracturing mechanism in rock under steady temperature gradients, will be shown in Chapter 4, as the details of the governing equations involved.

Chapter 4

Numerical models

Starting from the hypothesis derived from field observations at the Matterhorn site (see Chapter 3), several approaches to study the ice segregation phenomenon in rock will be presented in the next chapters.

The aim of the research is to design and set up a down scaled physical simulation of this frost weathering mechanism using acoustic emission techniques.

Numerical simulations have been performed in order to validate the experimental procedure as well as to evaluate some predictions. These studies have addressed the mechanics of ice growth, particularly the role of the premelted films in lens growth, and the fracturing mechanism in rock under steady temperature gradients.

Freezing of pore fluid within rock microcracks involves complex thermal, hydraulic and mechanical processes that can have significant mutual interactions. For example, phase changes of pore fluid caused by temperature variations modify the hydraulic regime of the material, which in turn induces mechanical deformation. At the same time, any change in the hydraulic and mechanical conditions feeds back to the thermal processes by way of advection and changes in ice and water contents ([104] Nishimura et al., 2009).

Analysis of frozen rock behavior inevitably requires a numerical technique such as the finite element method (FEM), owing to the non-linearity of the governing equations: models have been developed and implemented with differing degrees of sophistication.

4.1 THM-coupled finite element analysis of frozen rock

In order to try to predict the approximate depth of maximum cracking for the upward freezing experiment, a fully coupled thermo-hydro-mechanical (THM) model has been developed at the Department of Geotechnical Engineering and Geosciences, UPC Barcelona, in cooperation with Professors Eduardo Alonso and Sebastián Olivella.

The finite element (FE) formulation is described by Nishimura ([104] Nishimura et al., 2009) and considers each thermal, hydraulic and mechanical process in freezing water-saturated porous media, and their various interactions, through fundamental physical laws and models.

As a matter of fact, the segregation ice model of frost weathering due to the progressive growth of microcracks and relatively large pores wedged open by ice growth, treats freezing in water-saturated rocks as closely analogous to slow freezing in fine-grained soils.

Assuming an initially uniform distribution of very small defects throughout the block, the gneiss sample has been considered an "equivalent porous medium" characterized by its porosity, as well as many other thermo-mechanical properties.

4.1.1 Governing equations

The frozen soil formulation presented builds from the THM modelling by Olivella et al. (1994, 1996) and Gens et al. (1998) of high-temperature problems involving a gas phase. Low-temperature problems can be considered with the same overall structure if the original gas phase is replaced by a new solid phase representing ice ([104] Nishimura et al., 2009). The formulation has been implemented in the FEM code CODE_BRIGHT ([113] Olivella et al., 1996) considering the new features required to address freeze/thaw conditions. CODE_BRIGHT is a program for thermo-hydro-mechanical analysis in geological media. It has been developed at the Department of the Geotechnical Engineering and Geosciences, Universitat Politécnica de Catalunya (UPC) combined with the pre/post-processor GiD developed by the International Center for Numerical Methods in Engineering (CIMNE).

Thermodynamic equilibrium of freezing soil

The equilibrium between liquid water and ice phases is described by the Clausius-Clapeyron equation, derived from equilibrium of the chemical potentials between two phases.
This equation is expressed as:

$$-(s_1 - s_2)\mathrm{d}T + \nu_1 \mathrm{d}P_1 - \nu_2 \mathrm{d}P_2 = 0 \tag{4.1}$$

where s and ν are the specific entropy and the specific volume respectively, T is temperature on the thermodynamic scale, and P is pressure. Subscripts 1 and 2 refer to each of two different phases/materials in equilibrium. When applied to equilibrium between pure ice and liquid water, equation 4.1 can be rewritten as:

$$-(s_l - s_i)dT + \nu_l \mathrm{d}P_l - \nu_i \mathrm{d}P_i = 0 \tag{4.2}$$

$$\mathrm{d}P_i = \frac{\rho_i}{\rho_l}\mathrm{d}P_l - \frac{\rho_i L}{T}\mathrm{d}T \tag{4.3}$$

where L is the specific latent heat of fusion, ρ $(1/\nu)$ is the mass density, and the subscripts l and i refer to liquid water and ice respectively. This differential form can be integrated using atmospheric pressure and the temperature 273.15°K as references, to give:

$$\mathrm{d}P_i = \frac{\rho_i}{\rho_l}\mathrm{d}P_l - \rho_i L \ln\left(\frac{T}{273.15}\right) \tag{4.4}$$

This equation represents a thermodynamic requirement for equilibrium that needs to be satisfied by P_i, P_l and T ([104] Nishimura et al., 2009).

Freezing characteristic function

The model requires a freezing characteristic function to relate the degree of liquid (unfrozen water) saturation S_l (i.e. volume of liquid phase/volume of pore) to the porous medium thermodynamic properties ([104] Nishimura et al., 2009). Many researchers have developed freezing characteristic functions through analogies with water retention models developed to describe the drying and wetting of unsaturated unfrozen soils, where gas and liquid phases coexist in the pores (e.g. [78] Koopmans & Miller, 1966; [97] Miller, 1978; [16] Black & Tice, 1989; [52] Grant & Sletten, 2002; [31] Coussy, 2005). The different pressures between the liquid water and ice phases expressed by the
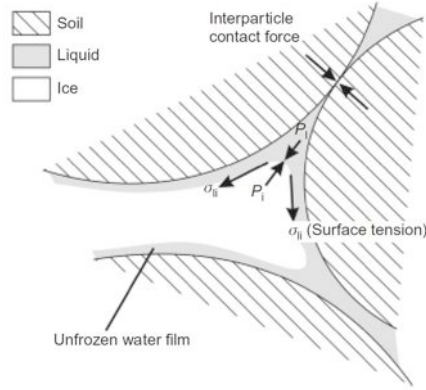
Figure 4.1: Surface tension forces developing along the interface between liquid water and ice phases in pores ([104] Nishimura et al., 2009).

Clausius-Clapeyron (equation 4.4) suggest that surface tension forces should develop along the interface between the two phases, as illustrated in Figure 4.1. The freezing characteristics and the water retention characteristics are both determined by the soil pore size distribution (e.g. [43] Fredlund & Xing, 1994; [31] Coussy, 2005) and the interface tension force. It is therefore natural to assume that the two functions can be expressed by similar forms of equation, once allowance is made for the difference between the ice/liquid and gas/liquid interface tension forces. The van Genuchten model ([154] van Genuchten 1980) was used here to represent the freezing characteristic function:

$$S_l = \left[1 + \left(\frac{P_i - P_l}{P} \right)^{\frac{1}{1-\lambda}} \right]^{-\lambda} \tag{4.5}$$

where P and λ are material constants. This equation represents the relationship between P_i, P_l and S_l ([104] Nishimura et al., 2009).

By combining equations 4.4 and 4.5, the freezing characteristic function relating S_l to T can be obtained as:

$$S_l = \left\{ 1 + \left[\frac{-(1 - \rho_i/\rho_l)P_l - \rho_i l \ln(T/273.15)}{P} \right]^{\frac{1}{1-\lambda}} \right\}^{-\lambda} \tag{4.6}$$

44

During prolonged freezing, water migrates and could be accumulated in a frozen fringe, i.e. a transitional zone just behind a freezing front, where the porous material is partially frozen (see Figure 3.8). The water migration is driven by cryogenic suction (represented by equation 4.5) but at the same time is impeded by the reduced permeability developed in partially frozen soil.

Mass/heat transfer

Mass conservation of pore water is expressed as:

$$\frac{\partial}{\partial t}(\rho_l S_l \phi + \rho_i S_i \phi) + \nabla \cdot (\rho_l \mathbf{q}_l) = f^w \tag{4.7}$$

where ϕ is the porosity; S_l and S_i are degrees of liquid and ice saturation respectively ($S_l + S_i = 1$, as neither a gas phase nor cavitation is considered); $\mathbf{q}_l$ is the liquid water flux vector; and f^w is the sink/source term of mass ([104] Nishimura et al., 2009). The water flux is calculated from generalised Darcy's law as:

$$\mathbf{q}_l = -\frac{k_r}{\mu_l}[k](\nabla P_l - \rho_l \mathbf{g}) \tag{4.8}$$

where $\mathbf{g}$ is the gravity acceleration vector, $[k]$ is the intrinsic permeability matrix, μ_l is the viscosity of liquid water, and k_r is the liquid phase relative permeability ([104] Nishimura et al., 2009). Viscosity (Pa $\times$ s) can be considered a function of the temperature, as:

$$\mu_l = 2.1 \times 10^{-6} \exp\left(\frac{1808.5}{273.15 + T}\right) \tag{4.9}$$

Relative permeability can be calculated from the expression:

$$k_r = \sqrt{S_l}\left[1 - \left(1 - S_l^{1/\lambda}\right)^\lambda\right]^2 \tag{4.10}$$

which can be derived from the van Genuchten function (equation 4.5). The parameter λ is a material constant that in principle coincides with that used in the retention curve and k_r varies between 0 and 1 ([104] Nishimura et al., 2009). The intrinsic permeability in the generalized Darcy's equation and the hydraulic conductivity $[K]$ (usually used in the flow equation when written in terms of piezometric head) are related by:

$$[K] = \frac{\rho_l g}{\mu_l}[k] \tag{4.11}$$

In the present study, all material properties have been considered isotropic. The energy conservation equation is written as:

$$\frac{\partial}{\partial t}\left[e_s\rho_s(1-\phi) + e_l\rho_l S_l\phi + e_i\rho_i S_i\phi\right] + \nabla \cdot (-\lambda_T\nabla T + \mathbf{j}_l^e) = f^e \qquad (4.12)$$

where e_s, e_l and e_i are the specific internal energy of solid phase minerals, liquid water and ice respectively; λ_T is in this case the overall thermal conductivity of the material (consisting of soil minerals and pore materials); $\mathbf{j}_l^e$ is the advective term of heat flux ($\mathbf{j}_l^e = e_l\rho_l\mathbf{q}_l$); and f^e is the sink/production term of energy. Fourier's law is employed in the above equation for calculating the conductive heat flux ([104] Nishimura et al., 2009). The overall thermal conductivity λ is calculated by using the geometric mean ([30] Côté and Konrad, 2005):

$$\lambda_T = \lambda_s^{1-\phi}\lambda_l^{S_l\phi}\lambda_i^{(1-S_l)\phi} \qquad (4.13)$$

where the subscript s denotes the soil mineral phase. The specific internal energies, e_s, e_l and e_i, are:

$$e_s = c_s T \qquad e_l = c_l T \qquad e_i = -l + c_i T \qquad (4.14)$$

where c_s, c_l and c_i are the specific heats for solid soil mineral, liquid water and ice respectively ([104] Nishimura et al., 2009).

Mechanical equilibrium

Mechanical equilibrium can be written as

$$\nabla \cdot \sigma + \mathbf{b} = 0 \qquad (4.15)$$

where σ are total stresses and $\mathbf{b}$ are body forces ([104] Nishimura et al., 2009).

4.1.2 Application of THM analysis to ice segregation processes in a rock sample

Ice segregation processes are caused by water migration and accumulation in a frozen fringe (i.e. a transitional zone just behind a freezing front, where rock is partially frozen), as explained in detail in section 3.5.

The water migration is driven by cryogenic suction (represented by equation 4.5) but at the same time is impeded by the reduced permeability developed in partially frozen rock.

A numerical study of the phenomenon can be done by solving the equations presented in section 4.1.1, using the finite element method.

Finite element meshes and boundary conditions

The spatial domain of the problem was discretized by designing a two-dimensional structured FE meshes (15x15 cm), made of 225 quadrilateral elements and 256 nodes ([112] Olivella et al., 1994): this is a rather coarse mesh, but it was a necessary compromise given the computational cost of coupled THM analysis.

A uniform temperature of 22°C was assumed as initial condition in the analysis. The hydraulic boundary conditions along the top boundary were set to give $P_l=0$, obtaining hydrostatic pore water pressures trough the sample.

The bottom boundary temperature reduced from 22°C to -12°C over the first 7 hours, simulating the upward freezing, and was then kept constant, while the upper surface temperature reached 3°C. Zero heat flux/liquid flux conditions were specified along the lateral mesh boundaries.

Regarding the mechanical boundary conditions, the displacement along x and y-axis have been given equal to zero on the lower surface of the sample.
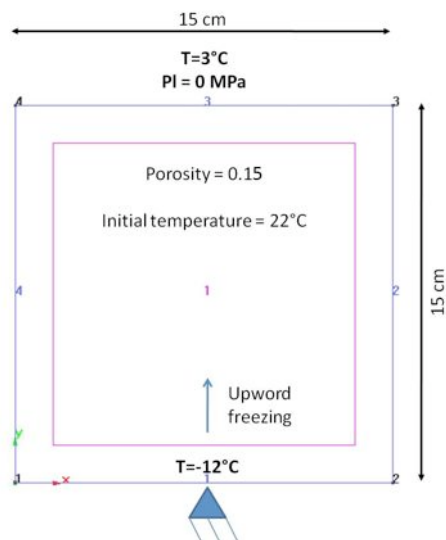
Figure 4.2: Model initial and boundary conditions.

Material parameters

The material parameters selected for input are summarized in Table 4.1.

Gneiss thermal conductivity value has been obtained in laboratory tests carried out at the Institute of Geosciences and Earth Resources of Pisa (thanks to Doctor Bellani) on a rock sample (Arolla gneiss); the specific heat value was set equal to 800 J/Kg K ([161] William & Smith, 1989). Water and ice thermal conductivity and specific heat values have been derived from literature data: λ_l=0.613 W/m K ([25] Cengel, 2003), c_l= 4180 J/Kg K ([25] Cengel, 2003), and λ_i=2.4 W/m K ([138] Shulson & Duval, 2009), c_i= 2110 J/Kg K ([138] Shulson & Duval, 2009). The specific latent heat of fusion was equal to 335000 J/Kg K ([138] Shulson & Duval, 2009).

There was a lack in knowledge of rock hydraulic properties: the parameters for the soil-water characteristic curve, P_0 and λ, were obtained by fitting equation 4.6 to the measured data determined by Borgesson and Hernelind ([19] Borgesson & Hernelind, 1999). Although the parameters λ in the soil-water characteristic curve (equation 4.5) and in the relative permeability function (equation permeability) do not need to be identical, the same value was chosen.

The two-dimensional sample cross-section was modelled with mechanical parameters obtained from laboratory tests carried out to determine strength and deformability in uniaxial conditions (MASTRLAB - Laboratorio Sperimentale Materiali e Strutture, Politecnico di Torino), as explained in paragraph 6.2. The axial Young's Modulus, E, has been calculated as the secant modulus at a stress level equal to 50% of the maximum strength (E=78000 MPa). The Poisson's ratio has been determined as the ratio between the slope of the axial and the radial strain curves, at the same stress level (ν=0.02).

As regards the elasto-plasticity, the value for the critical state parameter M was set as 2.25, which is equivalent to an angle of shearing resistance of 55°: this value was derived plotting uniaxial compression and indirect tensile test results and thus obtaining a Mohr-Coulomb failure envelope. The value of cohesion was equal to 10 MPa.

The solid phase density value is the one corresponding to the density calculated from laboratory tests on thermally-cracked Arolla gneiss specimens (Department of Environment, Land and Infrastructure Engineering, Politecnico di Torino) as reported in section 6.3.2. The initial porosity is derived from ultrasonic measurements conducted on thermally-cracked samples, applying Wyllie time-average equation (see equation 6.1). The model

available in fact, allowed the use of a spherical type porosity: the equation that links the elastic waves velocity with the porosity, valid for isodiameter pores, is Wyllie time-average equation. At this stage, this formulation was then used, as to obtain porosity value of the type required by the model.

Table 4.1: Arolla gneiss properties input in the analysis

Property	Value
Thermal	
Gneiss thermal conductivity, λ_s: W/m K	2.711
Water thermal conductivity, λ_l: W/m K	0.613
Ice thermal conductivity, λ_i: W/m K	2.4
Gneiss specific heat, c_s: J/Kg K	800
Water specific heat, c_l: J/Kg K	4180
Ice specific heat, c_i: J/Kg K	2110
Specific latent heat of fusion, l: J/Kg	335000
Hydraulic	
Rock-water characteristic curve	
P_0: MPa	0.05
λ	0.5
Intrinsic permeability, k: m^2	1E-14
Relative permeability	0.5
Mechanical	
Gneiss elasticity	
E: MPa	78000
ν	0.02
Gneiss plasticity	
m	3
Γ_0: s^{-1}	100000
c': MPa	10
M	2.25
Other	
Gneiss mass density, ρ_s: Kg/m^3	2759
Water mass density, ρ_l: Kg/m^3	1000
Ice mass density, ρ_i: Kg/m^3	916.4
Initial porosity, ϕ_0	0.15

Simulated upward freezing problem

A series of two-dimensional freezing simulations was performed, in order to study the interactions between frozen rock thermal, hydraulic and mechanical processes. Figure 4.3 shows the comparison between temperature obtained from CODE_BRIGHT and ABAQUS simulatios (see section 4.2) with the data collected during laboratory test concerning upward freezing. The temperature profile through the sample has been also plotted in Figure 4.4, once reached thermal equilibrium (solid blue line): the gradient is linear, and it can be seen again a good fitting with the laboratory data (red solid trend line): the red bullets correspond to the temperature measurements at the tip of the pt100 places at different depths of the sample. The zero-isotherm is located at a depth of 2.5 cm from the surface.

Figure 4.5 shows the trend of the liquid water saturation degree with depth: above 0°C, the pore water is completely in liquid phase (S_l=1). Below 0°C, S_l is still close to 1: the phase change begins to occur at about 3 cm depth, for T=-0.35°C, temperature that corresponds approximately to the "freezing point depression" in a variety of crystalline rocks ([157] Walder & Hallet, 1985).

It is possible to recognize a range between -3°C and 0°C in which considerable amount of water remains unfrozen, although the subfreezing temperature. In this zone, the pore space in only partially ice-filled (S_l decreases from 1 close to 0): borrowing the nomenclature of Miller ([97] Miller, 1978), this zone is defined as "frozen fringe". The temperature at the cold side of the frozen fringe is effective freezing temperature (below -3°C), and S_l is approximately equal to 1, i.e. the pore space is completely ice-filled; above the frozen fringe, the rock is instead unfrozen (S_l=1).

Figure 4.5 also shows the variation of the liquid saturation degree: it was used to calibrate and check the P_0 and λ values derived from literature. For instance, for higher P_0 values (P_0=0.5 MPa), the material does not desaturates, i.e. the space in the pores is not completely filled with ice, but water is still liquid (blue solid line in Figure 4.5).

The computed liquid flux (Figure 4.6) along the y-axis obtained after 24 hours from the beginning of freezing, demonstrates how the accumulation of freezing pore water drives the ice segregation process: the unfrozen pore water is drawn into the frozen fringe. The flux increases gradually from the freezing front down to the frozen fringe, at it reaches the maximum value and reaches the maximum value equal to 3.25E-07 Kg m^{-2}s^{-2} at 3 cm deep. At 5 cm depth, the flux changes sign, as the unfrozen water film between ice and substrate, tends to migrate toward the frozen rock to the freezing front ([156]

Walder & Hallet, 1985).

It can be noticed as -2°C is the critical temperature that controls permeability and consequently, water migration: slightly below this value, i.e. for depths less than 6 cm, the flow almost vanishes, marking the boundary between frozen fringe and completely frozen rock. At this depth, that corresponds to the isotherm -3°C, the maximum value of ice pressure is recorded (P_i=23 MPa), as shown in Figure 4.7 (red line: steady state after 24 hours from the beginning of freezing).

As temperatures are above -3°C, the frozen fringe is relatively permeable, and the fluid flow reaches the maximum value equal to 3.25E-07 $Kgm^{-2}s^{-2}$; however the ice pressure is only few MPa. At lower temperatures (T=-3°C), the maximum ice pressure is quite larger, but the liquid flux is definitely reduced due to the extremely low hydraulic conductivity of the frozen fringe there. Finally, sustained freezing should be most effective when temperature is around -3°C: at higher temperatures, thermodynamic limitations prevent ice pressure from building up sufficiently to produce significant crack growth, but at lower temperatures, the migration of water necessary for sustaining crack growth is strongly inhibited. The result is in agreement with the literature data, which suggested that the temperature at which ice segregation induces microgelivation in medium porosity hard rocks is lower then -3°C ([92] Matsuoka, 2001); Hallet also recognizes that most of the fracture activity (and consequently AE generation) occurs at temperature between -3°C and -6°C ([63] Hallet et al., 1991).

A map of the simulated porosity change is presented in Figure 4.8. A little increase of porosity from the initially set value of 0.15 is visible at depth of 6 cm, demonstrating how the accumulation of freezing pore water is maximum in this critical zone. As a matter of fact, the unfrozen pore water is drawn into the freezing front: in Figure 4.9 the profile of porosity as a function of depth is shown for three different time steps (i.e. 9, 14 and 24 hours from the beginning of freezing). It is interesting to note that the highest porosity value for each step coincides again with the deepening of zero-isotherm, and that this peak value increases with time. In fact, after the transient cooling, freezing at fixed temperature gradient allows the localization of increasing porosity precisely in that area, which should therefore be the preferential place for the ice lenses formation ([93] Matsuoka & Murton, 2008).
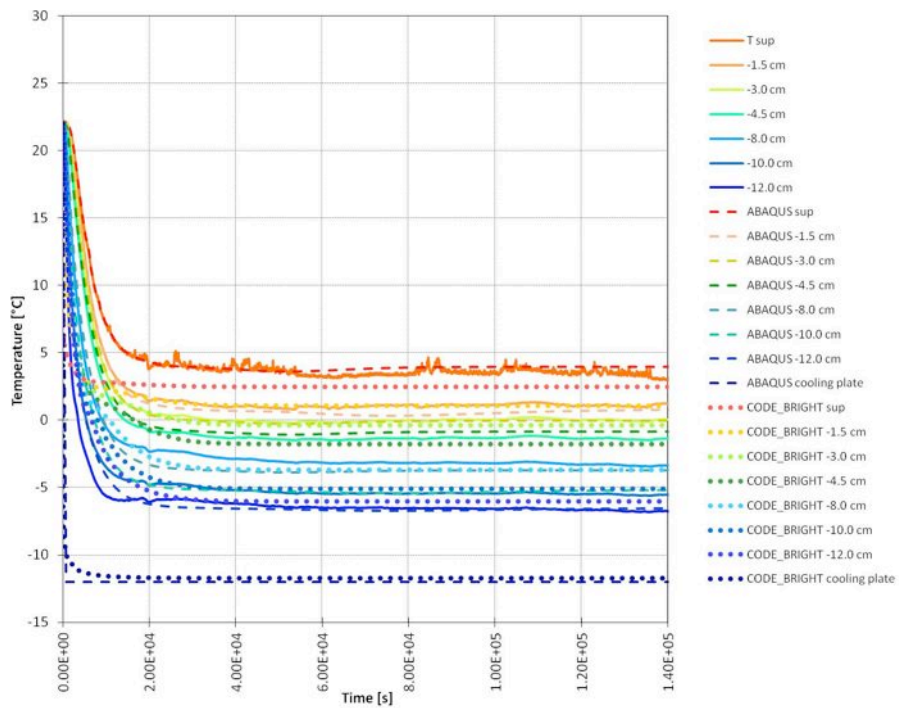
Figure 4.3: Comparison between the temperature profiles monitored during laboratory test (solid lines) and those obtained from CODE_BRIGHT and ABAQUS simulations (dashed lines).
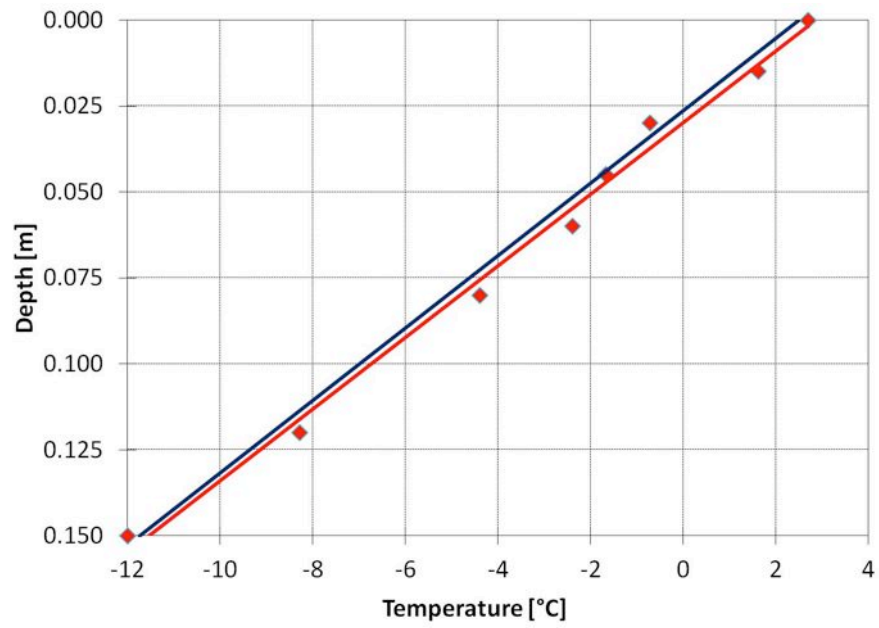
Figure 4.4: Temperature profile through the sample, once reached thermal equilibrium (solid blue line). The red bullets are the temperature measurements at the tip of the pt100 places at different depths of the sample; the red solid line is the corresponding linear trend line.
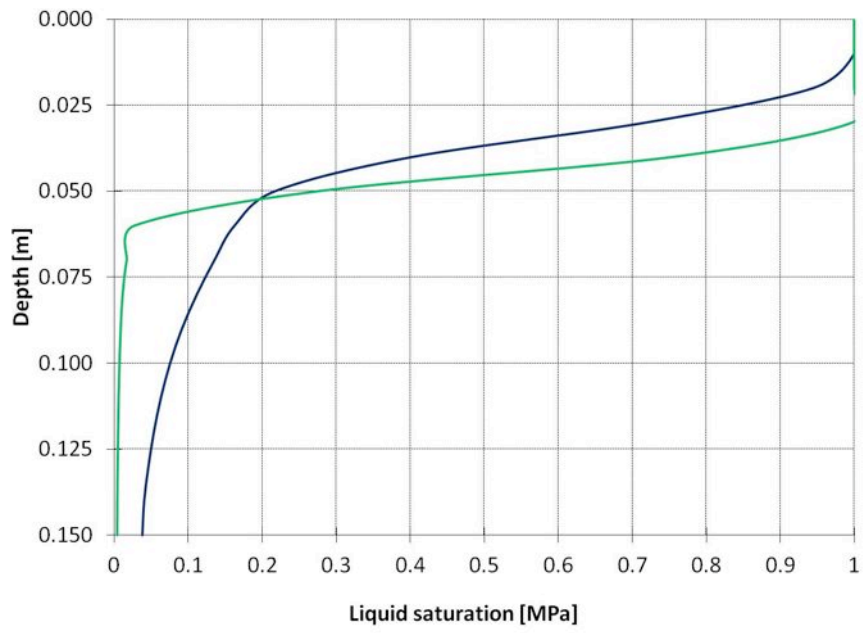
Figure 4.5: Liquid water saturation degree with depth for different models: P_0 value equal to 0.05 (green solid line), P_0 value equal to 0.5 (blue solid line).
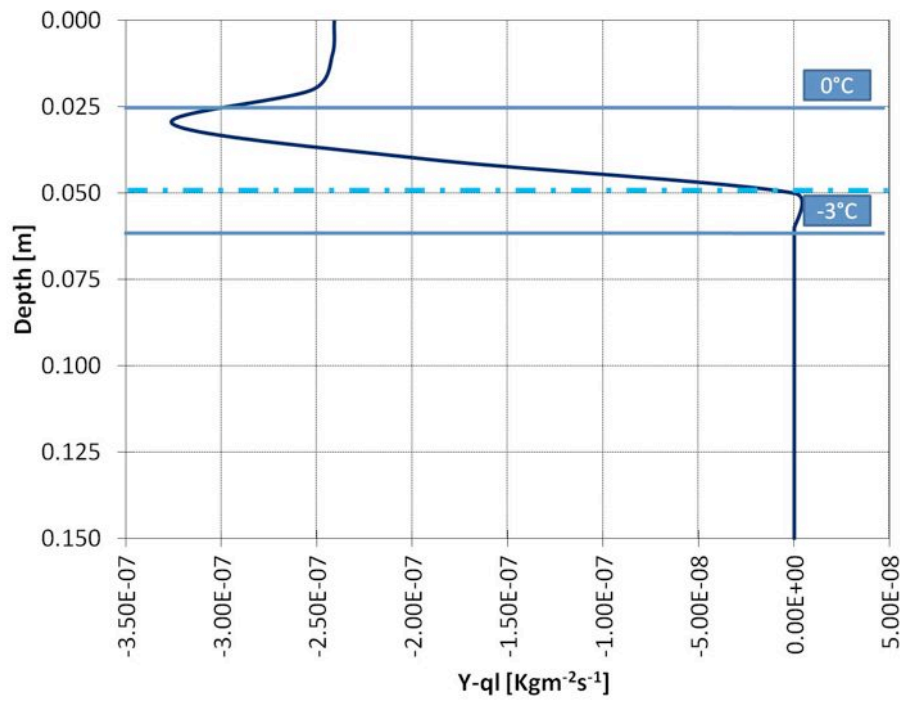
Figure 4.6: The computed liquid flux along the y-axis, after 24 hours from the beginning of freezing.
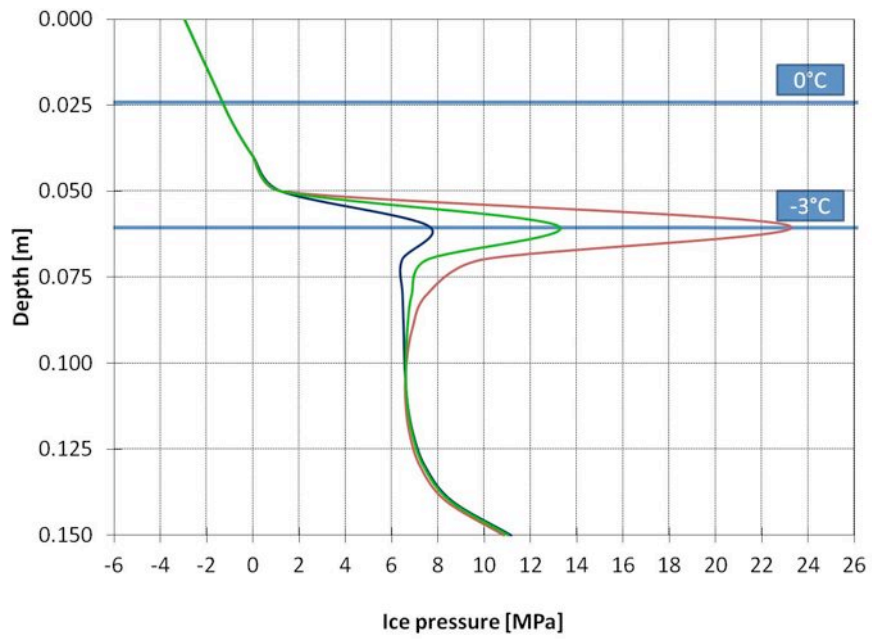
Figure 4.7: Comparison between the pressure profiles obtained after 9 (blue solid line), 14 (green solid line) and 24 (red solid line) hours of freezing.
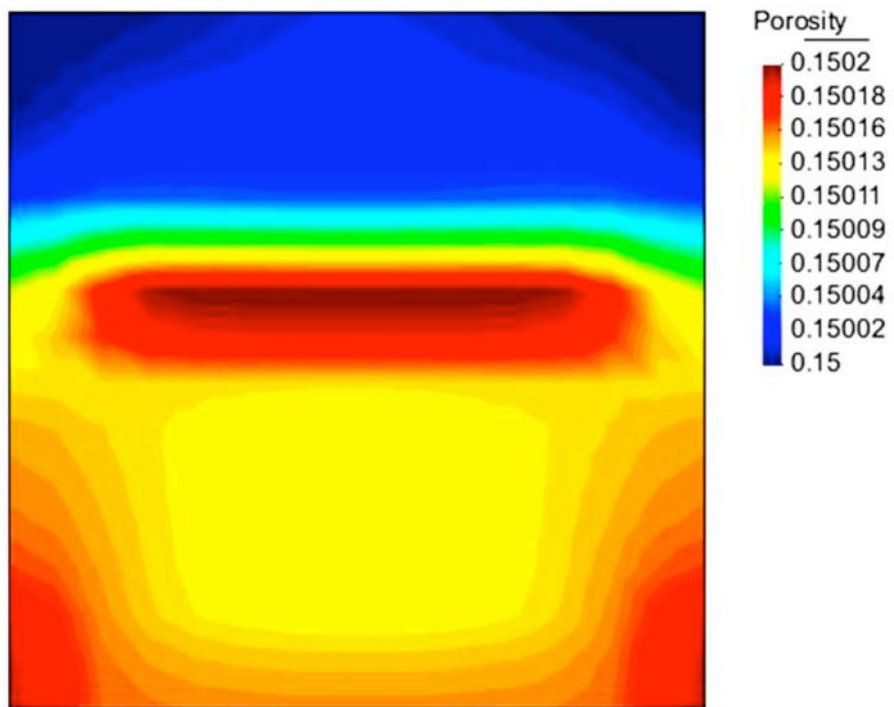
Figure 4.8: Porosity contour after 24 hours of freezing
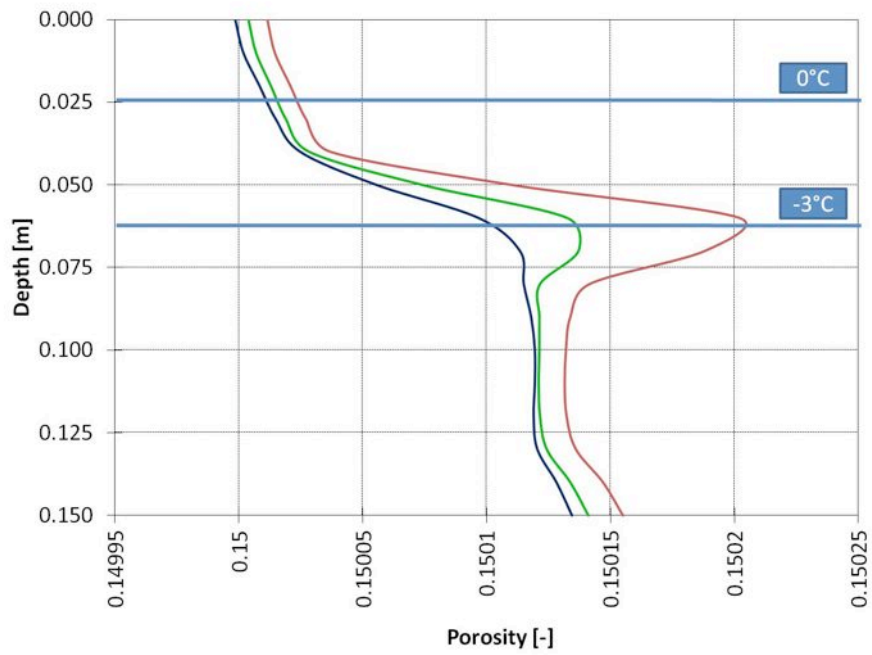
Figure 4.9: Comparison between the porosity profiles obtained after 9 (blue solid line), 14 (green solid line) and 24 (red solid line) hours of freezing.

4.2 Saturated microcracks propagation due to freezing

In order to evaluate the propagation of saturated microcracks due to freezing, uncoupled numerical analyses were performed using the FEM code ABAQUS, and developing two different models: a thermal model to evaluate temperature distribution over the specimen, and a structural model to evaluate the effect of stress distribution on crack propagation.

The study has been done considering a 2D section of the sample subjected to the laboratory test. Isotherms parallel to the rock cubic sample surface were monitored during the upward freezing: for this reason, a two-dimensional section could be representative of the thermal behavior.

The first objective was to study how the temperature distribution can induce a stress concentration at the microcrack-tip, due to the water volumetric expansion and to the stresses attributed to differential thermal expansion within the rock matrix. Different sets of crack-growth calculations have been done for cracks oriented parallel to the isotherms. "Single-crack" model has been built, pre-inserting a potential crack within the homogeneous rock sample: the crack has been modeled as solid region made of water with physical properties (i.e. thermal expansion coefficient) function of temperature. On left and right side of the each crack tip, cohesive elements have been inserted, in order to simulate the propagation mechanisms.

4.2.1 Modelling procedure and meshing

The geometry of the problem consisted in a square planar surface (150x150mm) representing the 2D section of the sample: within this region, a microcrack has been inserted, schematized as a rectangle of width 10 μm and length 1mm ([126] Rotonda, 1991). The crack has been placed below the active layer (i.e. below the zero degree isotherma) measured in the laboratory, at a depth of 45mm. The profile of the gneiss sample is shown in Figure 4.10.

Because of the sensitivity of the behavior at the crack tip, it was necessary to create a fine mesh to obtain an adequate estimate of the stress distribution around the discontinuity. On the contrary, the stresses inside the crack do not require a large number of elements, since the stress does not have singularities inside the domain: a coarser and structured mesh has been chosen for this region. Also in the thermal model, local variations of temperature near the crack, can have important effects: for this reason it was decided to have the
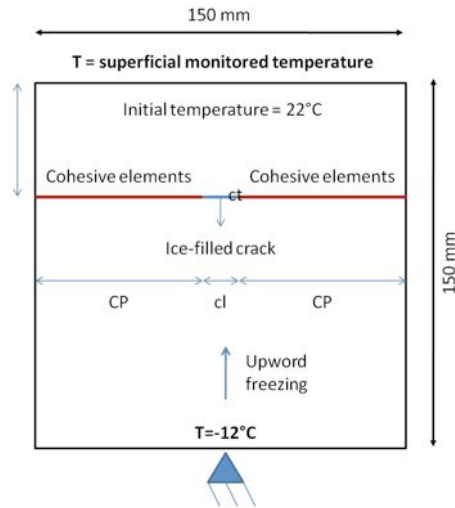
Figure 4.10: Model sketch and boundary conditions. Parametrized geometrical dimensions: AL = active layer depth, CP = crack position, ct = crack thickness and cl = crack length.

same mesh also for this implementation, since the computational costs were not excessive.

Appropriate seeding has been prescribed, in order to obtain a nonuniform distribution of elements along sample edges, by defining the size of the coarsest (far from the crack) and finest element (around the crack) along the edges (see Figure 4.11 b)).

Ice region was modeled with continuous cohesive element, allowing to use only one element in the crack thickness.

The mismatch that occurred between the nodes of the "crack region" and the nodes of the "gneiss region", required that the "crack region" have been generated as a separate mesh and tied to the rock material using tie constraints.

A tie constraint ties two separate surfaces together so that there is no relative motion between them. This type of constraint allowed to bond together the two regions, even though the meshes created on the surfaces of the regions may be dissimilar ([1] ABAQUS User's Manual, 2011).

The final mesh obtained has 491688 nodes and 164653 elements, as shown in

Figure 4.11 a).

A python script has been created in order to automatize the mesh generation on the domain, parameterizing each geometrical dimension (i.e. AL, CP, cl, ct in Figure 4.10) and mesh attributes. Different input files have then been generated for both thermal and structural models.
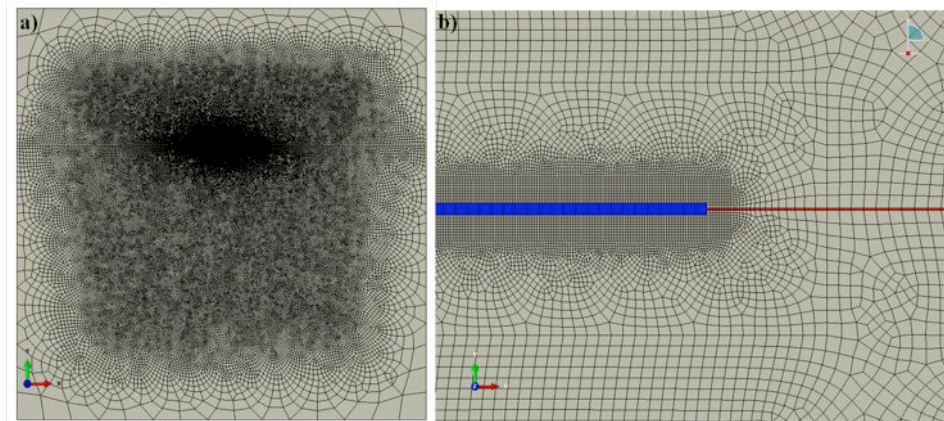
Figure 4.11: Finite element mesh: a) discretized domain, b) detailed view of the mesh around the crack tip: in blue "crack region", in grey "gneiss region" and in red "cohesive elements".

4.2.2 Simulation of heat transfer in freezing rock sample

Heat transfer in saturated freezing rocks is a complex process because of the coexistence of a multi-phase mixture of solid rock matrix, water and ice ([10] Adersland, 2004).

Three important effects associated with the freezing process are:

1. effect of the latent heat during the phase change of water,

2. nonlinearity of the soil thermal properties,

3. the existence of unfrozen water in frozen soil.

As the rock is subjected to freezing, liquid water inside pores and microcracks turns into ice. However, not all water freezes at the freezing temperature. The amount of unfrozen water drops as the temperature decreases, but some liquid

61

water is still present in frozen rocks at temperature well below 0°C.

As a result, the latent heat of fusion of water is released over a range of temperature rather than at one particular temperature. Release of the latent heat has a strong influence on the temperature profile and retards the frost penetration. As freezing front penetrates into the rock, thermal properties of the frozen material also change. The thermal conductivity and the heat capacity vary with the volumetric fractions of phases, which are dependent on the temperature ([161] Williams & Smith, 1989).

The effects of different temperature patterns on stress distribution nearby the microcrack have been studied, as explained in the following.

Thermal properties

Some assumptions have been made for the heat transfer analysis in the freezing rock sample:

- the heat transfer takes place by conduction only;

- the crack is fully saturated;

- the thermal conductivity of the rock sample is isotropic.

The heat conduction is described by the following differential equation:

$$\rho c \frac{\partial T}{\partial t} - L \rho_i \frac{\partial \Theta_i}{\partial t} - \nabla \left(\lambda_T \nabla T \right) = 0 \qquad (4.16)$$

where, T is the temperature, t is the time, ρc is the volumetric heat capacity of the gneiss sample, ρ_i is the density of ice, Θ_i is the volumetric fraction of ice, L is the latent heat of fusion per unit mass of water (approximately 333.5 kJ/kg, in a freezing range equal to -3°C $< T <$ 0°C ([138] Schulson & Duval, 2009)), $\nabla = \frac{\partial}{\partial x} + \frac{\partial}{\partial y} + \frac{\partial}{\partial z}$ is the gradient operator, and λ is the effective thermal conductivity of the gneiss sample. The first term in equation 4.16 represents the change in energy storage with respect to time. The second term represents the rate of the latent heat released during the change of water into ice. The third term represents the net energy flow by conduction ([161] William & Smith1989, [107] Noetzli et al., 2007).

The typical values of water physical and thermal properties are listed in Table 4.2, function on temperature. Arolla gneiss properties are listed in Table 4.1: they have been evaluated during laboratory tests, as explained in 4.1.2. These values have been used in the simulations.

62

Table 4.2: Water physical and thermal properties ([138] Schulson & Duval, 2009).

Temperature	Density	Thermal Conductivity	Volumetric Heat Capacity
°K	kg/m^3	W/mK	J/kgK
283.15	999.8	0.581	4193
278.15	1000	0.571	4204
273.16	999.8	0.563	4210
273.15	916.2	2.22	2050
268.15	917.5	2.25	2027
263.15	918.9	2.3	2000
258.15	919.4	2.34	1972
253.15	919.4	2.39	1943
248.15	919.6	2.45	1913
243.15	920.0	2.5	1882
238.15	920.4	2.57	1851
233.15	920.8	2.63	1818
223.15	921.6	2.76	1751
213.15	922.4	2.9	1681
203.15	923.3	3.05	1609
193.15	924.1	3.19	1536
183.15	924.9	3.34	1463
173.15	925.7	3.48	1389

Table 4.3: Arolla gneiss physical and thermal properties.

Density	Thermal Conductivity	Volumetric Heat Capacity
kg/m^3	W/mK	J/kgK
2774.46	2.711	800
(Lab. test DIATI Torino)	(Lab. test CNR Pisa)	(William, 1989)

Two dimensional freezing problems

In the single-crack model, the pre-existing defect measured 1 mm in length and 10 μm in thickness, as shown in Figure 4.10: this has been placed in the

center line of the sample, and the depth has been chosen depending on the analysis carried out.

In this way two regions have been identified, characterized by two different behaviors: gneiss, whose characteristics are listed in Table 4.3, and the crack, considered to be saturated with water and whose characteristics are reported in Table 4.2.

Plain strain ABAQUS standard elements DC2D4 have been chosen to discretize the model. The finite element mesh is shown in Figure 4.11.

The thermal model has been simulated, in order to study an upward freezing mechanism followed by a temperature gradient kept constant after the thermal equilibrium was reached. This situation is the one reproduced in laboratory: the thermal profile correspond to a long term freezing at fixed gradient, which should maximize the ice segregation process. The single-crack has been inserted, just below the maximum depth of the zero-isotherm.

The initial temperature was 295.15°K and lateral insulation kept the isotherms parallel to the upper surface. The temperature at the lower surface has then been dropped to 260.15°K suddenly, and freezing front started to go upward. The temperature distribution dropped down quickly during the first hour, and the heat transfer mechanism reached the steady state after about 7 hours.

The frost penetration is shown in Figure 4.12 as a function of time, while the temperature profiles for different instances are shown in Figure 4.13: it can be noted how the thermal equilibrium corresponds to a linear temperature gradient (magenta solid line).

Figure 4.3 shows the comparison between the temperature evolution during freezing at different depth obtained from the laboratory test, the CODE BRIGHT simulation, and the thermal model results: the temperature maps obtained for each time step, have been included in the structural-mechanic simulation, as will be fully explained in the previous paragraph (4.1.2).

4.2.3   Crack propagation model

The rock sample sketch has been characterized with three different element kinds, each one having its own characteristics.

Plain strain elements CPE4R have been chosen to model the homogeneous rock region: gneiss properties are listed in Table 4.4 and they derived from laboratory tests, as described in section 6.2.

As explained above, the saturated crack has been modeled as solid regions made of water with the thermal expansion coefficient, which is a physical properties, function of temperature (see Table 4.5, derived from literature. The

64
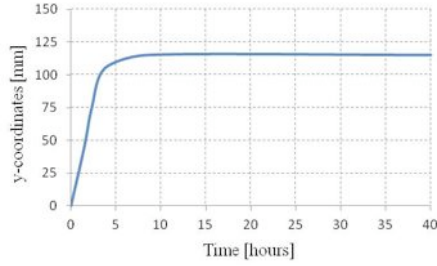
Figure 4.12: Frost penetration as a function of time.

Table 4.4: Arolla gneiss properties.

Density	Young modulus	Poisson's ratio	Expansion Coefficient
kg/m^3	MPa	-	K^{-1}
2759.46	112000	0.23	$3.30 \cdot 10^{-6}$

crack has been modeled using 4-noded continuum-cohesive elements COH2D4. The constitutive response of cohesive elements modeled as continuum has been defined in terms of macroscopic material properties: Young modulus and Poisson's ratio are listed in Table 4.6, function of temperature.

On left and right side of the crack, "cohesive elements" (COH2D4) have been pre-inserted into a narrow band ahead of the tips, in order to evaluate the rock fracture behavior and propagation mechanisms ([149] Tijssens et al., 2000). In fact, since the isotherms are parallel to the surface and to the schistosity and the defect was placed with the largest dimension along this direction, the crack path has been hypothesized a priori.

The cohesive elements constitutive behavior has been defined by a traction-separation relation ([137] Scheider, 2001): the traction acting on a cohesive element monotonically degrades as the separation displacement between the two outer surfaces increases after damage initiation ([135] Sarris & Papanastasiou, 2011). Therefore cohesive elements have been described by two independent parameters for mode-I plane strain ([40] Feih, 2005), fracture energy (G_{IC}=100Nm) and the tensile strength (σ_t=2.7MPa), derived from laboratory tests.

The initial response of cohesive elements has been assumed to be linear elastic

65
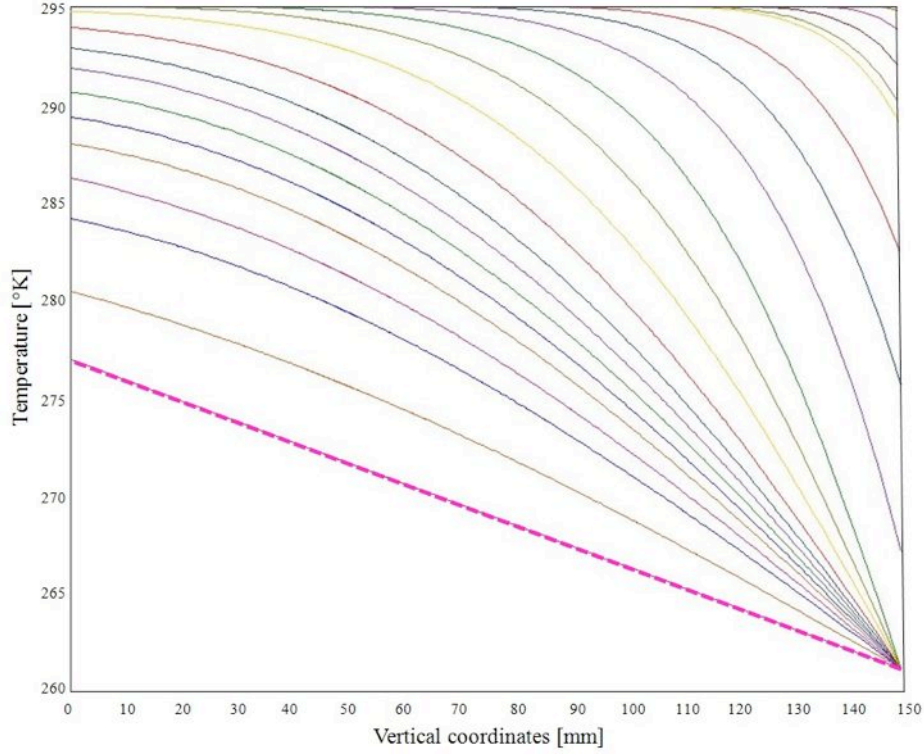
Figure 4.13: Temperature profiles.

before damage initiation ([131] Sancho et al., 2007): the tensile stiffness before the tensile strength has been reached, has been chosen equal to the un-cracked rock material (see Table 4.4).

This study assumed that damage initiated, when a quadratic interaction function involving the nominal stress ratios, reached a value of 1 ([17] Bonifaz, 2011):

$$\left\{ \frac{\langle t_n \rangle}{t_n^0} \right\}^2 + \left\{ \frac{t_s}{t_s^0} \right\}^2 = 1 \tag{4.17}$$

where t_n and t_s are the two components (2D problem) of the nominal stress vector, normal and tangential respectively, across the crack surface; t_n^0 and t_s^0

66

Table 4.5: Water thermal expansion coefficient ([138] Schulson & Duval, 2009).

Temperature	Expansion Coefficient
°K	K^{-1}
283.15	$8.80 \cdot 10^{-5}$
282.15	$7.00 \cdot 10^{-5}$
281.15	$6.00 \cdot 10^{-5}$
280.15	$4.00 \cdot 10^{-5}$
279.15	$3.00 \cdot 10^{-5}$
278.15	$1.60 \cdot 10^{-5}$
277.15	$3.10 \cdot 10^{-7}$
276.15	$-1.00 \cdot 10^{-5}$
275.15	$-3.00 \cdot 10^{-5}$
274.15	$-5.00 \cdot 10^{-5}$
273.15	$-6.00 \cdot 10^{-5}$
253.15	$-5.30 \cdot 10^{-5}$

represent the tensile and the shear strengths in the corresponding directions, respectively.

A damage evolution law has been used to describe the rate at which the material stiffness is degraded once the corresponding initiation criterion is reached ([163] Yang et al., 2009). A scalar damage variable, D, represented the overall damage in the material and captured the combined effects of all the active mechanisms. For a linear softening law, the damage evolves according to ([163] Yang et al., 2009):

$$D = \frac{\delta_{mf} \left(\delta_{m,max} - \delta_{m0} \right)}{\delta_{m,max} \left(\delta_{mf} - \delta_{m0} \right)} \qquad (4.18)$$

where $\delta_{m,max}$ is the maximum effective relative displacement attained during the loading history. δ_{m0} and δ_{mf} are effective relative displacements corresponding to δ_{n0} and δ_{s0}, and δ_{nf} and δ_{sf} respectively.

Equation 4.18 indicates that D monotonically evolves from 0 to 1 upon further loading after the initiation of damage. Damage evolution has been defined based on the fracture energy dissipated as a result of the process, which is a material property.

The stress components of the traction-separation model have been affected by

67

Table 4.6: Water/ice Young modulus and Poisson's ratio, function of temperature (Godbout et al. 2000).

Temperature °K	Young modulus MPa	Poisson's ratio -
261.15	6978.4	0.325
262.15	6905.2	0.325
263.15	6832	0.325
264.15	6758.8	0.325
265.15	6685.6	0.325
266.15	6612.4	0.325
267.15	6539.2	0.325
268.15	6466	0.325
269.15	6392.8	0.325
270.15	6319.6	0.325
271.15	6246.4	0.325
272.15	6173.2	0.325
273.15	0.1	0.325
293.15	0.1	0.325

the damage according to ([163] Yang et al., 2009):

$$t_n = \begin{cases} (1 - D)\,\bar{t}_n, & \bar{t}_n \geq 0 \\ \bar{t}_n & \bar{t}_n < 0 \end{cases}$$

$$t_s = (1 - D)\,\bar{t}_s$$

(4.19)

where $\bar{t}_n$ and $\bar{t}_s$ are the traction components predicted by the elastic traction-separation behavior for the current separation without damage.

Preliminary structural analysis

In a first step, some analysis were conducted in order to validate the structural model, understand the mechanical effects resulting from imposed temperature distributions, and to ensure its correspondence with literature data. The simulations also provided insight into the interdependence of temperature, temperature gradient, and pressure within a growing microcrack.

Thermal analysis have been performed applying three different temperature

distributions throughout the rock sample (Figure 4.14), imposing that the temperature on the lower surface was equal to 260.15°K. The initial temperature of the sample was 295.15°K and lateral insulation was imposed to keep the isotherms parallel to the upper surface.
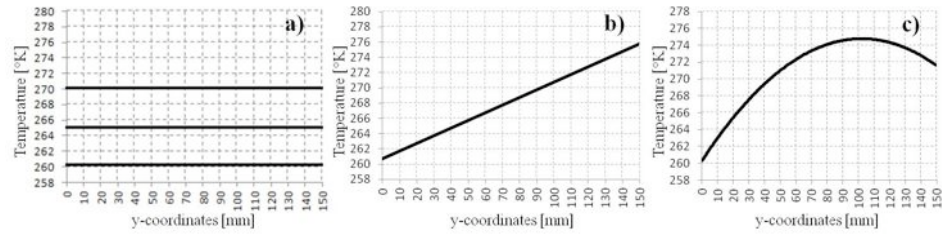
Figure 4.14: Temperature distributions applied throughout the rock sample: a) uniform (260.15°K, 265.15°K and 270.15°K), b) linear and c) parabolic temperature distribution.

The first temperature distribution was uniform, and equal to 260.15°K, 265.15°K, 270.15°K: these cases should represent the behavior of a crack in the permafrost table, at three constant subfreezing temperature. In the second case, a linear temperature distribution along y-axis has been applied, by imposing a gradient of 2.5°/cm. This situation should be representative the thermal equilibrium (being the gradient linear), at the interface between active layer and permafrost: in fact the upper part of the sample results to be thawed, while the lower frozen. The crack has been placed to a depth of 4.5cm, i.e. just below the zero-isotherm. The third thermal model has been developed by imposing a parabolic temperature profile, with the vertex in correspondence of the crack: the defect therefore resulted to be at a temperature equal to 275.15°K, trapped between two freezing fronts. This wanted to play a freezing period during which the upper part of the sample froze both from the upper surface downwards and from the lower surface upwards, simulating two-sided freezing of an active layer.

Regarding the mechanical boundary conditions, the displacement along x and y-axis have been given equal to zero on the lower surface of the sample.

Figure 4.15 compares two stress distributions around the crack right tip due to the volumetric expansion of ice after the application of two different uniform temperature on the sample: 260.15°K in Figure 4.15a) and 270.15°K in Figure 4.15c). 260.15°K is approximately the lowest temperature of the rock recorded in the reference site of the Matterhorn (see section 3.3); 270.15°K is the upper

69

limit of the so-called "frost cracking window", which is the temperature interval that maximize the frost cracking mechanism in hard intact rocks ([62] Hales & Roering, 2007). It can be seen that for both cases, tensile stress at the crack tip induces propagation: this is displayed through the damage index of cohesive elements. The red element corresponds to $D = 1$, which means that the element is broken, and the fracture propagates: for $T = 260.15°$K crack length increases by 6.5% (Figure 4.15b)), whereas for $T = 270.15°$K it increases by 2.8% (Figure 4.15d)).

It can also be noticed as the crack appears instead compressed, as a result of the expansion mechanism of the ice that stresses on fracture walls and causes tensile stress concentration at the tip.

Figure 4.16 shows the results in terms of stress distribution around the crack tip and the damage index, which shows the fracture propagation, for linear and parabolic temperature profiles within the sample (see Figure 4.14b) and c)). In both cases, the fracture is located at temperatures slightly above zero thermal, but despite this, there is a propagation mechanism. This highlights how steady temperature gradients play a fundamental role in crack propagation, resulting tense not only for the volumetric expansion of the ice contained within, but also because of opposite deformations (contraction in the lower, colder part and expansion in the upper warmer part) of the rock matrix that contains the defect.

The increase of the crack length at the end of the fracture propagation mechanism is equal to 6.5% in the case of linear temperature profile applied to the sample, and to 3.6% in the case of parabolic profile.
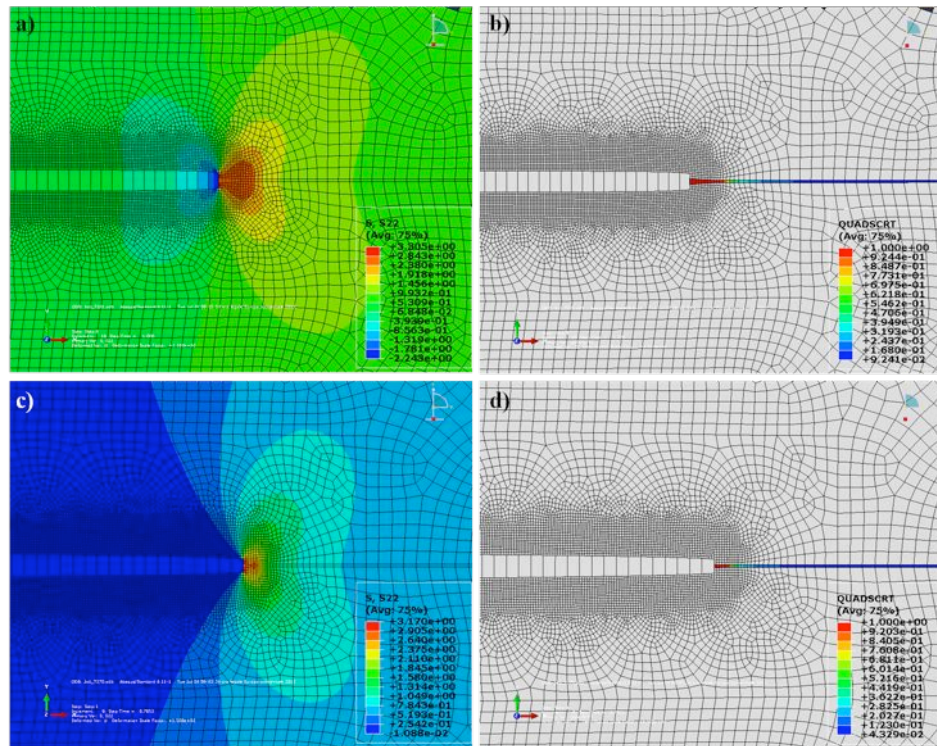
Figure 4.15: a) σ_{YY} distribution at the crack tip for $T = 260.15°$K; b) fracture propagation for $T = 260.15°$K (red color: $D = 1$); c) σ_{YY} distribution at the crack tip for $T = 270.15°$K; d) fracture propagation for $T = 270.15°$K (red color: $D = 1$).
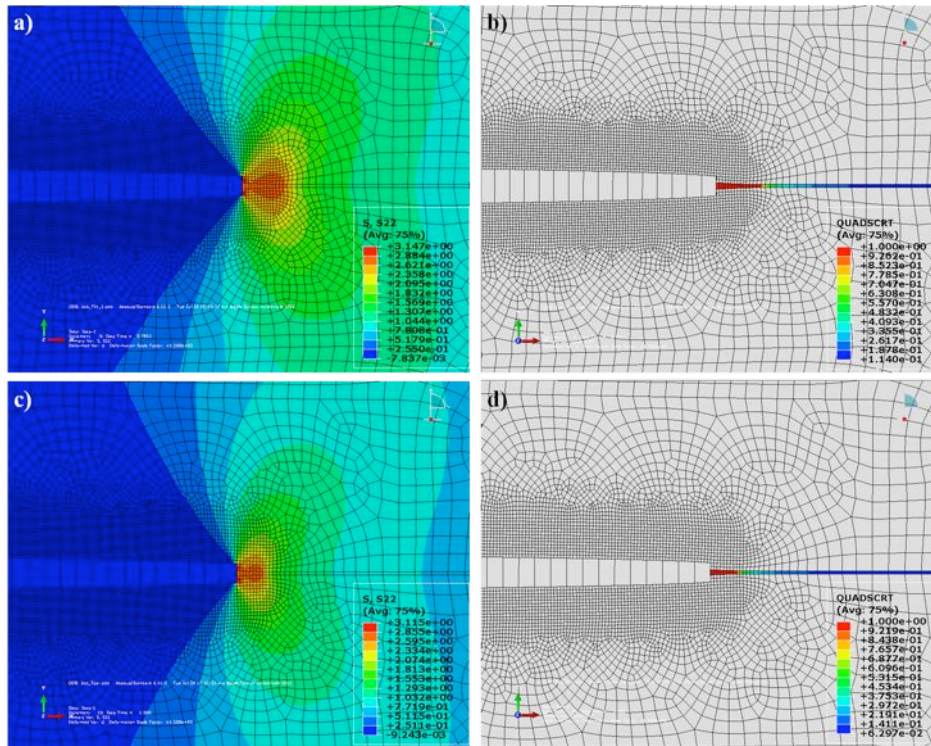
Figure 4.16: a) σ_{YY} distribution at the crack tip for linear temperature profile; b) fracture propagation for linear temperature profile (red color: $D = 1$); c) σ_{YY} distribution at the crack tip for parabolic temperature profile; d) fracture propagation for parabolic temperature profile (red color: $D = 1$).

Chapter 5

Experimental pilot study

5.1 Introduction

As the mechanical breakdown of macroscopically unfractured rock is the manifestation of the growth and interconnection of microfractures, monitoring the microcracking activity during freezing tests has been considered a powerful technique to study fundamental details of frost weathering ([63] Hallet et al., 1991).

In order to verify the relation between acoustic emission and temperature variations in a saturated material in controlled condition, experimental laboratory prototype has been designed and set up at the Laboratoire de Geophysique Interne et Tecnophysique, Université Joseph Fourier, Grenoble in cooperation with Professor Amitrano.

This pilot trial has been necessary in order to test the methodology and to identify the difficulties connected with the application of thermal cycles to a saturated rock sample, monitoring microcrack activities.

The freezing water is often invoked as playing a major role in the damage accumulation in shallow rocks, particularly in zone where transient permafrost may appear, as high altitude rocky cliffs.

Rocks at freezing temperatures contain varying amount of ice, liquid water and air, depending on the degree of water saturation and temperature; the damage is induced by the volume change of water included in the microcracks network, and also by the water migration via thin films from unfrozen zones to growing ice lenses (see Chapter 3.5).

A number of recent theories and laboratory experiments have addressed the prime role of ice segregation in intact rocks (e.g. [156] Walder & Hallet, 1985, [3] Akagawa & Fukuda, 1991, [101] Murton et al., 2000, [29] Chen et al., 2003, [102] Murton et al., 2006, [128] Saad et al., 2010). Most studies use intact rock samples with medium (5-20%) to high (>20%) porosity. This is because, firstly, intact rocks allow to correlate rock properties with frost sensitivity and, secondly, high porosity rocks are generally vulnerable to weathering (e.g. [89] Matsuoka, 1990).

In contrast, many field studies concern weathering of low porosity (<5%) but jointed rocks, which compose most of the high mountains in the world. The formation and growth of microcracks in rock material is accompanied by a sudden release of stored elastic energy that propagates as elastic waves. These latter can be detected, at the laboratory scale, by an array of acoustic emission (AE) sensors.

While in the laboratory studies cited above, the appearance of ice lenses was monitored by measuring heave and settlement of the block surface with different techniques (e.g. linear voltage displacement transformer, CCD camera, time-laps photography and Geo PIV analysis, X-ray radiography technology etc.), the idea of this research is rather to locate the area where the microgelivation is more active (which should correspond to the appearance of a macroscopic ice lens) using acoustic monitoring techniques.

The aim of this preliminary research has been to assess the role of the temperature gradient in this phenomenon by laboratory experiments: as a matter of fact the temperature gradient plays a major role as it determines the spatial repartition of frozen and unfrozen pore water.

The lower surface of a cubic shape sample has been maintained at subzero temperatures, while the upper surface has been cyclically frozen and thawed, simulating the temperature cycles in an active layer above permafrost. The sample used in the experiments was cubic shape measuring $15 \times 15 \times 15$ cm: this large size was necessary to provide sufficient depth to permit freezing and thawing of a thin artificial active layer above permafrost.

The pattern of the temperature variation has been chosen in order to induce different values of thermal gradient within the rock sample.

Unfrozen water could get trapped between the frozen zones near the surface and at depth: this case is particularly interesting because it has been observed in natural conditions that this pattern corresponds to high microseismic activity. Acoustic emissions have been recorded while the rock sample was subjected to different temperature gradients.

74

5.2 Material characterization

The rock used in the experiments was primarily considered to be the gneiss collected from the Matterhorn site, but since the area is difficult to access, it was decided to try a type of gneiss easier to find. Initially the Luserna stone was considered a suitable material, since there are many quarries in the Piedmont area.

Studying the geological map of the Aosta Valley, it has been noticed that the gneiss of the Matterhorn belongs to the type "Arolla gneiss". This type of gneiss crops out also in Pelline Valley where several samples have been taken.

In order to study these types of gneiss, thin sections have been analyzed and laboratory tests have been performed to determine open porosity, apparent density and thermal conductivity of the specimens.

5.2.1 Thin sections

Thin sections of Luserna gneiss, Arolla gneiss and samples taken from the Matterhorn, have been analyzed at the Department of Mineralogy and Petrology, Universitá di Torino in cooperation with Professor Borghi, with the intention of determining which of the Luserna stone and Arolla gneiss was more comparable to the Matterhorn gneiss: representative thin sections of these three material are showed in Figure 5.1 and the mineralogical composition of the three types of gneiss is summarized in the table 5.1. The Arolla gneiss has been finally identified as the material suitable for testing.

Table 5.1: Mineralogical composition of Luserna, Arolla and Matterhorn gneiss sample obtained by the analysis of thin sections.

	Luserna gneiss	Arolla gneiss	Matterhorn gneiss
quartz	35%	40%	40%
plagioclase	25%	4%	4%
K-feldspar	20%	20%	15%
muscovite	10%	20%	30%
biotite	5%	-	1%
epidote	3%	15%	10%
opaque	2%	1%	-
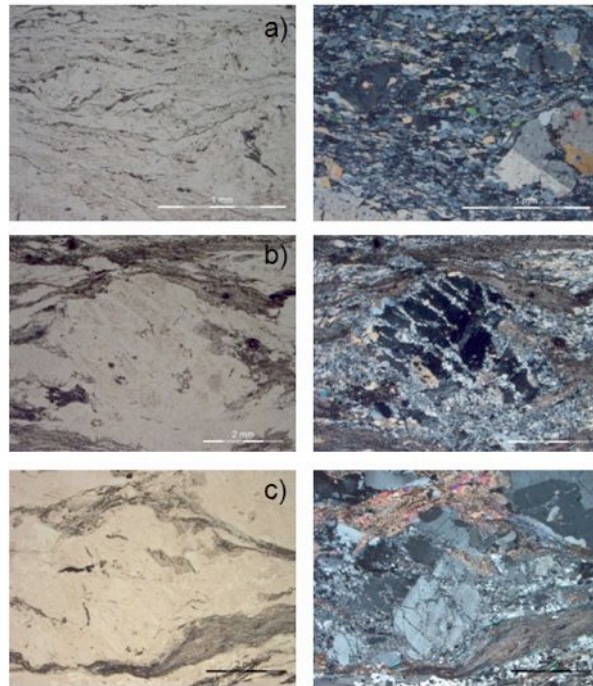
Figure 5.1: Photomicrograph of a) Luserna gneiss, b) Matterhorn gneiss, c) Arolla gneiss, in plane-polarized light on the left, cross-polarized light on the right.

5.2.2 Open porosity, density and thermal characteristics

Laboratory tests have been performed at the Department of Land, Environment and Geo-engineering, Politecnico di Torino in cooperation with Professor Marini, in order to determine open porosity and apparent density of the Luserna gneiss, Arolla gneiss and Matterhorn gneiss cubic shape samples: their dimensions were $5 \times 5 \times 5$ cm.

The specimens were dried at 70°C in a ventilated oven until a constant mass has been reached: this was assumed to have been attained when the difference between the two weighing at an interval of 24 h is not greater than 0,1% of the mass of the specimen.

The specimens were kept in a desiccator until room temperature was attained.

Each specimen was weighed (m_d indicates the dry mass) and then the specimens were put into a evacuation vessel where the pressure has been lowered gradually to 2 kPa=5 mmHg. This pressure has been maintained for 2 h in order to eliminate the air contained in the open pores of the specimens.

Demineralized water was slowly introduced at 20°C into the vessel, maintaining the pressure of 2 kPa during the water filling. When the specimens were immersed, the vessel was returned to atmospheric pressure and the specimens were left under water for another 24 h at atmospheric pressure. Then each specimen:

- was weighed under water and the mass in water was recorded: m_h;

- was quickly wiped with a dampened cloth and the mass of the specimen saturated with water was determined: m_s.

The apparent density (in kilograms per cubic meter) is expressed by the ratio of the mass of the dry specimen and its apparent volume, by the equation:

$$\rho_b = \frac{m_d}{m_s - m_h} \cdot \rho_{rh} \tag{5.1}$$

where ρ_{rh} indicates the density of water at 20°C equal to 998 kg/m^3.

The open porosity is expressed by the ratio (as a percentage) of the volume of open pores and the apparent volume of the specimen, by the equation:

$$p_o = \frac{m_s - m_d}{m_s - m_h} \cdot 100 \tag{5.2}$$

Open porosity values obtained for samples collected from the Matterhorn, for Luserna and Arolla gneiss, are listed in Table; apparent density values are also reported.

Thermal characteristics

Thermal conductivity tests have been carried out at the Institute of Geosciences and Earth Resources of Pisa (thanks to Doctor Bellani) on a sample of rock (Arolla gneiss) collected from Pelline Valley.

The tests have been made using an instrument Showa Denko "quick thermal conductivity meter - Shoterm QTM", which performs measurements using a transient linear heat source, directly returning a value of thermal conductivity in W/mK.

The accuracy of the instrument on a single measure is certified by the

77

Table 5.2: Open porosity and apparent density values obtained for samples collected from the Matterhorn, for Luserna and Arolla gneiss.

	p_o [%]	ρ_b [Kg/m^3]
Matterhorn	1.39	2694.99
Luserna	0.92	2608.30
Arolla	1.03	2774.46

manufacturer in $\pm 5\%$.

The probe has a flat surface of 9.5×4 cm crossed along the longer side by a heating wire; at the center of this wire is applied to a thermocouple. The measurement is taken at the contact between the wire and thermocouple.

As a result, anisotropic rocks can provide a considerable variability in thermal conductivity: to overcome this problem, 48 measures have been performed in different parts of the sample, and then an average value has been calculated.

On each of the two surfaces were then performed two sets of measurements in two orthogonal directions, respectively parallel and perpendicular to the schistosity.

The probe was always positioned in different points on the sample, as to minimize the effects of anisotropy and the influence that individual minerals with high thermal conductivity can give.

The probe QTM does not return a vertical thermal conductivity but it is necessary to combine two values measured respectively parallel and perpendicular to the schistosity of the sample: $\lambda_T = (\lambda_{parallel})^2 / \lambda_{orthogonal}$.

The value of thermal diffusivity of the Arolla gneiss has been then calculated using the following equation:

$$\alpha_T = \frac{\lambda_T}{\rho c_P} \tag{5.3}$$

where λ_T is the thermal conductivity and ρ is the density, both obtained by the laboratory tests, and c_p is the heat capacity at constant pressure derived from literature. The characteristics of the Arolla gneiss are listed in Table 5.3.

Table 5.3: Characteristic of the material

Characteristic of the material - Arolla gneiss	
Open porosity	$P_0 = 1.03$ %
Density	$\rho = 2774.46$ kg/m^3
Thermal conductivity	$\lambda_T = 2.711$ W/mK
Heat capacity (constant pressure)	$c_P = 800$ J/kgK
Thermal diffusivity	$\alpha_T = 1.3 \cdot 10^{-6}$ m^2/s

5.3 Description of experimental apparatus

In the following, a detailed description of the apparatus used for the preliminary tests is reported.

The experiments have taken place in a cold room at the Laboratoire de Geophysique Interne et Tecnophysique, Université Joseph Fourier, Grenoble in cooperation with Professor Amitrano.

The sample, saturated first by capillary rise, was placed on a basal CP-121 cooling plate, specifically designed and assembled by TE Technology (Figure 5.2a)), to permit upward freezing and therefore ensure the persistence of simulated permafrost in the lower half of the gneiss block. This type of cooling plate is ideal for medium to large heat loads and provides effective direct-contact cooling: the temperature of the cooling plate was regulated by a thermoelectric controller (Figure 5.2b)). Cooling plate general specifications are attached in Annex C (see Table C.1).

The top of the sample was directly in contact with the ambient air of the freezer, permitting downward cooling of the block by the chilled air circulation system in the cold room: it has been considered as an analog of the free surface of a stiff cliff in mountain areas, which is subjected to different thermal cycles of freezing and thawing following different temperature patterns.

In order to reproduce the impact of solar exposition in natural conditions, the free surface has been cyclically heated by an IR lamp (heat flux Φ=800 W/m^2) installed at a distance of 55 cm from the top of the sample (Figure 5.3).

The four sides of the block were insulated by 10 cm of polystyrene to minimize lateral heat transfer during freezing and thawing: hence the specimen could only freeze downward from the chilled air in the cold room and upward from the simulated permafrost.
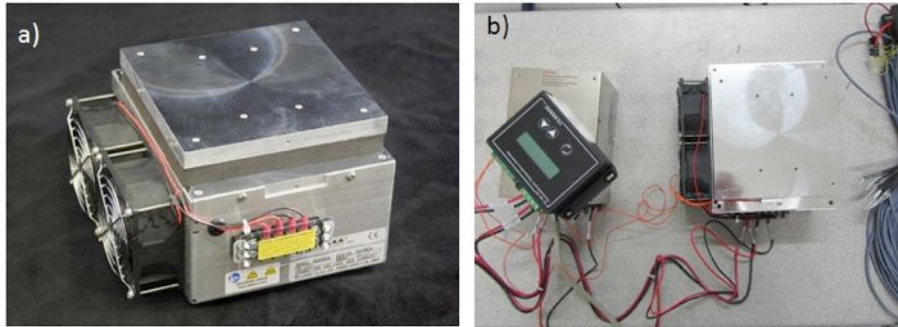
Figure 5.2: The upward freezing system: a) cooling plate (photo by TETech); b) thermoelectric temperature controller.
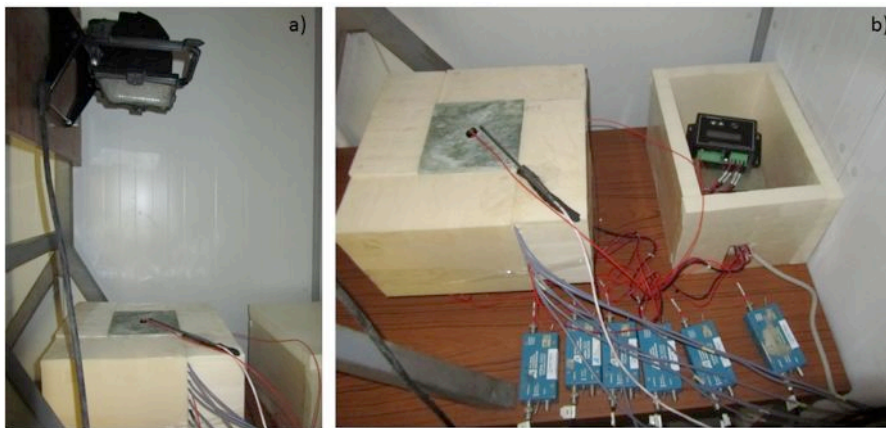
Figure 5.3: The instrumentated sample: a) under the IR lamp; b) conneted to the thermoelectric temperature controller.

5.3.1 Thermosensors

The temperature distribution has been monitored with a set of thermosensors that were platinum resistance thermometers Pt100 (TC Direct s.r.l. product). The characteristics of the Pt100 elements used and other technical specifications are given in Annex A.

The Pt100 sensors (Figure 5.4a)) described above have been used to measure
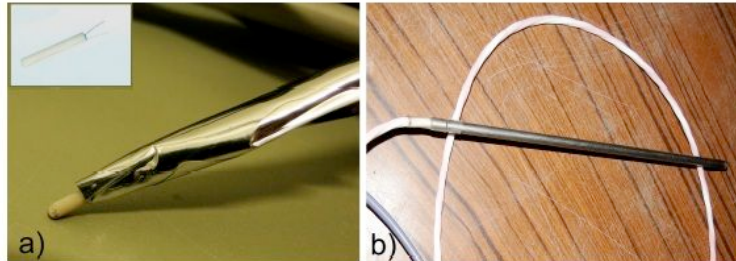
Figure 5.4: Sensors used for the temperature monitoring; a) Pt100 element used to measure the superficial and in depth temperatures; b) sensor used to measure the temperature of the lower face.

the temperature gradient through the thickness of the sample and the temperature trend on the upper surface. Eight sensors have been located adjacently to a vertical face (surface 2) of the specimen at different depths: 1.5, 3, 4.5, 6, 8, 10, 12, 14 cm (Figure 5.5); one sensor were placed on the upper surface (surface 1) of the specimen.

All the resistors were connected with shielded three-wire conductors the acquisition system, made of an acquisition board (PC10 - AOIP product), which allows measurement, monitoring and storage of digital and analogue signals issued from electrical sensors.

The configuration of the acquisition board and the data logging have been performed with LTC10 software, which allows the monitoring and the supervision of parameters such as temperatures thanks to an automated management of the memory. Temperature measurements were every 5 seconds. The general characteristics of the acquisition board are stored in Table B.1.
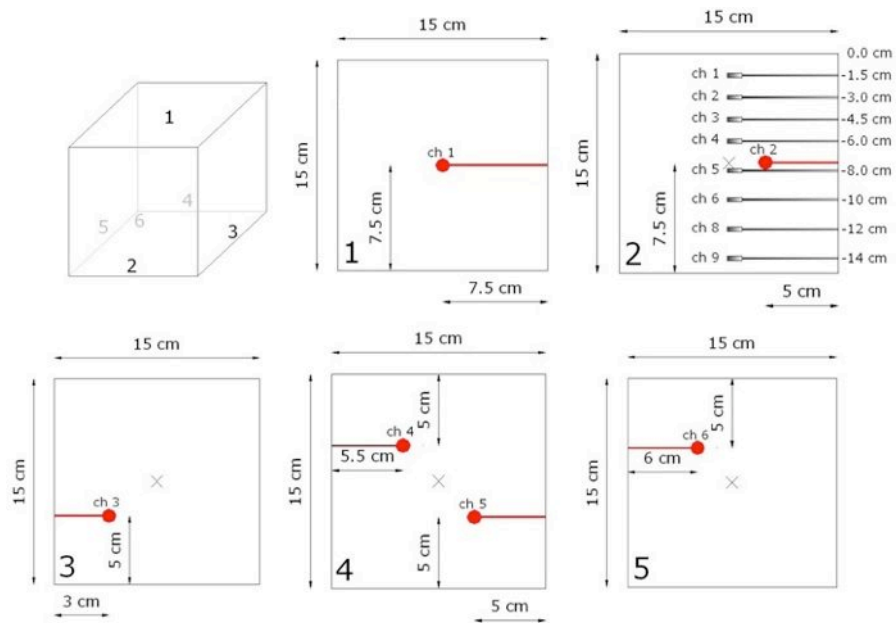
Figure 5.5: Schematic disposition of the sensors on the surfaces of the specimen: thermosensors in grey, acoustic emission sensor in red.
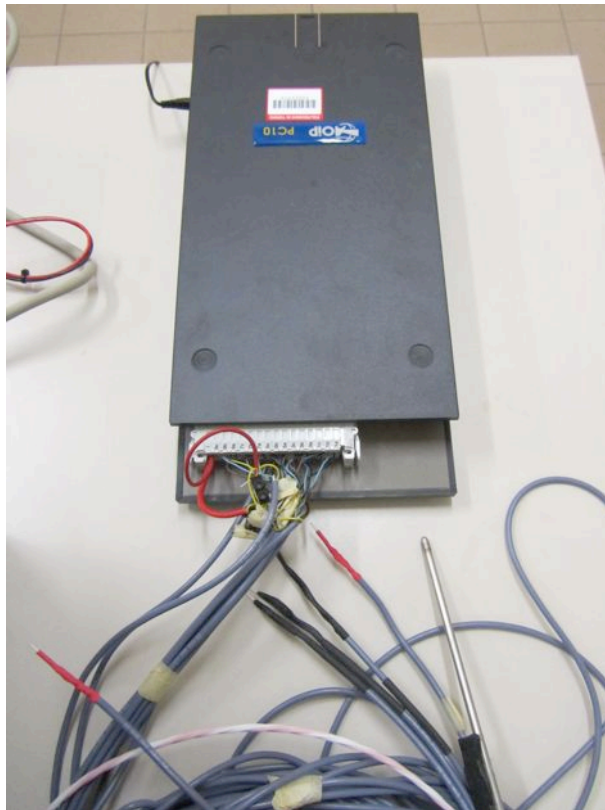
Figure 5.6: Acquisition board and thermosensors used in the laboratory test.

5.3.2   Acoustic emission sensors

A first attempt was made to evaluate the possibility of detect the damage process through the monitoring of the acoustic emission activity (AE). The transducers placed on each face of the sample are Physical Acoustic sensors, model NANO30 (FN 54-61), produced by Mistras Corporation, each one given with its calibration certificate (calibration methodology based on ASTM standard E976 "Guide for determining the Reproducibility of Acoustic Emission Sensor Response"). These sensors can be used in any application requiring a small, mid-band frequency response; they have a resonant response at 300 kHz and a good frequency response over the range of 125-750 kHz. Their size makes the sensors ideal candidates for applications where small size is important, feature that in this case has been extremely functional. The Nano-30 miniature AE sensors feature a small, 1 meter, integral coax cable, which exits from the side of the sensor with a BNC connector on the end. The AE sensor characteristics are reported in Annex D while in Annex G the calibration certificates of the used sensors are reproduced.

On each surface of the specimen were placed sensors of acoustic emissions to detect and localize the occurrence of microcracks propagation (Figure 5.5).

An effective acoustic coupling between the sensor face and the structure is an essential requirement: first it has been necessary to make sure that the sensor surface was smooth and clean, allowing for maximum couplant adhesion. The couplant should fill gaps caused by surface roughness and eliminate air gaps to ensure good acoustic transmission. Moreover the sensor should be held firmly to the testing surface during all the testing time. During the laboratory test the sensor has been fixed to the sample surface through a thin layer of glue which served as a couplant and held the sensor stable during the tests.

Each AE sensor has been connected to a 1220A preamplifier, made by the Physical Acoustic Corporation. The 1220A type is powered by +28 volts and uses the single BNC for both power and signal; it features single and differential input, switchable 10/40 dB gain and replaceable bandpass with values from 10 kHz to 1.5 MHz. In Figure 5.7a) it is possible to see an AE sensor connected to a preamplifier. The acquisition of the AE signals was made by an Advantech PC visible in Figure 5.7b).

84
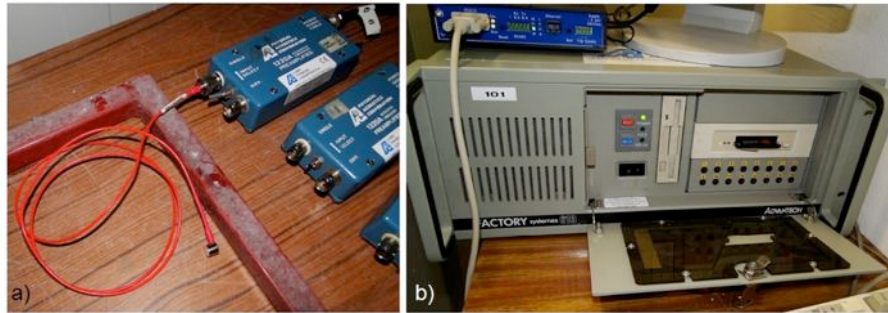
Figure 5.7: a) AE sensor connected to the preamplifier; b) Advantech PC used for the acquisition of the AE activity.

5.4 Freezing preliminary test

During the first freezing cycle, the saturated sample has been placed in the cold room which was initially at 18°C. Then the cold room temperature has been set at -15°C and the sample has been frozen until it has reached a uniform temperature in thermal equilibrium with the room.

5.4.1 Temperature analyses

Studying the temperature trend during freezing processes, it is possible to notice how the transient thermal field can be influenced by latent heat effects, even below 0°C. The fraction of liquid water as a function of temperature depends on the shape and diameter distribution of the pore space (rock properties) and the solute content of the pore water and shows a hysteresis between freezing and thawing. During freezing, a substantial fraction of pore water remains liquid even at temperatures below 0°C and large amount of energy is involved in the formation of hydrogen bonds in the crystal of ice while the freezing process continues. When the temperature inside the rock sample reaches -10°C, the crystallization process ends as well as the consumption of latent heat: in the graph in Figure 5.8 the abrupt change of slope of the curves that describe the evolution of temperatures in the specimen can be recognized.
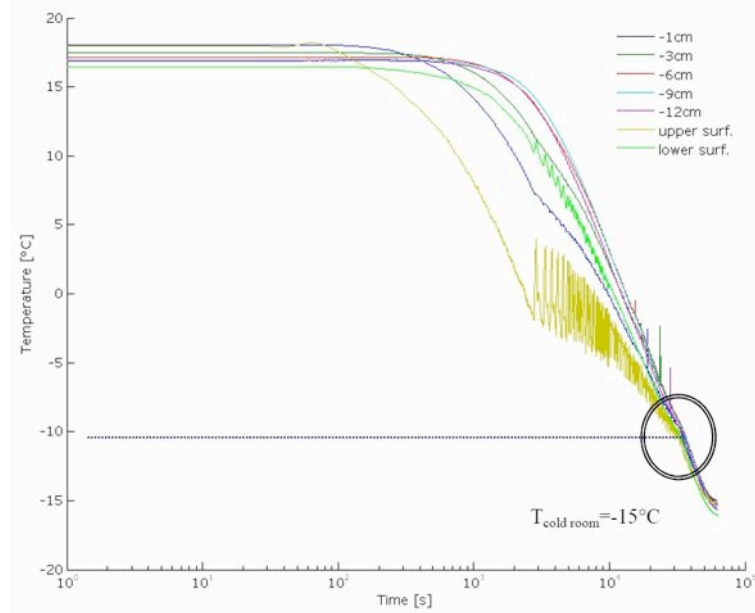
Figure 5.8: Cycle 1: freezing

5.5 Thermal cycles

The sample has been initially cold by chilled air in the cold room, until the entire block has reached 5°C; then the basal cooling plate was switched on and the sample started to freeze upward.

The freezing process followed three steps: the cooling plate was set initially at -10°C and this temperature has been kept fixed till the sample reached the thermal equilibrium; then the cooling plate temperature was lowered to -12°C; finally the air temperature of the cold room was set equal to -10°C and the specimen started to freeze from the surface downwards to simulate permafrost aggregation when bedrock is exposed to cold air. The entire period of freezing lasted seven days (Figure 5.9).

Three thaw-freeze cycles have been then carried out: the upper surface of the sample has been heated turning on the IR lamp, while the lower surface has been maintained at subzero temperatures, thanks to the cooling plate. During warm periods the upper half of the specimen thawed from the surface
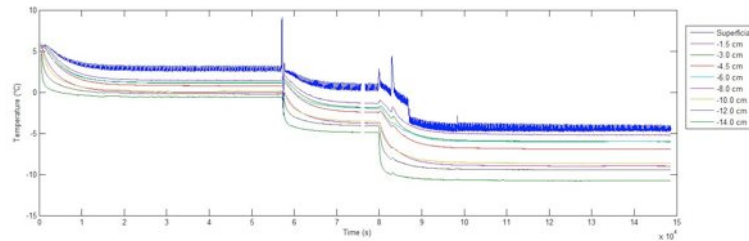
Figure 5.9: Three freezing steps

downward, simulating summer thaw of the active layer. The heating lasted till the the depth of maximum downward thaw (simulated permafrost table) was reached, so the "isothermal-zero" position has been carefully controlled and kept relatively constant.

Turning off the IR lamp, the upper half of the block froze both from the surface downwards and from the permafrost table upwards, simulating two-sided freezing of the active layer at autumn freeze-back.

During each thaw cycle water was supplied on the sample surface by the melting of superficial ice.

5.5.1   Temperature analysis

The freezing process of the sample consisted of several steps, as explained in the previous paragraph (5.5). At the beginning of the freezing period the temperature gradient in the gneiss was negative (downward heat flow), and at the end, positive (upward heat flow): during this phase the sample reached thermal equilibrium between the temperature of the cold room, set at 5°C, and the temperature of the cooling plate at-12°C.

At the beginning of the thaw period, the temperature gradient quickly changed from positive to negative. The first warm period lasted 16 hours: the temperature in the upper half of the block rose above 0°C (active layer), while the lower half remained subzero (permafrost). The superficial temperature was 9°C and the temperature at 14 cm depth was -9°C: this means that, thanks to the cooling plate, it was possible to obtain a temperature distribution that ensured a difference of about 21°C between the upper and lower surface of the sample.

Figure 5.10 shows the trend of temperature at different depths in the specimen: the sample reached the thermal equilibrium and the thermal

87

gradient was linear. In the upper graph, the dotted line identifies the position of the "0°C isotherm", which is located approximately 7.5 cm deep in the sample.

The other warm periods lasted 3 hours: in fact it can be noticed from the chart below in Figure 5.10, that the thermal equilibrium was not reached. The superficial temperature was 6°C and the temperature at 14 cm depth was -10°C: therefore the "0°C isotherm" depth was not deep as in the previous case and the specimen was thawed only in the first 4.5 cm from the surface.
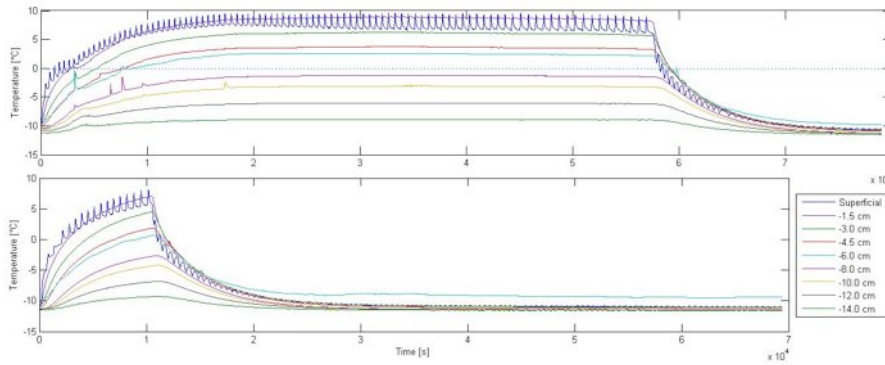
Figure 5.10: Comparison between two freeze-thaw cycles: in the upper graph the heating phase lasted 16 hours and the sample reached the thermal equilibrium. The dotted line indicates the position of the "0°C isotherm", about 7.5 cm deep.

The lower graph shows instead a second cycle of freezing and thawing, during which the warm period lasted only 3 hours and the sample did not have enough time to reach the thermal equilibrium.

During the cold period (21 hours), the sensor at 6 cm depth (cyan) had a problem, since recorded the temperatures much higher than those of the entire sample.

5.5.2   AE activity

The study of the AE is very sensitive, since many factors can interfere with monitoring. The first difficulty was to choose the right threshold that was able to minimize the noise of the apparatus and of the surrounding equipment, but

that was also able to record the events produced by the microcracks propagation. After several attempts, the trigger was set at 38 dB.

Some investigations have been carried out in the cold room, since the experimental activity is still at the beginning and during the tests and constant adjustments were needed: thus, the recording has been manually started and stopped at the same time when the temperature recording started or stopped too. The manual starting required the synchronization of the two operators who manually started the softwares for the AE and temperature recordings on two different PC.

The results of the AE activity monitored during the cycles described above, has been analyzed observing the cumulate of events recorded during each cycle and comparing it with the temperature trends.

In Figure 5.11 the graphs of the cumulate of the number of events recorded during the first freezing cycle is reported and compared with the temperature trend. From the beginning of the cycle till the point 1 (17/11/2010 - 2:10 am) it is possible to notice a uniform increasing of AE activity.

In correspondence of -10°C, where it is possible to hypothesize the end of the crystallization, as described in the previous paragraph, it is possible to notice an increment of the AE activity followed by a more stable interval till the end of the cycle. It can be hypothesized that most of the activity and, as a consequence, most of the microcrack propagation, occurs during the crystallization phase. This can be due to the increase of volume when the water filling the pore and the existing microcracks, freezes.

The same trend can be seen in the Figure 5.12, when the cumulate of the number of AE events increases in correspondence to a sudden lowering of the temperatures at the second freezing step: this phase is followed by a more stable interval till the third freezing step, when a new increase in the number of events has been recorded, though less significant, due to a new temperature lowering. Again a stable phase follows.

Figure 5.13 shows the graph of the cumulate of the number of events recorded during the first thaw-freeze cycle and the temperature trend: thawing period lasted 16 hours.

In correspondence of -10°C, where the end of the crystallization is hypothesized, as described in the previously, it is possible to notice again an increment of the AE activity followed by a more stable interval till the end of the cycle.

An interesting increase in the number of events can be noticed observing the graphs in Figure 5.14. This phenomenon has been reported after 15 hours of freezing and it indicates that all the microfractures propagated within the
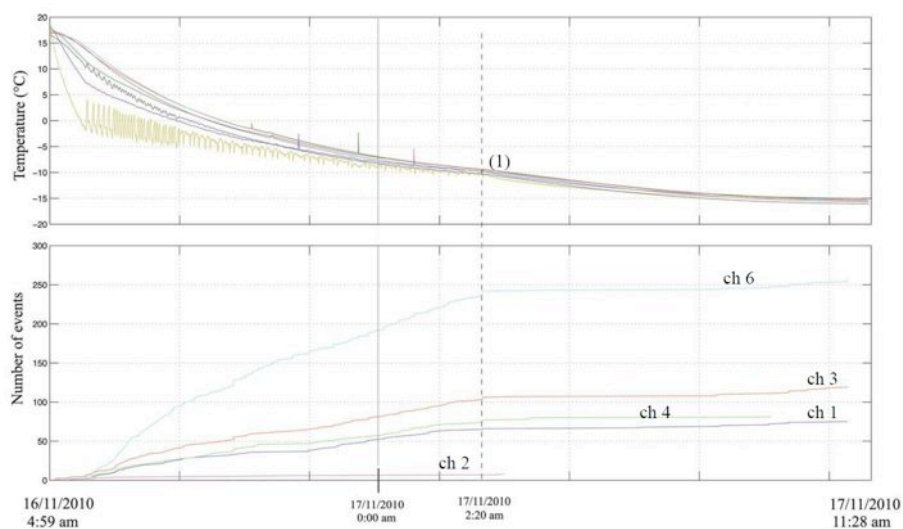
Figure 5.11: Comparison between the AE activity and temperature trend recorded during the first freezing cycle.

already frozen portion of the rock, rather than being associated with the freezing front.

As soon as the lamp was turned off (which corresponded to a temperatures rapid drop and high gradient), a corresponding increase of AE activity wasn't recorded, but the increase in the number of acoustic emissions occurred by the end of the freezing cycle: this could mean that the events recorded were not due to the thermal strain (thermal contraction cracking) but probably to the frost-induced microfracture propagation. The frost induced microfracture propagation does not require falling temperatures, as all the AE activity reported here accurred while temperatures and temperature gradients were held fixed.

The considerable microfracture activity monitored at steady subfreezing temperatures is a manifestation of microfractures being progressively wedged open in domains within the sample that are cold enough to permit sufficient ice-generated pressure to cause progressive microcrack growth: from literature the most rapid crack growth was predicted to occur in the ranges between -4°C to -15°C [92] (Matsuoka, 2001).
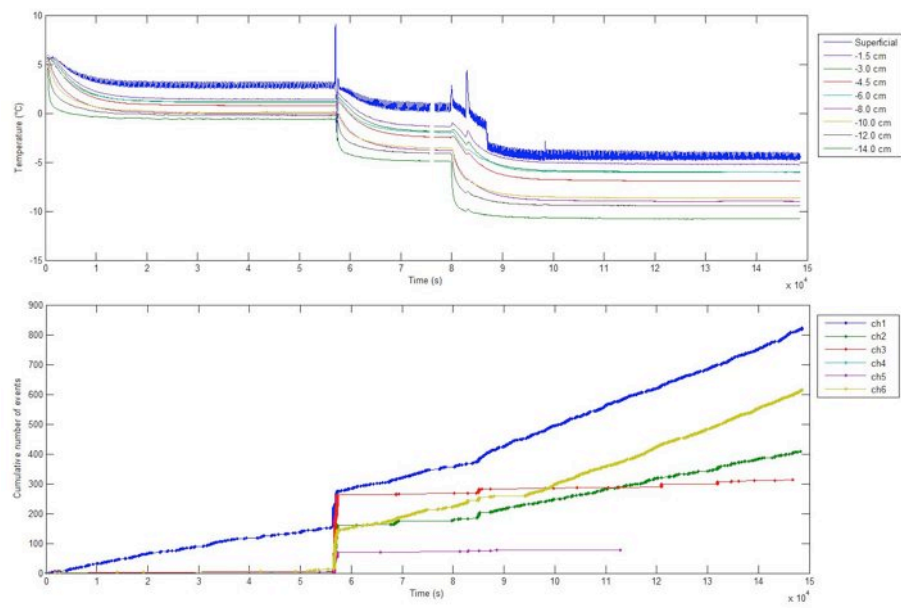
Figure 5.12: Comparison between the AE activity and temperature trend recorded during the freezing steps.
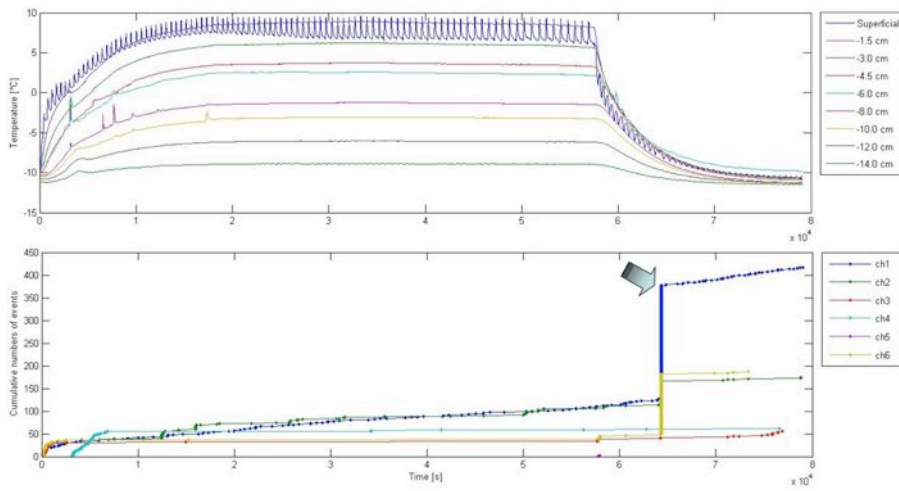
Figure 5.13: Temperature distribution during the first step of the freezing process.
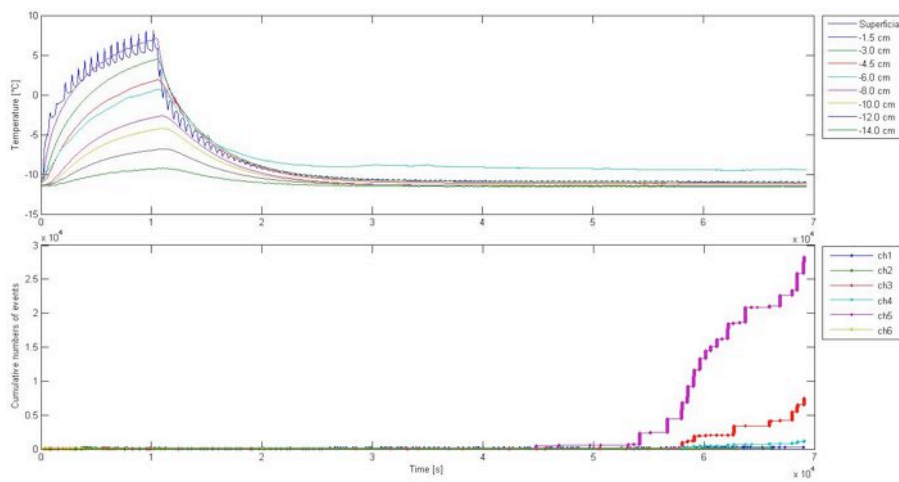
Figure 5.14: Temperature distribution during the first step of the freezing process.

92

5.6   Final considerations

Since the tests described in the present chapter had the aim of testing the methodology and identifying the correct procedure for the following laboratory activities, the first results are not significant for understanding the material behavior.

Unlike the stringent conditions needed for volumetric expansion to fracture rocks, the conditions needed for ice segregation, are slow rates of freezing or sustained subzero temperatures in saturated, fine-grained rock ([93] Matsuoka & Murton, 2008); laboratory experiments (see 5.1) have demonstrated that ice segregation can fracture rock blocks under constant temperatures and temperature gradients; finally, simulations of unidirectional freezing regimes (see Chapter 4) resulted in fracture of porous rock by ice-lens growth in near-surface permafrost ([100] Murton et al., 2001). Starting from these considerations and from the experience acquired during the laboratory pilot study described above, some decisions have been taken designing the experimental procedure and guidelines for an optimal test design, can be derived:

* slow and prolonged freezing so as to ensure thermal equilibrium and constant active layer deepening, in order to permit the migration of pore water;

* as the presence of a nearby moisture source plays a fundamental role in ice segregation ([92] Matsuoka, 2001), a controlled supply of water have been programmed so that a continuous downward water percolation could be available, ensuring a long-term, slow freezing test under an open-system condition;

* as the effective microgelivation requires an initial saturation degree of 0.8, the saturation procedure have been improved and designed ad hoc: the initial degree of saturation is important because it allows the pore water volume expansion during the first cycle of freezing and then the water could be drawn from the saturated zones to the frozen rock ([96] Mellor, 1970; [89] Matsuoka, 1990; [119] Prick, 1997). Saturation has been maintained, by coating the side surfaces of the specimen with silicone;

* as porosity governs volumetric expansion by delimiting the capacity of ice volume and permeability controls water migration, these rock properties could affect ice formation and the expansive force ([161] Williams & Smith,

93

1989). For this reason, artificially microcracked specimens of Arolla gneiss have been used;

* the technical problems of instrumentation should be solved and all the thermal sensors should be carefully calibrated;

* coupling between the insulation, sample surfaces and AE/thermal sensors, has been improved, building eight special brass housings for the AE sensors, a rigid plexiglass cladding around the rock block, with appropriate holes for the sensors, and studying thoroughly different types of insulation;

* 8 amplifiers have been designed and manufactured specifically for this type of test.

All the details related with the experimental procedure design and set up will be explained in Chapter 8.

Chapter 6

Thermal treatment and mechanical behavior of Arolla gneiss

Since the rock samples collected from Carrel Hut area, are characterized by porosity values higher than the Arolla gneiss (see Table 5.2), strong mylonitic deformation and heterogeneous grain, the specimens of Arolla gneiss have been subjected to thermal cycles that modified the specimen microstructure, in order to be comparable with the material which characterizes the Matterhorn at 3835 m a.s.l.

Temperature variations induce micro-cracks in rock because of the heterogeneity or phase transition of mineralogical components, which have different coefficients of thermal expansion that lead to onset of intergranular compressive and tensile forces starting from a threshold temperature. Depending on temperature intensity, thermal cracking can occur either between adjacent crystalline grains (intergranular cracks) or within grains (intragranular cracks) such as the case of α/β phase transition in quartz.

6.1 Thermal micro-cracking

Experimental works ([126] Rotonda, 1991) have confirmed that the damage induced by heating determines variations of rock properties that are closely

connected to the fracturing degree of the material.

The formation of thermally-induced microcracks in rocks subjected to slow ($\leq 2°C/min$), uniform temperature changes, gives rise intergranular thermal stresses independently of the existence of a temperature gradient. These stresses induce the formation of microcracks preferentially along grain boundaries and secondarily as intragranular cracks.

The thermal micro-cracking is initiated by a critical temperature that depends on several parameters: in the case of granite, for example, corresponds to a range of temperature between 75°C and 100°C ([126] Rotonda, 1991).

Due to the anisotropic single-crystal thermal expansion and to the mismatch of thermal expansions of neighboring mineral grains characterized by the different thermal expansion coefficient, stresses are generated along the grain boundaries, which lead to a granular decohesion of the material with time (Weiss et al., 2003).

Material parameters supposed to promote or control thermal degradation, are grain size, grain shape, grain-to-grain misorientation and bulk lattice preferred orientation, as well as the single-crystal properties of the rock forming minerals (Weiss et al., 2003).

In rocks containing quartz, the inhomogeneity of the thermal expansion coefficient of the different minerals plays a dominant role in thermal-crack development at temperatures below the $\alpha - \beta$ transition of quartz (573°C), due to the differential expansion between neighboring quartz and other mineral grains ([126] Rotonda, 1991). Thermal expansions of some natural minerals are listed in Table 6.1.

Table 6.1: Volumetric thermal expansions (%) of some natural minerals ([141] Skinner, 1966).

	200°C	600°C
orthoclase feldspar	0.155	1.185
sillimanite	0.215	0.931
plagioclase feldspar (56-44)	0.240	0.950
calcite	0.285	1.395
pyroxene (augite)	0.350	1.370
garnet (spessartite)	0.396	1.528
microcline feldspar	0.398	1.029
hornblende	0.420	1.580
quartz	0.780	4.520

The following will describe the laboratory tests carried out on Arolla gneiss fresh and micro-cracked samples. Uniaxial compressive and indirect tensile stress tests have been performed in order to characterize the mechanical behavior of the material (section 6.2). Open porosity (section 6.3.2) and total porosity (6.3.3) have been determined, after each thermal cycle. Ultrasonic wave velocity has been measured on the specimen in natural condition and after each thermal treatment in dry conditions (see section 6.3.3): then the sample has been saturated, and P-wave velocity measurements have been carried out at T=20°C and T=-12°C, as explained in section 6.4.1 and section 6.4.1, respectively.

6.2   Mechanical tests

The mechanical behavior of thermally-cracked samples has been mostly studied by destructive mechanical tests. The compressive or tensile tests provide direct information about evolution of elastic modulus, compressive or tensile strength versus temperature.

The physical and mechanical characteristics of the rock have been determined according to the Standards of the American Society for Testing and Materials (ASTM).

Natural and treated samples of Arolla gneiss, obtained from cores extracted from a rock block collected in Valpelline (Valle d'Aosta), have been tested in the laboratory to identify their mechanical features.

Six cylindrical specimens have been prepared from the rock block by drill coring into two orthogonal directions; across and along the foliation plane. They have been cut at the two ends, which were then polished into smoothed surfaces. The final dimension of each specimen was about 5 cm in diameter and 12 cm long.

To investigate the influence of microcracking conditions on the mechanical behavior of the Arolla gneiss, two cylindrical samples have been slowly heated in a furnace at ambient pressure to 420°C with a heating rate of 0.5°C/min at the Department of Analytical Chemistry, Universitá degli Studi di Torino, in cooperation with Professor Maurino and Dottor Sordello. The low rate of heating has been used to ensure that cracking events result only from the temperature effect and not due to thermal gradients across the sample. The maximum temperature has been maintained for 18 hours. The specimens have then been cooled at an inverse gradient of 0.1°C/min to room temperature ([28] Chaki et al., 2008).

On these six specimens, two thermal-cracked and four in natural conditions, tests have been carried out to determine strength and deformability in uniaxial conditions, according to the designation ASTM D 3148-93.

The tests have been carried out at MASTRLAB - Laboratorio Sperimentale Materiali e Strutture, Politecnico di Torino.

In Table 6.2 specimens diameter and length, direction of loading (parallel or orthogonal to the foliation plane), deformation rate, maximum applied load and compressive strength, are reported.

The axial Young's Modulus, E, has been calculated as the tangent modulus at a stress level equal to 50% of the maximum strength. The Poisson's ratio has been determined as the ratio between the slope of the axial and the radial strain curves, at the same stress level.

Table 6.2: Results obtained from uniaxial compression tests on cylindrical specimens of Arolla gneiss: CA_nc, CB_nc, CE_nc and CF_nc were samples in natural condition, CD_m and CE_m were thermally microc

	CA_nc	CB_nc	CC_m	CD_m	CE_nc	CF_nc
Height H [mm]	126.80	127.52	119.32	118.81	147.51	147.63
Diameter D [mm]	50.19	50.19	50.24	50.29	49.02	48.90
Weight W [g]	701.50	700.30	653.30	652.10	753.25	741.40
Schistosity	$\perp$	$\perp$	$//$	$\perp$	$//$	$//$
Deformation rate [mm/min]	0.025	0.025	0.015	0.005	0.025	0.025
Maximum applied load P [kN]	219.80	228.48	188.4	233.90	252.14	212.5
Compressive strength C_0 [MPa]	111.10	115.48	95.04	117.75	133.60	113.15
Young modulus $E_t [GPa]$	101.26	102.10	95.34	128.12	146.55	117.60
Poisson ratio ν [-]	0.25	0.22	0.01	0.04	0.25	0.21

Observing the graph in Figure 6.1, where the stress-strain curves obtained for the six samples subjected to uniaxial compression are reported, it is possible to notice that compressive strength is poorly affected by micro-cracking after only one cycle of heating, whereas a decrease in Young's modulus is more noticeable. As a matter of fact, static deformability (and dynamic properties) are markedly reduced by even only mild microcracking, whereas strength is less influenced ([126] Rotonda, 1991). Moreover, the stress-strain curves relating to micro-cracked specimens, have a non-linear trend and a reverse concavity for low load levels.

It has been also noted that the lateral deformation in uniaxial compression tests

on thermal microcracked samples is lower than the one of intact material, and even for high microcracking temperatures, the Poisson's ratio can be negative ([126] Rotonda, 1991). This is in agreement with the extremely low values of Poisson's ratio obtained for the cylindrical micro-cracked samples (CC_M and CD_M).

For completeness, brazilian, or indirect tensile, tests have been performed on cylindrical disks specimens to determine the indirect tensile strength of fresh Arolla gneiss. The tests have been carried out at DIPLAB - DIsaster Planning LABoratory, Politecnico di Torino, following the designation ASTM D 3967-95a.

In Table 6.3 specimens diameter and length, direction of loading (parallel or orthogonal to the foliation plane), deformation rate, maximum applied load and splitting tensile strength are reported.

Table 6.3: Results obtained from splitting tensile strength tests on cylindrical disks specimens of Arolla gneiss

	BR_{14}	BR_{15}	BR_{16}	BR_{17}
Thickness L [mm]	30.46	31.41	30.01	30.22
Diameter D [mm]	48.96	48.95	49.00	49.98
Weight W [g]	156.12	159.50	155.91	155.20
Schistosity	//	$\perp$	//	$\perp$
Deformation rate [mm/min]	0.02	0.05	0.05	0.05
Maximum applied load P [kN]	4.56	16.03	8.055	17.45
Splitting tensile strength σ_t [MPa]	1.95	6.64	3.49	7.36

6.3   Non-destructive tests

Non-destructive tests, such as open porosity and ultrasonic wave velocity, have been performed on 50mm and 150mm-cubic shape specimens respectively.
All the gneiss specimens have been heated to induce micro-cracking.

6.3.1   Thermal treatment

The samples have been subjected to two different thermal cycles, at the Department of Analytical Chemistry (Universitá degli Studi di Torino), in cooperation with Professor Maurino and Dottor Sordello.

99
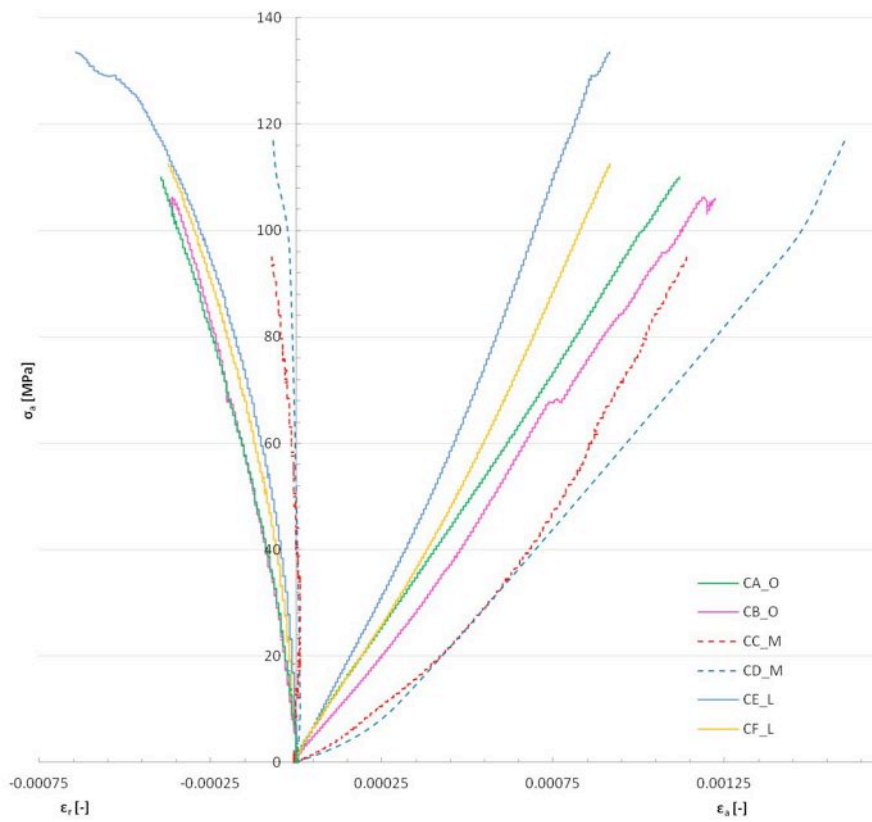
Figure 6.1: Stress-strain curves for the axial and the radial direction obtained from the uniaxial compression tests.

During the first thermal treatment, the specimens have been heated to 420°C with a heating rate of 0.5°C/min; the maximum temperature has been maintained for 18 hours. The specimens have since been cooled at an inverse gradient of 0.1°C/min.

During the second thermal treatment, the samples have been subjected first to a thermal shock and subsequently to a new thermal cycle. In particular, the samples have been placed in an oven at temperature of 250°C for 24 hours, and then suddenly cooled in cold water.

Finally the specimens have been slowly heated in a furnace at ambient pressure to 420°C with a heating rate of 0.5°C/min. The low rate of heating has been used to ensure that cracking events result only from the temperature effect and note due to thermal gradients across the sample. The maximum temperature has been maintained for 5 days. The specimens have then been cooled placing them directly to the room temperature.

6.3.2   Open porosity

Porosity is one of the basic physical properties of rocks. It can be classified into different types such as absolute or total porosity, open porosity, and effective or connected porosity. The total porosity is simply the fractional volume of all void space inside a porous material. While the open porosity considers only the proportion of voids that are communicated with the outside of the sample. The effective or connected porosity is the volume fraction of pore spaces that are fully interconnected between two opposite end-faces and allowing the fluid flow through the material.

The open porosity of 50mm-cubic shape specimens, has been measured in natural conditions and after each thermal treatment according to EN 1936 (it is classically inferred from successive weight measurements of dry, water saturated and immersed samples). The tests have been conducted at the Department of Environment, Land and Infrastructure Engineering (Politecnico di Torino), thanks to Prof. Marini and Dr. Bellopede.

The water content of the saturated samples has been determined, and from this value, the hydraulically connected porosity has been estimated, which is likely related to the thermal micro-cracking.

For the fresh gneiss, the open porosity mean value is 1.03%. The evolution of this rock property with thermal treatment is presented in Table 6.4.

A low increase in porosity after the first thermal cycle has been observed. This implies that the samples present only minor structural modifications, primarily due to the opening of pre-existing microcracks and/or to the nucleation of a

new cracks. The most important change has appeared after the second thermal treatment and has induced a significant increase of the open porosity. This is explained by connection of the discontinuities networks created during the previous phase, and by an increase in the number of the open cracks.

In the following paragraph the increase of the total porosity as a function of thermal treatment will be presented, obtained by Wyllie time-average equation([162] Wyllie, 1958), that relates sonic velocities with the porosity of a rock (section 6.3.3). These values have been calculated for the 150mm-cubic shape specimen, since its dimensions have not allowed the measures of open porosity because of the sensitivity of the instrumentation.

Table 6.4: Open porosity and apparent density of Arolla gneiss in natural condition, after the first thermal cycle and after the second thermal cycle

	Natural conditions	I thermal cycle	II thermal cycle
Open porosity P_0 [%]	1.03	2.25	3.57
Apparent density ρ_b [Kg/m^3]	2774.46	2760.40	2759.38

6.3.3   Ultrasonic measurements

To investigate the rock dynamic characteristics and the changes induced by the thermal treatment, the ultrasonic wave velocity has been determined by measuring the travel time of a pulse along the axis of 150mm-cubic shape specimen.

Changes in amplitude and travel time (attenuation and slowness) reveal changes in the physical properties of the material: the measurements have been performed on the sample in natural conditions and after each thermal cycle.

The tests have been conducted at the Department of Environment, Land and Infrastructure Engineering (Politecnico di Torino).

The ultrasonic equipment used for data acquisition is a PUNDIT (Portable Ultrasonic Nondestructive Digital Indicating Tester): the device is equipped with two piezoelectric transducers (diameter 50mm), transmitter and receiver, connected to the PUNDIT with shielded coaxial cables and BNC connectors. These crystals were fabricated to convert electric signals into mechanical vibrations, in a compression (P) and a shear (S) mode, or vice versa.
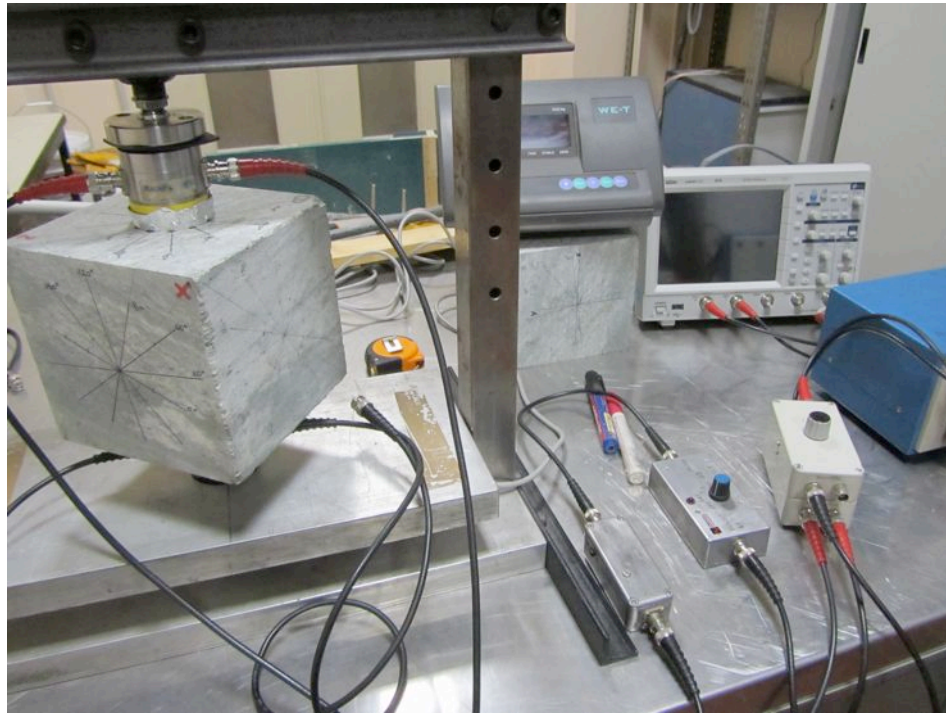
Figure 6.2: A picture of the ultrasonic survey apparatus.

The specimen has been placed between the two piezoelectric transducers as shown in Figure 6.2. Furthermore, for each measurement taken, a pressure of 0.4 MPa has been guaranteed, placing the sample in a load cell. To avoid background noise in the received signal, two sheets of rubber have been placed between the transducers and the plates of the press load.

The PUNDIT has been connected to an Oscilloscope LeCroy WaveJet 314, in order to visualize the received signal.

The pulse generator sends an electric pulse at a desired interval to both the transmitter on one end of the specimen and to the oscilloscope. This signal simultaneously triggers the recording and excites the transmitter. The vibration propagates through the sample and arrives at the other end, where it is reconverted into an electric signal by the receiving crystal. The signal is amplified through two pulser-amplifier units (7 and 10 dB). The oscilloscope

then receives two signals: one is trigger, the other is through the sample, and displays them both. The traces have been recorded on a USB flash drive connected to the oscilloscope, in order to perform further signal processing and to obtain a more reliable first picking.

Before any measurement, the calculation of the transducers delay due to constructive reasons, has been carried out: an amount equal to $7.7 \cdot 10^{-6}$s (P-waves) and $11.6 \cdot 10^{-6}$s (S-waves) have been then subtracted from all the time readings.

Two components of elastic wave velocity, compression and shear waves, were measured along x, y, and z axis of the specimen: z-axis is normal to the foliation plane. On each face, the measurements related with shear waves, were carried out by rotating the transducers of an angle ω equal to 0, 30, 60, 90, 120 and 150°, and others have been obtained by symmetry: ω equal to 0° corresponds to the direction parallel to the schistosity plane.

The ultrasonic velocities are calculated from the travel time of the pulse and relative sensor positions i.e. path length: P- and S-wave arrival times were manually picked on the waveforms obtained from a Matlab code.

The procedure explained above was repeated on the same sample after each thermal cycle.

The seismic velocity is a very sensitive indicator of microcracking conditions ([126] Rotonda, 1991): the effect of temperature is mainly due to mechanisms of induced microcracking rather than a direct influence on the intrinsic physical characteristics of minerals, as is evident from Figure 6.3. The graphs show the variation of the longitudinal and transverse velocities with the increase of open porosity due to thermal microcracking.

As expected, there is a negative correlation between velocity and the damage induced by the heat treatment: these results are in agreement with the porosity evolutions against thermal cycles, as this phenomenon characterizes the interaction between waves of high frequencies and heterogeneities, i.e. the micro-cracks (see Table 6.5).

In principle, the material exhibits a global orthotropic structure that, in first approximation, can be considered transversely isotropic.

Carefully observing the sample, however, three main planes have been identified in the block, whose intersections have then been considered the reference axis during the experiment.

Anisotropy seems to have a significant effect on data measured on the sample in natural condition, as it is shown in Figure 6.4 and 6.5.

Since from the first heat cycle it can be noted how the marked differences of S-wave velocity measured with respect to the axis x, y, z are reduced. After

the second thermal cycle, the S-wave velocity values are nearly equivalent in three directions: it would seem an isotropic S-wave velocity.

This phenomenon can be explained by the fact that the overlapping mica flakes (preferential layers along which the S-wave velocity increases) have suffered a degradation after the thermal treatment and have been detached from the grains of feldspar: the initial anisotropy, determined by the schistosity planes coincident with the orientation of mica sheets, is then lost. Consequently the difference of the S-wave velocity values as a function of the angle of polarization has been also considerably reduced (Figure 6.4 and 6.5).

Table 6.5: P-wave velocity value variations induced by microcracking

	Natural conditions			I thermal cycle			II thermal cycle		
	x-axis	y-axis	z-axis	x-axis	y-axis	z-axis	x-axis	y-axis	z-axis
mean [m/s]	4560	3106	2508	3389	2564	2100	1691	1465	1582
std [m/s]	400	248	64	149	10	71	172	73	129
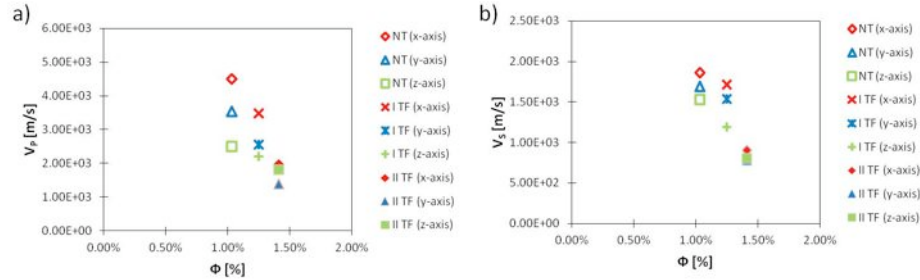
Figure 6.3: Variation of the longitudinal (a) and transverse (b) velocities with the increase of open porosity due to thermal microcracking.
(NT = No thermal treatment, I TF = First Thermal micro-fissuration cycle, II TF = Second Thermal micro- fissuration cycle and thermal shock).

The values obtained are in agreement with those reported in the literature (e.g [126] Rotonda, 1991). Figure 6.6 shows the elastic waves velocity variations as a function of the maximum temperature maintained during
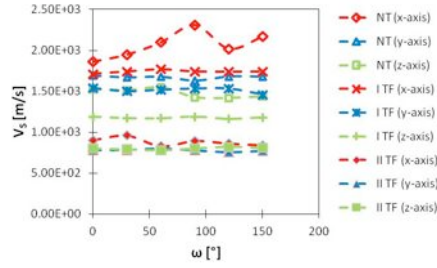
Figure 6.4: S-wave velocities depending on ω angle. (NT = No thermal treatment, I TF = First Thermal micro-fissuration cycle, II TF = Second Thermal micro- fissuration cycle and thermal shock).
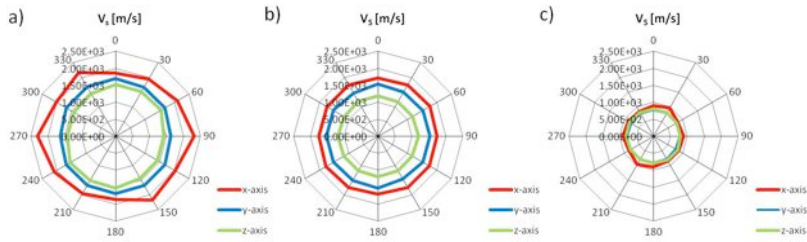
Figure 6.5: S-wave velocities depending on ω angle. (a) sample in natural condition; (b) sample after the first thermal cycle; (c) sample after the second thermal cycle.

thermal microcracking treatment. These changes, compared to those of the intact rock, are related to the aspect-ratio of the micro-cracks system: in fact, the thermal microcracking causes both the creation of new microfractures with low aspect ratio, and the extension or opening of pre-existing microcracks, with an increase in the aspect ratio ([126] Rotonda, 1991).
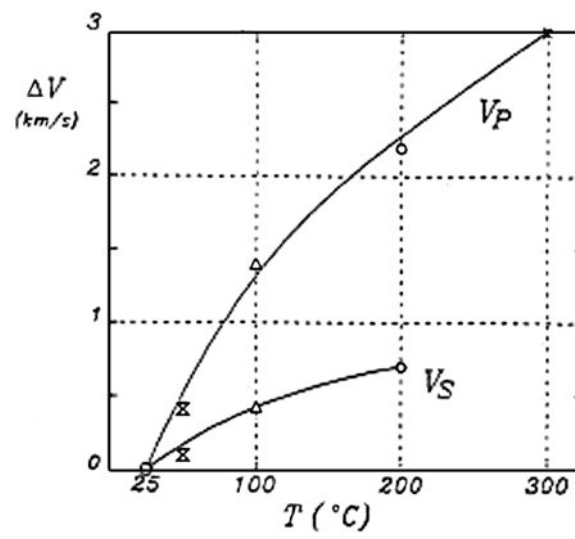
Figure 6.6: Elastic waves velocity variations as a function of the maximum temperature maintained during thermal microcracking treatment ([126] Rotonda, 1991).

107

Wyllie time-average equation

In order to estimate the total porosity of the 150mm-cubic shape sample in natural conditions and after each thermal cycle, the Wyllie equation has been used, obtaining a relationship between compressional velocity and porosity for the Arolla gneiss rock.

This time-average equation relates the wave's phase velocity v to porosity ϕ, fluid velocity v_f, and rock matrix velocity v_m ([162] Wyllie et al., 1958):

$$\frac{1}{v} = \frac{\phi}{v_f} + \frac{1 - \phi}{v_m} \qquad (6.1)$$

The interpretation of this expression is that the total transit time is the sum of the transit time in the mineral plus the transit time in the pore fluid.

Through this relationship, the total porosity has then been calculated by inserting the P-waves velocities derived from ultrasonic measurements, a fluid velocity $v_f = 340$m/s ([162] Wyllie et al., 1958) and a rock matrix velocity $v_m = 6080$m/s which is an average velocity for the material characterized by a mixed mineralogy.

The following Table 6.6 summarizes the mineralogical composition of Arolla gneiss and the corresponding velocities ([95] Mavko et al., 1998).

Table 6.6: Mineralogical composition of Arolla gneiss sample obtained by the analysis of thin sections.

Mineral	[%]	$V_P[m/s]$
quartz	40	6050
muscovite	20	6460
K-feldspar	20	4680
epidote	15	7430
plagioclase	4	6460
opaque	1	-

The use of the time average equation would require the following considerations:

- the rock is isotropic;

- the rock must be fluid saturated;

- the rock is at high effective pressure.

108

Despite the measurement conditions do not satisfy the above assumptions, the Wyllie time-average equation may be useful to obtain an indicative porosity variation value after each thermal cycle, which would otherwise be impossible to measure according to the standards, due to the block size. Total porosity values obtained are reported in Table 6.7: it can be seen how the total porosity variations agree with those of open porosity (see Table 6.4).

Table 6.7: Total porosity, obtained from the Wyllie time-average equation, of Arolla gneiss in natural condition, after the first thermal cycle and after the second thermal cycle

	Natural conditions	I thermal cycle	II thermal cycle
Total porosity P_0 [%]	5.40	8.03	18.55

6.4 Saturation procedure

In order to saturate the specimens, a combination of vacuum to remove air, and pressure to force water into the pores has been used. The procedure was carried out at the the Department of Analytical Chemistry (Universitá degli Studi di Torino), thanks to Prof. Maurino and Dr. Sordello, with an apparatus specifically constructed. The sample has been placed in a container of demineralized water inside a bell jar, and connected to a turbomolecular pump to obtain and maintain high vacuum. The pressure in the bell jar has been sufficiently low for the water to boil and the sample has remained in this conditions for 10 hours, and subsequently returned to atmospheric pressure

6.4.1 Saturated P-wave velocity of thermally microcracked sample

P-wave velocity measurement has been carried out on the sample completely saturated, using the PUNDIT and just one transducer (transmitter and receiver). Transducer have been pressed in the center of the upper sample surface and the pulse transit time was recorded along the z-axis (normal to the foliation plane). P-wave velocity value have been calculated by dividing the length of sample to the half pulse transit time.

The velocity obtained was about 4300 m/s.The comparison between P-wave velocity measured in the laboratory on the saturated-microcracked rock sample, and values obtained applying Gassmann's theory, shows that the petro-elastical model does not fit the data.

The unconformity between the measured data and the estimated data from the theories is due to the fact that Gassmann derived his equations for high-porosity unconsolidated sediments at low frequencies ([95] Mavko et al., 1998). The rocks tested in this study do not match the material specified by Gassmann's theory, since it is a thermally microcracked gneiss caracterized by low porosity and penny-shape cracks due to thermal treatment.

Some researchers have investigated the effect of water content on the ultrasonic velocities. Wyllie et al. ([162] Wyllie, 1958) investigated the variation of velocity in sandstone as a function of water content. They showed that there is a marked decrease in the P-wave velocity as the saturation is reduced from 100% to approximately 70%, between 70% and 10% the P-wave velocity is nearly constant and below 10% the velocity is changeable. Thill and Bur ([148] Thill & Bur, 1969) examined the influence of saturation on pulse velocity in granodiorite rock. They found that a remarkable velocity changes

can occur even in compact rock having only a minute amount of porosity. Wang et al. ([160] Wang et al., 1975) determined both compressional and shear wave velocities in Alpine gneiss along its principle fabric directions under dry and saturated conditions. The compressional wave velocities in all three directions increased remarkably as the sample was immersed in the water, whereas the shear wave velocities exhibited little change. The greatest change took place in the compressional waves in the direction perpendicular to the foliation of the rock.

Nur and Simmons ([110] Nur & Simmons, 1969) measured the compressional wave velocity in a sample of granite, initially saturated with water but allowed to dry in the atmosphere over a period of four days. Because of their low porosity, generally less than 1%, the velocities in granites were not expected to be influenced by saturation with water. Simmons and Nur found, however, that the differences in Vp of dry and saturated granite samples at low pressure may approach 50% ([110] Nur & Simmons, 1969). They indicated that a rapid change of velocity occurred in the first a few hours even though the porosity of the sample is only about 1%.

This work demonstrates the need to take into account that the shape of the pores in typical crystalline rocks plays an important role: increase in Vp due to saturation of pores occurs when the pores are in the form of cracks but not when they are in the form of round holes (spheres). Nur and Simmons ([110] Nur & Simmons, 1969) reported Walsh's expression derived for two phase systems, where one phase consisted of low aspect ratio elliptical holes: the inclusion is empty or contains a fluid ([159] Walsh, 1969). The shape of the inclusion or crack, assumed to be penny-like, is specified through a single parameter - the aspect ratio $\alpha = a/d$ where a is the width and d is the diameter of the crack. Walsh's expression for bulk and shear moduli when the inclusion fluid is air (viscosity is vanishingly small and compressibility almost infinite) are:

$$\frac{1}{K_{air}} = \frac{1}{K_0}\left(1 + m\frac{c}{\alpha}\right) \tag{6.2}$$

$$\frac{1}{\mu_{air}} = \frac{1}{\mu_0}\left(1 + n\frac{c}{\alpha}\right) \tag{6.3}$$

where K_0 and μ_0 are the bulk and shear moduli of the solid, c and α are respectively, porosity and aspect ratio of the inclusions (assumend to be penny shaped),

$$m = \frac{K_0\left(3K_0 + 4\mu_0\right)}{\pi\mu_0\left(3K_0 + \mu_0\right)} \tag{6.4}$$

111

$$n = \frac{4}{15\pi} \left[\frac{2\left(3K_0 + 4\mu_0\right)}{\left(3K_0 + 2\mu_0\right)} + \frac{\left(3K_0 + 4\mu_0\right)}{\left(3K_0 + \mu_0\right)} \right] \tag{6.5}$$

The corresponding expressions for the same material saturated with water (viscosity low but compressibility finite) are ([151] Todd, 1973):

$$\frac{1}{K_{wat}} = \frac{1}{K_0} \left[1 + c\left(\frac{K_0}{K_{H_2O}} - 1 \right) \right] \tag{6.6}$$

$$\frac{1}{\mu_{wat}} = \frac{1}{\mu_0} \left[1 + n\frac{c}{\alpha} \right] \tag{6.7}$$

K_{wat} can be espressed in terms of K_{air}:

$$\frac{1}{K_{wat}} = K_{air} \left[\frac{1 + n\frac{c}{\alpha}}{1 + c\left(\frac{K_0}{K_{H-2O}} - 1 \right)} \right] \tag{6.8}$$

The difference between the "dry" and "saturated" bulk modulus obtained with the penny shape crack model, leads to an increment of compressional wave velocities in the saturated media, derived from:

$$V_P = \sqrt{\frac{3K_{wat}\left(1 - \nu\right)}{\rho\left(1 + \nu\right)}} \tag{6.9}$$

In Table 6.8, the V_p velocity values obtained from different theoretical models, are reported and compared with the ones obtained from US measurements performed in the laboratory.

Finally, sound velocity tests were performed by Kahraman ([72] Kahraman, 2007) on 41 different rock types, 11 of which were igneous, 15 of which were sedimentary and 15 of which was metamorphic. He showed that the difference between wet- and dry-rock P-wave velocities for igneous low porosity rocks (i.e. gneiss) could reach 2000m/s.

Porosity values of each sample were determined from the saturated and dry weights. Kahraman examined the P-wave velocity plots as a function of saturation degree: it was shown that after initial increasing with increasing saturation degree, P-wave velocity values were remained approximately same up to a saturation degree value depending on the rock properties. After a value defined as threshold saturation degree (SD_t), it was seen that P-wave velocity values were rapidly increased. The P-wave velocity plots as a function

Table 6.8: V_p velocity values obtained from different theoretical models (i.e. G: Gassman, N.&S.: Nur & Simmon) and compared with laboratory measurements: porosity aspect ratio have been assumed to sphere in fresh samples, penny-shape in microcracked samples.

crack shape	K_{sol}	ν_{sol}	K_{rock} G.	K_{rock} N.&S	ρ	ϕ	SD	V_P G.	V_P N.&S.	V_P lab
	GPa	-	GPa	GPa	Kg/m^3	-	-	m/s	m/s	m/s
sphere	43	0.35	42		2775	0.01	0.01	4725		4560
penny	43	0.35	3.3	3.25	2760	0.03	0.01	1327	1307	1582
penny	43	0.35	3.3	28	2760	0.03	0.99	1327	3809	4300

of saturation degree for some rocks are given in Figure 6.7. As shown in Figure 6.7, the SD$_t$ values vary between approximately 20% and 85%. Kahraman found that the SD$_t$ values largely depend on the velocity difference (ΔV_P), i.e. the difference between wet- and dry-rock P-wave velocities. There is an exponential relation between SD$_t$ and ΔV_P as shown in Figure 6.8. SD$_t$ values decrease with increasing ΔV_P values.
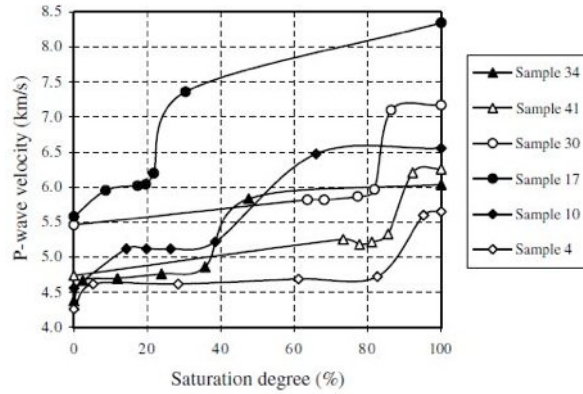
Figure 6.7: P-wave velocity as a function of saturation degree for some rocks. Sample 34: granite; Sample 41: granite; Sample 30: serpentinite; Sample 17: marble; Sample 10: travertine; Sample 4: travertine ([72] Kahraman, 2007).

113
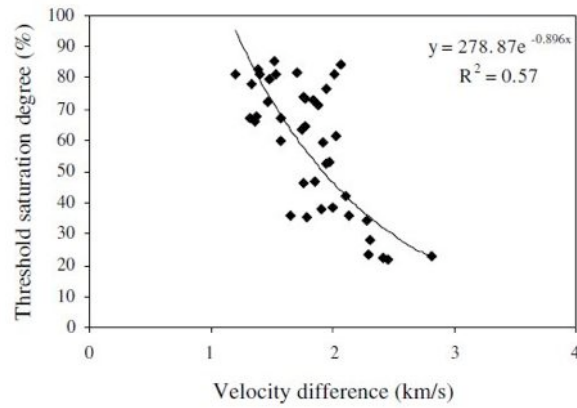
Figure 6.8: The relation between threshold saturation degree
and the velocity difference ([72] Kahraman, 2007).

Since the tested material is a thermally microcracked gneiss, results
obtained by Rotonda ([126] Rotonda, 1991) are also reported. Figure 6.9a)
shows the longitudinal and transverse velocity values for dry and saturated
marble specimens, as a function of treatment temperature. Graphs show how
the saturation conditions strongly affect longitudinal velocity. These values in
agreement with the theoretical models presented by Rotonda, i.e. DSCM,
according to which P-wave velocity values are significantly higher compared to
dry cracks condition. Figure 6.9b) highlights that even modest increases in
porosity resulting from thermal treatment, cause a sharp reduction in P-wave
velocity.
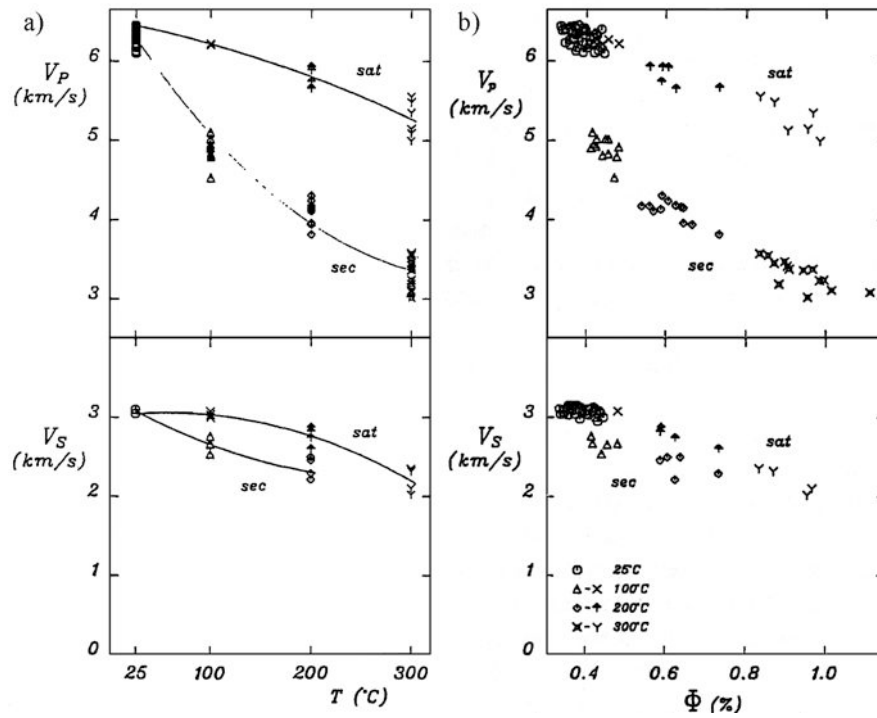
Figure 6.9: Elastic waves velocity for dry and saturated specimens of marble depending on: a) microcracking temperature; b) porosity values ([126] Rotonda, 1991).

115

P-wave velocity changes in the frozen sample

P-wave velocity of the tested Arolla gneiss sample has been measured under freezing conditions. Eight pt100 thermometers measured rock temperature at different depths to account for temperature homogeneity in the sample (-12°C). The P-wave transmitter-receiver was placed on the upper surface of the cubic sample, perpendicular to the cleavage/bedding direction. The traveltime of the P-wave was picked with an accuracy of 2 μs. The internal deviation induced by the measurement procedure was assessed by conducting four subsequent traveltime measurements. As shown in Figure 6.10, P-wave velocity increased significantly (14%) as a result of freezing: also this latter measure performed on the completely frozen Arolla gneiss sample, is in agreement with literature.
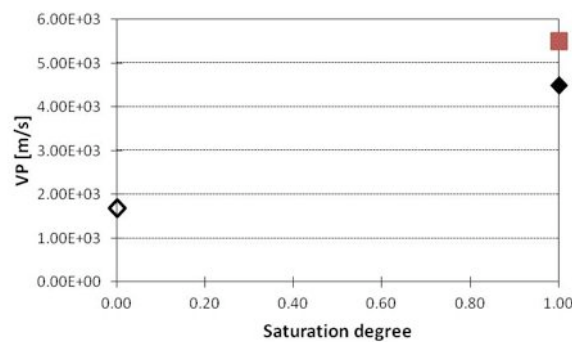
Figure 6.10: P-wave velocity of frozen (-12°C) Arolla gneiss sample (filled square); P-wave velocities of dry (blank diamond) and saturated (filled diamond) specimen, at 22°C.

P-wave velocity of freezing rocks was investigated in the laboratory mostly using polar high-porosity sedimentary rocks ([150] Timur, 1968; [39] Dzhurik & Leshchikov, 1973; [73] King, 1977; [115] Pandit & King, 1979; [116] Pearson et al., 1986; [123] Remy et al., 1994; [144] Sondergeld & Rai, 2007; [18] Bonner et al., 2009).
Low-porosity igneous rocks were studied by Takeuchi and Simmons ([146] Takeuchi & Simmons, 1973) and Toksöz et al. ([152] Toksöz et al., 1976). Early laboratory studies demonstrated compressional and shear wave velocity increases in freezing bedrock ([150] Timur, 1968; [73] King, 1977). Seismic

116

velocities increase at sub-zero temperatures until they reach a plateau when most of the pore fluid is frozen and the unfrozen water content is negligible ([115] Pandit & King, 1979; [116] Pearson et al., 1986). P-wave velocity of freezing rocks is controlled by the original water-filled porosity, i.e. the velocity corresponds to the changing proportion of frozen and unfrozen pore water content ([74] King et al., 1988).

Draebing and Krautblatter ([37] Draebing & Krautblatter, 2012) measured in the laboratory P-wave velocity of 22 decimeter-large low-porosity (<6 %) metamorphic, magmatic and sedimentary permafrost rock samples with a natural texture (>100 micro-fissures) from 25°C to -15°C in 0.3°C increments close to the freezing point (Figure 6.11). All rock samples show a P-wave velocity increase dependent on lithology due to freezing. P-wave velocity increases from 7.3±3.7% for gneiss to 78.5±7.0% for carbonate rocks parallel to cleavage/bedding; perpendicular measurements show an increase ranging from 11.1±2.4% for gneiss to 166.0±56.9% for carbonate rocks. The increase of P-wave velocity of carbonate rocks is independent of effective porosity, as has been outlined before by Wyllie et al. ([162] Wyllie et al., 1958). Especially schistosity strongly influences P-wave velocity increase perpendicular to cleavage due to freezing.
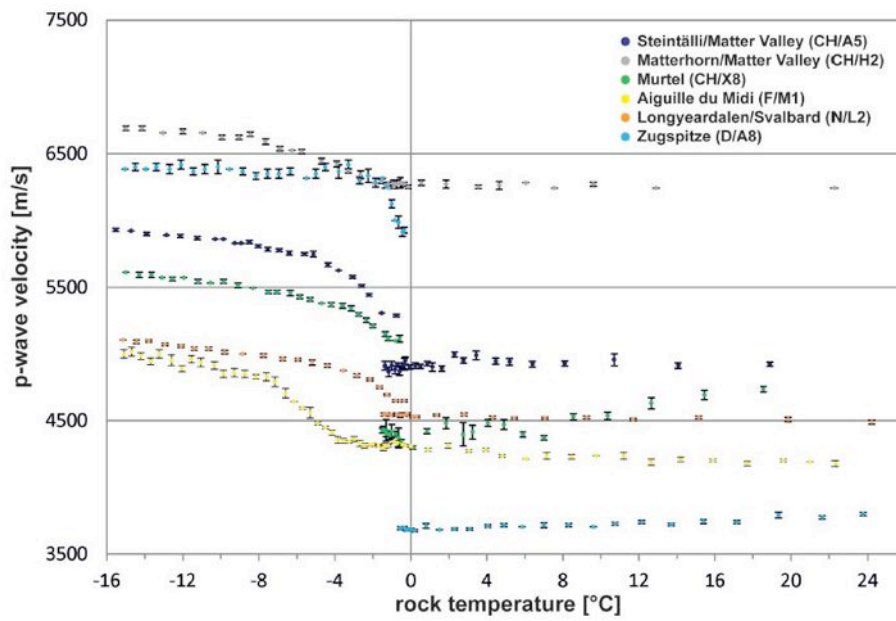
Figure 6.11: P-wave velocity of igneous, metamorphic and sedimentary rock samples measured parallel to cleavage or bedding plotted against rock temperature ([37] Draebing & Krautblatter, 2012).

Chapter 7

Detection of microfracture processes by acoustic emission

7.1 The source location problem

The use of AE technique seems to be a promising technique for studying frost weathering experimentally, also because in principle it permits continuous, non destructive determination of the approximate location of the microfracture events caused by ice growth in rock ([63] Hallet et al., 1991).

Solids emit low-level seismic signals when they are stressed or deformed; the sudden release of stored elastic energy generates elastic waves. The acoustic emission (AE) activity originates as the stress wave propagates undergoing attenuation as it moves away from the point where the material is mechanically unstable. These waves can be detected by surface or subsurface transducers, which sense the particle motion associated with the elastic wave. Many studies are dedicated to the AE monitoring during laboratory mechanical tests with the aim of better understanding of rock rupture mechanisms ([85] Lockner, 1993; [5] Amitrano, 2006). In fact AE analysis allows to characterize different mechanical behaviours of intact and jointed samples, as it is closely correlated to non-linear strain and can be used as a precursor of violent ruptures of intact as well as jointed samples ([7] Amitrano & Hantz, 1998). As a consequence, in laboratory, where the specimens are instrumented in order to monitor the AE activity associated with a particular test, surface mounted AE sensor are normally employed. The various sensors

may be installed in a variety of ways depending on the type of transducers and on the environment of the test specimen or structure.

For single point-like sources in geometries having continuous straight line ray paths between the source and each receiver, triangulation is usually the method of choice.

The travel time t_i from the source to the i-th receiver in a homogeneous medium is (e.g. Scholz, 1967):

$$t_i - t_0 = \frac{1}{v} \sqrt{(x_i - x_0)^2 + (y_i - y_0)^2 + (z_i - z_0)^2} \tag{7.1}$$

where $(x_i,\ y_i,\ z_i)$ and $(x_0,\ y_0,\ z_0)$ are respectively the spatial coordinates of the transducers in the receiving array and of the source; t_i is the measured arrival time at each station of the compressional wave generated by the transient event; v is a single velocity value, as the velocity field is assumed to be, for simplicity, both isotropic and homogeneous and t_0, is the unknown time in which the energy is released by the source (hereafter event time).

A similar equation can be written for each transducer. Each equation is a nonlinear combination of spatial coordinates.

The problem can be linearized if equations for two different receivers are squared and subtracted following the Arrival Time Difference (ATD) approach. The governing equations associated with the ATD approach represent hyperboloids ([48] Ge & Hardy, 1988, [49] Ge & Mottahed, 1994, [64] Hardy, 2003).

Consider two receivers i (selected as reference receiver) and k:

$$v^2 \left[(t_i - t_0)^2 - (t_k - t_0)^2 \right] = (x_i - x_0)^2 + (y_i - y_0)^2 + (z_i - z_0)^2$$
$$- (x_k - x_0)^2 - (y_k - y_0)^2 - (z_k - z_0)^2 \tag{7.2}$$

Expanding and simplifying:

$$v^2 \left[2t_0 (t_k - t_i) + t_i{}^2 - t_k{}^2 \right] = 2x_0 (x_k - x_i)^2 + 2y_0 (y_k - y_i)^2$$
$$+ 2z_0 (z_k - z_i)^2 + x_i^2 + y_i^2 + z_i^2 \tag{7.3}$$
$$- x_k^2 - y_k^2 - z_k^2$$

Finally:

$$t_0 v^2 (t_k - t_i) - x_0 (x_k - x_i) - y_0 (y_k - y_i) - z_0 (z_k - z_i) =$$
$$\frac{1}{2} \left[x_i^2 + y_i^2 + z_i^2 - x_k^2 - y_k^2 - z_k^2 - v^2 \left(t_i^2 - t_k^2 \right) \right] \tag{7.4}$$

Let's write:

$$a_{i,k} = v^2 \left(t_k - t_i\right) \tag{7.5a}$$

$$b_{i,k} = \left(x_k - x_i\right) \tag{7.5b}$$

$$c_{i,k} = \left(y_k - y_i\right) \tag{7.5c}$$

$$d_{i,k} = \left(z_k - z_i\right) \tag{7.5d}$$

$$p_{i,k} = \frac{1}{2} \left[x_i^2 + y_i^2 + z_i^2 - x_k^2 - y_k^2 - z_k^2 - v^2 \left(t_i^2 - t_k^2\right)\right] \tag{7.5e}$$

Then a, b, c, d, and p are auxiliary parameters that depend on known values related to receivers i and k. Equation 7.4 is a linear equation in terms of the event time t_0 and source coordinates x_0, y_0, and z_0. It can be written for each possible pair of receivers k with respect to a reference receiver i (supposed to be the receiver 1) as:

$$\begin{bmatrix} p_{1,2} \\ \cdots \\ p_{1,k} \\ \cdots \end{bmatrix} = \begin{bmatrix} a_{1,2} & b_{1,2} & c_{1,2} & d_{1,2} \\ \cdots & \cdots & \cdots & \cdots \\ a_{1,k} & b_{1,k} & c_{1,k} & d_{1,k} \\ \cdots & \cdots & \cdots & \cdots \end{bmatrix} \begin{bmatrix} t_0 \\ x_0 \\ y_0 \\ z_0 \end{bmatrix} \tag{7.6}$$

being the length of $\mathbf{p}$ equal to the number of transducer minus one.
The location requires the solution of the inverse problem that aims to solve for the event time and the coordinates of the source. $\mathbf{q} = (t_0, x_0, y_0, z_0)$ is the vector of unknown parameters.

The linearization of a nonlinear-equations system leads to a linear problem (equation7.6) that, in matrix notation, can be summarized in explicit form:

$$\mathbf{p} = \mathbf{Hq} \tag{7.7}$$

where $\mathbf{p}$ is the vector Mx1 (number of receivers-1) containing measured data, $\mathbf{q}$ is the vector Nx1 containing the values to be determined. $\mathbf{H}$ is a matrix MxN (sometimes referred to as kernel matrix), containing all the physical and geometrical information for the selected problem.
The comparison between the number of measurements M and the number of unknowns N provides a first indication on the problem type. The problem is underdetermined if the number of unknowns N exceeds the number of equations M, that is M < N. The converse is not necessarily true: interrelated measurements do not contribute to the pool of available information and problems that appear even-determined M = N or overdetermined M > N may actually be underdetermined.

It can be assumed that the measured vector is equal to the modelled vector plus a vector **e** whose components represent the departure of the measurements from the model ([103] Nelson & Yoon, 2000).
Thus:

$$\mathbf{p} = \mathbf{Hq} + \mathbf{e} \qquad\qquad (7.8)$$

The solution for the modelled vector **q** that ensures the "best fit" to the measured data has to be sought. The traditional approach to problems of this type is to find the "least-squares" solution for the vector **q** which ensures the minimization of the sum of the squared errors ("residuals") between the measured outputs and the model outputs.

7.2   Optimal sensor distribution

Among the advantages of the AE technique, the possibility of locating the source of the observed phenomenon, by analyzing the data from a suitable transducer array, is a matter of the greatest importance. In general, source location techniques involve the use of a number of AE sensors placed at various points around the specimen under study ([64] Hardy, 2003). The most relevant factors influencing source location errors have been identified in a U.S. Bureau of Mines Study ([145] Swanson et al., 1992):

1. biases of the numerical source location technique;

2. receiver array geometry;

3. uncertainties in receiver positions;

4. errors in picking arrival times;

5. uncertainties in seismic velocity structure.

The array geometry and the location of the event relative to the array play a major role in the source location error ([69] Jones et al., 2008). Each array has its own limits and error boundaries and, as a consequence, the suitability of a specific array should be investigated before its use.
In the present section, a tool for the identification of the optimal sensor position on a cubic shape rock specimen, monitored with an acoustic emission (AE) array during a campaign of laboratory tests, is presented.
The importance of a correct receiver array distribution and the details of the adopted solution for the experimental design together with the technical problems and limits of the proposed method, are also evidenced.

122

7.2.1   Condition number

In an isotropic velocity medium, three-dimensional surfaces of constant relative arrival time, or isochrons, can be constructed for each pair of receivers reporting first arrivals ([145] Swanson et al., 1992). This three-dimensional hyperboloid surface, which is symmetric about the line connecting the pair of receivers, is a solution to equation 7.2, as explained in details in section 7.1.

The infinite number of possible solutions for the source location on the hyperboloid surface is reduced by considering additional relative-arrival-time isochron surfaces from other receiver pairs. The mathematical solution for the event location can be graphically interpreted as common point of intersection of all of the isochron surfaces.

When errors in travel time are added to the exact relative-arrival-time data, the isochron surfaces do not intersect at a point, but instead cluster throughout a volume. The size, shape, and orientation of this volume depend not only on the magnitude of the errors, but also on the angle of isochron surface intersection: the receiver locations, i.e. the array geometry, determines these angles ([145] Swanson et al., 1992).

The array geometry itself does not induce any errors: it merely amplifies errors already present. The essence of this amplification in terms of geometry is that the source is incorrectly located on an adjacent hyperboloid rather than on the one associated with the true source. Thus, the density of hyperboloids in the region of the true source is a measurement of potential source location accuracy. Moreover the effect of array geometry on source location accuracy is a result of the non-uniformity of the hyperbolic field, which makes the location error heavily dependent on the position of the true source relative to the array. Maximum constraint on the solution can be achieved by minimizing measurement errors and selecting an optimum receiver geometry such that the number of isochrons that intersect at small angles is minimized. This is achieved by completely surrounding the events to be located with a three-dimensional distribution of receivers.

The optimal estimate of the vector $\mathbf{q}$ that minimizes a cost function related with the error vector $\mathbf{e}$, is given by

$$\mathbf{q} = \mathbf{H}^+\mathbf{p} \tag{7.9}$$

where $\mathbf{H}^+ = \left[\mathbf{H}^T\mathbf{H}\right]^{-1}\mathbf{H}^T$ is the pseudo-inverse of the matrix $\mathbf{H}$.

The sensitivity of the solution for $\mathbf{q}$ to small deviations or errors in $\mathbf{H}$ and $\mathbf{p}$, is determined by the condition number of the matrix $\mathbf{H}$ which has to be inverted ([103] Nelson & Yoon, 2000).

The condition number is defined by:

$$k\left(\mathbf{H}\right) = \|\mathbf{H}\| \|\mathbf{H}^+\| \tag{7.10}$$

where $\|\mathbf{H}\|$ denotes the 2-norm of the matrix $\mathbf{H}$. The 2-norm of $\mathbf{H}$ turns out to be equal to the largest singular value of $\mathbf{H}$ and is also equal to the square root of the largest eigenvalue of the matrix $\mathbf{H}^T\mathbf{H}$.

Thus, in terms of the singular value decomposition, $\|\mathbf{H}\| = \lambda_{max}$, where λ_{max} is the maximum singular values of $\mathbf{H}$. The 2-norm of $\mathbf{H}^+$ is given by $1/\lambda_n$, where λ_n is the smallest non-zero singular value of $\mathbf{H}$, and therefore the condition number can be written as

$$k\left(\mathbf{H}\right) = \frac{\lambda_{max}}{\lambda_n} \tag{7.11}$$

A simple argument can be used to demonstrate the importance of the condition number to the sensitivity of the solution $\mathbf{q} = \mathbf{H}^+\mathbf{p}$ to errors, for example, in the measurement of $\mathbf{p}$.

Let's assume that small deviations of $\mathbf{p}$ produce small deviations $\mathbf{q}$ in the solution,

$$\mathbf{H}\left(\mathbf{q} + \delta\mathbf{q}\right) = \left(\mathbf{p} + \delta\mathbf{p}\right) \tag{7.12}$$

A useful property of the matrix 2-norms is that $\|\mathbf{AB}\| \leq \|\mathbf{A}\|\|\mathbf{B}\|$ for two matrices $\mathbf{A}$ and $\mathbf{B}$. Since $\delta\mathbf{q} = \mathbf{H}^+\delta\mathbf{p}$, it therefore follows that $\|\delta\mathbf{q}\| \leq \|\mathbf{H}^+\|\|\delta\mathbf{p}\|$. It also follows that $\|\mathbf{p}\| \leq \|\mathbf{H}\|\|\mathbf{q}\|$ and therefore it is possible to write

$$\|\delta\mathbf{q}\|\|\mathbf{p}\| \leq \|\mathbf{H}\|\|\mathbf{H}^+\|\|\delta\mathbf{p}\|\|\mathbf{q}\| \tag{7.13}$$

And, using the definition of the condition number,

$$\frac{\|\delta\mathbf{q}\|}{\|\mathbf{q}\|} \leq k\left(\mathbf{H}\right)\frac{\|\delta\mathbf{p}\|}{\|\mathbf{p}\|} \tag{7.14}$$

This important and well-established result demonstrates clearly that the sensitivity of the solution $\mathbf{q}$ is determined by the condition number of the matrix $\mathbf{H}$ to be inverted; a large ratio of maximum to minimum singular value of $\mathbf{H}$ will greatly amplify small perturbations in $\mathbf{p}$ ([103] Nelson & Yoon, 2000).

The condition number also captures the transition from invertible to noninvertible matrices ([132] Santamarina & Fratta, 2005). A matrix is noninvertible when $k = \infty$. On the other hand, a matrix is ill-conditioned when k is very large; in this case, numerical inaccuracies become important to the solution, and errors in the data are magnified during inversion.

Condition number permits the assessment of the kernel matrix before data acquisition.

To find the maximum and the minimum singular values one can proceed as follows. The **H** matrix can be decomposed into three matrices, according to the singular value decomposition ([51] Golub & Kahan, 1965), in the form:

$$\mathbf{H} = \mathbf{USV}^T \tag{7.15}$$

where **S** matrix consists of the N singular values λ_n of the **H** matrix (MxN). The columns of the **U** matrix (MxM) comprise the left singular vectors of the **H** matrix, whilst the columns of the **V** matrix (NxN) comprise the right singular vectors of the **H** matrix. The matrices **U** and **V** are unitary and have the properties $\mathbf{U}^T\mathbf{U} = \mathbf{UU}^T = \mathbf{I}$ and $\mathbf{V}^T\mathbf{V} = \mathbf{VV}^T = \mathbf{I}$. The condition number can be obtained searching the maximum and the minimum among the singular values in the **S**-matrix and computing the ratio between the maximum and the minimum.

7.2.2 Proposed solution for an optimal distribution of 8 sensors on 5 free surfaces of a cubic sample

The experimental activity has been planned with the purpose of investigating the mechanisms of frost weathering in hard thermally-microfracturated rocks, trying to evaluate the physical condition in which ice action generates new ice lenses from propagated microcracks.

By recording the relative arrival times of AE signals at transducers mounted on the sample, it has been possible to locate the microcrack damage that occurs during prolonged slow freezing, as a function of time and temperature: in this manner, information concerning the complete nucleation and growth history is obtained. For this reason, it was necessary to reduce as much as possible the uncertainties on the micro crack sources location.

The experiment have been carried out with 8 sensors and 5 surfaces of the cubic sample available for positioning the sensors (the sample is placed on a basal cooling plate, so the lower surface is not usable).

Installing a receiver array (that could be comparable to an antenna), which could scan the volume to be monitored for AE sources, is very important but difficult to achieve in practice.

Receiver positions are typically constrained by available access due to the presence of other laboratory equipment.

Poor array geometries and/or poor wrapping by adequate geometries, can

125

greatly amplify the effect of small measurement errors and lead to inaccuracies in locations.

Constraining hypothesis

In order to select the optimum array geometry, the surfaces and the volume of the sample have been discretized. The 5 free surfaces of the sample have been discretized with a grid whose nodes identify possible positions for the receivers. To determine the node spacing, the accuracy of the acquisition system and the uncertainties of localization have been considered. As the sample is cubic shape 15 cm wide, each surface has been discretized by a grid with step 3.75 cm, so as to divide each surface into 16 squares. 45 possible sensors positions have been identified, corresponding to the nodes of the grid, and excluding those on the edges (Figure 7.1). In the central volume of the sample where, in this particular case, the ice segregation phenomenon and the resulting microcracks propagation should likely occur, 108 possible AE source positions have been considered. 3 planes of potential AE sources have been hypothesized, placed at 3, 6 and 9 cm below the top surface. Each plane has been discretized with a grid with a square mesh size of 3 cm, identifying 36 nodes corresponding to the potential AE sources for that level.

The combination of the 45 sensor positions taken 8 at a time gives a number of possible octets equal to about $2 \cdot 10^8$. To compute the kernel matrix and then the k-value matrix, each octet has to be combined with each one of the 108 source positions. Thus $2.3 \cdot 10^{10}$ k-values, among which the lowest values have to be selected, should be computed. As a consequence, this deterministic method would have been time consuming and would have required huge computational efforts.

To reduce the total possible sensor positions, a number of constraining hypotheses was introduced.

The first imposed constrain derives from the observation that three-dimensional source location can be very accurate if the sources are within the boundaries of the sensor array. Generally as the source moves from the center of the array the source location error increases. Thus to obtain a suitable sensor distribution on the specimen and to avoid the presence of un-instrumented faces, configurations with more than 2 sensor per face have been excluded.

Furthermore when the transducers of an array lay on a plane, the location error increases with the distance from the array plane. As a consequence it is desirable that the sensors do not lie all along the same plane or along parallel

planes. Based on this considerations, some other geometrical constrains were then imposed.

Since a plane in the space is defined specifying the position of at least 3 points, the 45 possible positions were combined, three by three, in order to identify all the obtainable planes. Fixed an initial a priori tern, an iterative process allowed to collect all the terns identifying non-parallel planes and, as a consequence, sets of points (corresponding to sensor positions) among the total 45 which do not belong to the same or parallel planes. Taking into account the uncertainty in time reading, theoretical geometrical planes has not been considered, but "thick planes". So that a point falling within the thick plane identified by other three sensors was excluded.

These sets of position were then combined, taken 8 points each time, obtaining 504 octet of sensors.

As a result of the application of these constraining criteria the **H** matrices to be evaluated dropped from $2 \cdot 10^8$ to about $5 \cdot 10^4$.
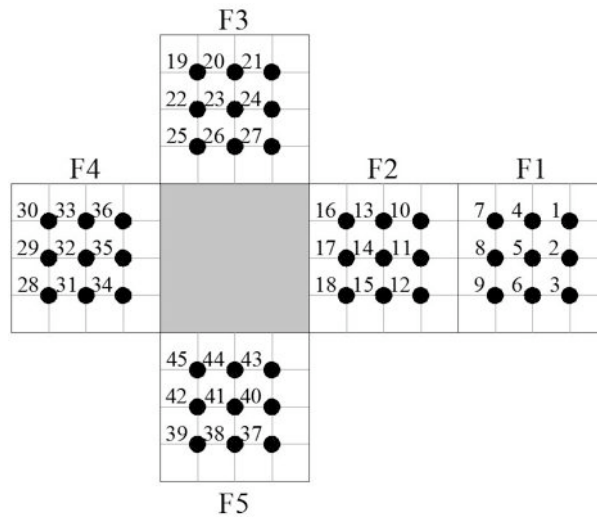
Figure 7.1: 45 sensor positions identified on 5 surfaces (upper surface, F1, and 4 lateral surfaces, F2 to F5) of a 15cm-cubic shape sample: they correspond to the nodes of a 3.75 cm-step grid. The lower surface (the grey one), is not available because the sample is placed on a cooling plate during the tests.

Results of K-Matrix computation

The condition number has been calculated combining each sensor octet to each source position and the results have been stored in a matrix **K** [108x504]. In Figure 7.2 the frequency distribution of the values stored in **K** is shown: on the histogram, values corresponding to the maximum and to the minimum (dashed line), and to the arithmetic mean (red solid line) of the condition number have been plotted; the one σ-interval (one standard deviation) from the average value of the distribution has also been identified (green solid lines). Three k-classes have been then identified: the green one, which contains k-values smaller then mean value minus the standard deviation (k <1.5), the yellow one, which contains k-values between 1.5 and the mean (1.5< k <2.6), and the red one, which contains k-values greater than the mean (k >2.6). The **K**-matrix containing the condition number computed combining all the possible combinations between identified octets of sensors and potential source positions, was plotted by giving to each k-value the color of the corresponding class. The resulting image is shown in Figure 7.3. The Figure 7.4 shows the **K**-matrix sorted in order to have along each column (corresponding to an octet of sensors) all cells green, yellow and red, respectively, grouped together: this means that the identification of the source position is lost, but the evaluation of the specific sensor configuration robustness results immediate. In fact the column order has been given growing, from the column with the minimum sum of all the 108 k-values, to the one with the maximum sum.

The selection of the optimal sensor configuration can be performed on the base of the observation of the sorted **K**-matrix. The best configuration is the one allowing the minimization of the condition number for all the potential source position, corresponding to the first column of the sorted **K**-matrix. The global minimum value of the condition number has been computed with the 156th configuration and for a source point placed at 6 cm depth. Four optimal configurations have been analyzed: the one with the minimum sum, the one with the minimum k-value, and two intermediate configurations. On the sorted **K**-matrix, these configurations correspond to column 1, 16, 70 and 156 respectively. In Table 7.1 sensor position are reported for each configuration: each number corresponds to a node in the grid that discretized the sample (see Figure 7.1) In Figure 7.5 the four box plots are shown: they graphically depict 4 groups of condition number data (corresponding to the 4 sensor configurations identified as optimal) through their five-number summaries: the smallest observation, the 25th percentiles, the median, the 75th percentiles, and largest observation; they also indicate which observations might be

128
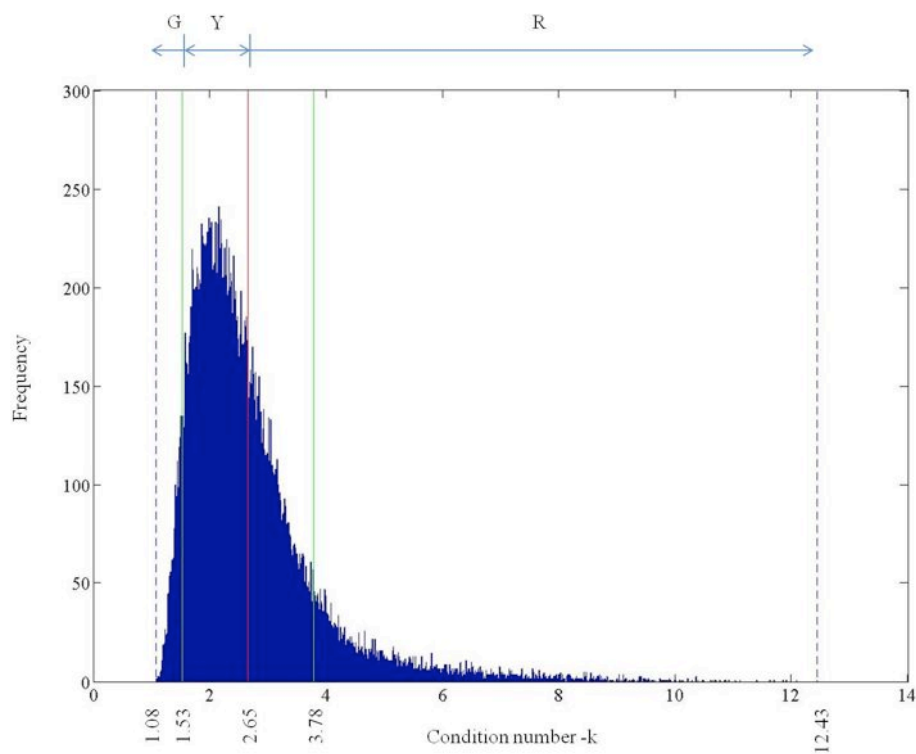
Figure 7.2: The frequency distribution of k: on the histogram, values corresponding to the maximum and to the minimum (dashed line), and to the arithmetic mean (red solid line) of the condition number have been plotted; the value of one σ-interval from average has been also identified (green solid lines).

considered outliers. The configuration number 1, which corresponds to octet of sensors designed on the flat representation of the cubic sample of Figure 7.6 has been chosen as the optimal configuration: as it can be seen from the box plot in Figure 7.5, this configuration ensures a low condition number for all source locations; the 156th configuration allowed to compute the global minimum condition number for a source position located in the middle of the sample, while for other source positions, the condition number increases and

129
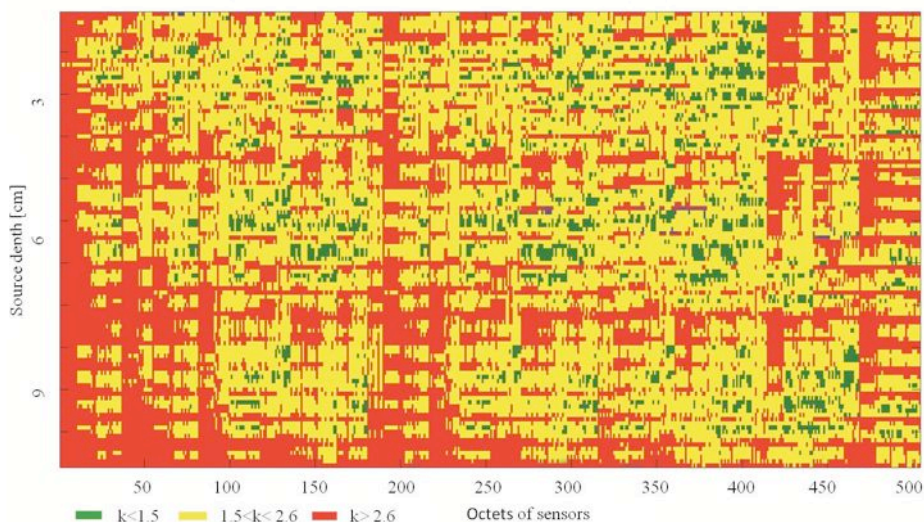
Figure 7.3: **K**-matrix plot, containing the condition number corresponding to all possible combinations between octets of sensors and potential source positions. To each k-value, the color of the corresponding class has been given.

Table 7.1: Sensor position configurations corresponding to column number 1, 16, 70, 156 of the sorted **K**-matrix.

ID column (sorted K-matrix)	Sensor position							
1	7	8	16	22	32	34	37	45
16	2	10	19	20	31	34	37	45
70	4	5	13	22	23	32	37	45
156	4	5	13	19	20	31	29	40

reach the maximum value in comparison with the other optimal selected configurations. Just perturbing some positions of the optimal configuration (the comparison between the two sensors array is shown in Figure 7.7), the corresponding median k-value doubles: this shows how a configuration that may seem appropriate, effectively doubles the relative inaccuracies in sources
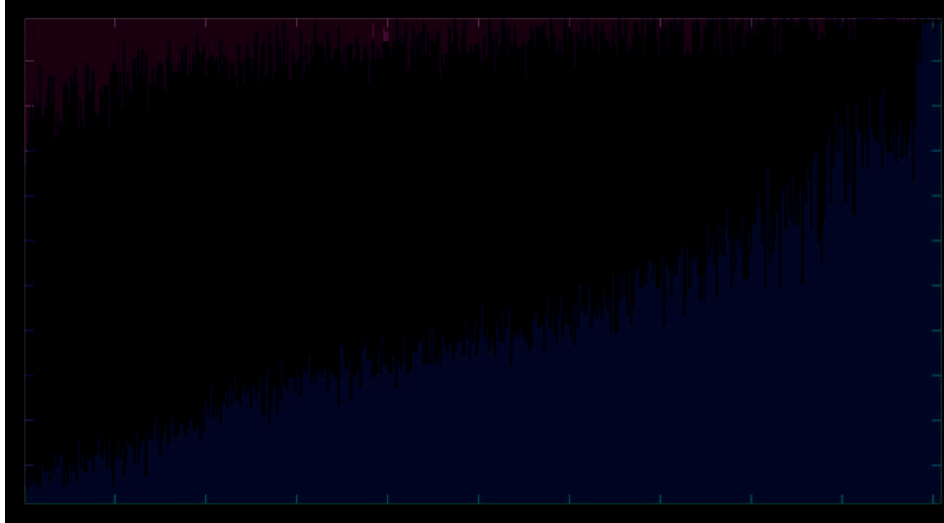
Figure 7.4: K-matrix sorted in order to have along each column (corresponding to an octet of sensors) all cells green, yellow and red respectively grouped. The columns order has been given growing, from the column with the minimum sum of all the 108 k-values, to the one with the maximum sum. To each k-value, the color of the corresponding class has been given (see Figures 7.2 and 7.3)

location. It has to be underlined that in any case condition number values are always very low; this confirms that the constrains made initially (see 7.2.2) are effective, already excluding k-values higher than 15.

131
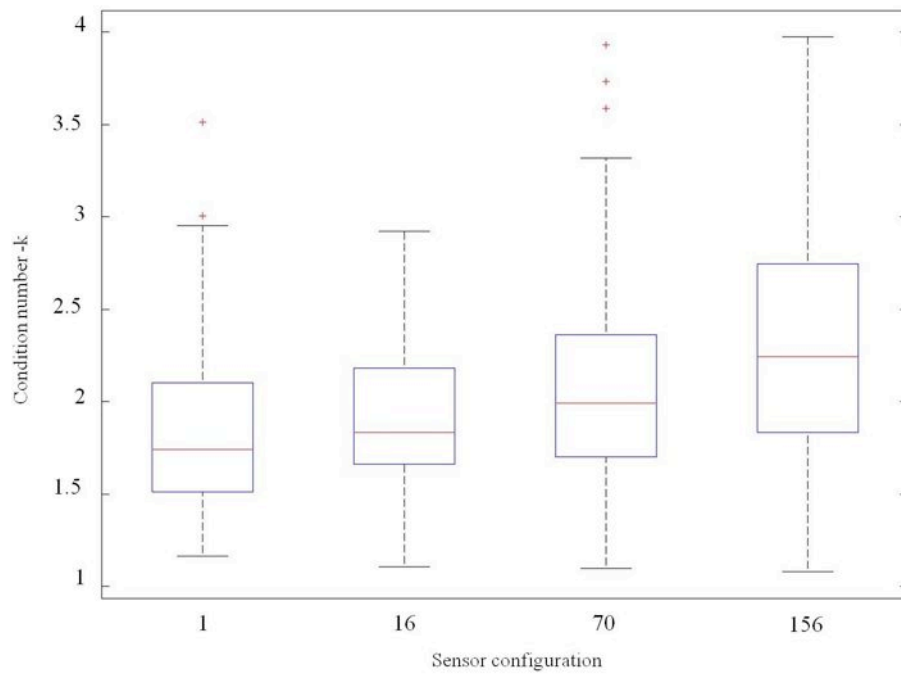
Figure 7.5: Four box plots graphically depict 4 groups of condition number data (corresponding to 4 sensor configurations) through their five-number summaries: the smallest observation, the 25th percentiles,the median, the 75th percentiles, and largest observation; they also indicate which observations might be considered outliers. On the sorted **K**-matrix, these configurations correspond to column 1, 16, 70 and 156.
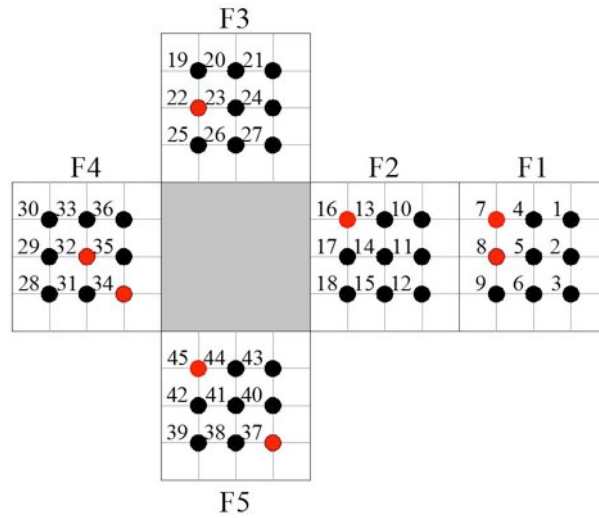
Figure 7.6: Optimal sensors configuration that optimize the reliability of the inversion with the lowest uncertainties propagation for sources located in the central 9 cm thick horizontal slice of the cube volume.
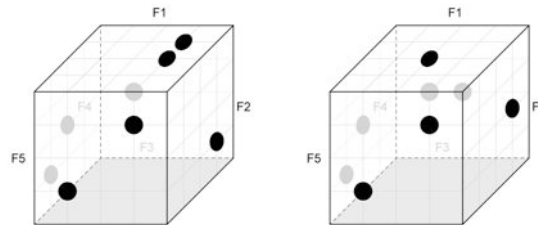
Figure 7.7: Optimal sensors configuration (on the right) that optimizes the reliability of the inversion and the perturbed one (on the left), that doubles the median k-value, and consequently, the relative inaccuracies in sources location.

133

Chapter 8

Experimental assessment of freezing phenomena

Matsuoka and Murton (2008) reviewed frost-weathering studies in the last years and proposed key questions to be answered.

Field monitoring has highlighted the roles of diurnal and annual frost cycles in controlling the timing and magnitude of frost weathering. In the laboratory, bidirectional freezing in soft, porous rocks has produced fractures containing segregated ice layers near the permafrost table, which imply the development of ice-filled fractures in permafrost bedrock over long time-scales. This finding, combined with numerical modeling of the thermal regime in permafrost rock slopes, contributes to the prediction of large-scale rockfalls and rock avalanches triggered by permafrost degradation ([93] Matsuoka and Murton, 2008).

Matsuoka and Murton have highlighted that future studies should also focus on explosive shattering, frost weathering of hard-intact rocks, field monitoring of ice segregation and bedrock heave, and the role of frost weathering in landscape evolution.

Concerning frost weathering of hard rocks composing high mountains, they proposed a questions to be answered: "Does microgelivation of hard intact rocks require an extant microcrack system developed by any process or inherited (e.g. Whalley et al., 2004)?".

Laboratory freeze-thaw tests have never proved the generation and propagation of new, visible cracks in hard intact rocks; they have only revealed a minor decrease in ultrasonic velocity or Young's modulus, or a minor

increase in porosity (e.g. Matsuoka, 1990b; Ondrasina et al., 2002; Whalley et al., 2004). The ice-segregation theory suggests that cracks in such low-porosity rocks (e.g. granite) propagate at low temperatures i.e -4°C to -15°C (Walder and Hallet, 1985), but laboratory simulations have so far induced ice segregation at higher temperatures ($>$-2°C) in high-porosity rocks (tuff and chalk).

This study would try to lead the verification of ice segregation and resulting crack growth in hard, intact rock with a laboratory simulation: upsizing of physical modeling experiments and monitoring natural unweathered bedrock, would provide valuable insights into permafrost landscape evolution and engineering geology.

Two laboratory test carried out at DIPLab (DIsaster Planning LABoratory, Politecnico di Torino) in 2012, will be presented in the following.

The first experimental test was aimed to reproduce the ice lens growth mechanism due to the onset of ice segregation processes at the interface active layer-permafrost table, actually building a physical model. To achieve this, long-term freezing test has been set up, in order to reproduce the physical conditions in which ice action generates ice lenses just beneath the active layer of the gneiss sample, as explained in section 8.1.

During the second trial, acoustic emission monitoring system has been installed. The application of this techniques to ice segregation experiments is a novel and promising strategy. This approach yields valuable new insights into the processes operating in evolving fault zone due to the ice lens growth. As a matter of fact, AE associated with grain-scale fracture can reveal the spatial and temporal distribution of damage (King et al., 2011). The details of this second laboratory test are shown in section 8.2.

The tested material is a thermally-microcracked Arolla gneiss, cubic shape, measuring $15 \times 15 \times 15$ cm, fully saturated (see 6.4); its characteristics are explained in detail in Chapter 6. No macrocracks or discontinuities were observed on the blocks, as shown in Figure 8.1.

8.1   Physical model

A long-term laboratory test simulating ice segregation process in rock will be described below.

Direct testing of the ice segregation model, requires specifically designed experiments: the methodology developed is the result of the experience gained
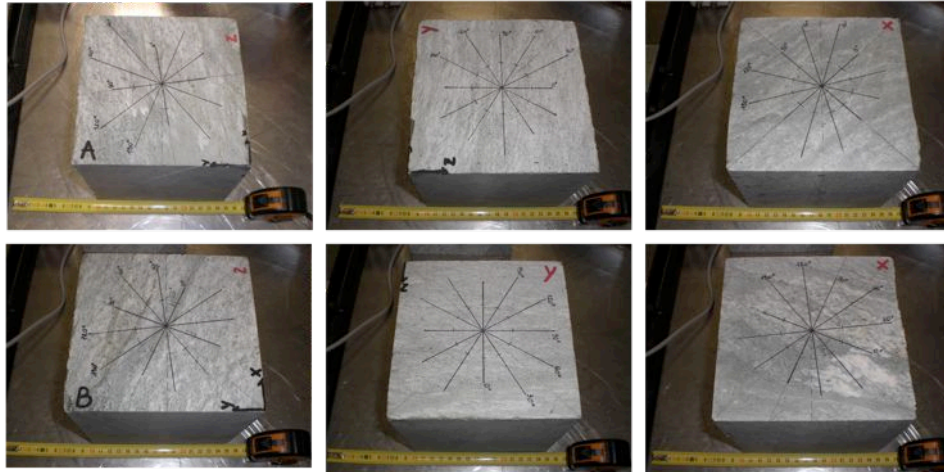
Figure 8.1: Pictures showing 6 surfaces of the rock sample at
the beginning of the experimental trail.

during the permanence in Grenoble, at Laboratoire de Geophysique Interne et
Tecnophysique, Université Joseph Fourier (see section 5.6). The heat transfer
and water transport have been essentially unidirectional and steady, in order
to induce fracture propagation by slow-continuous freezing and fixed
temperature gradient.

Moreover, thermal conduction models allowed to know the spatio-temporal
variations in the active-layer depth (see Chapter 4).

Uncoupled numerical analyses were performed using the FEM code ABAQUS
(see 4.2): they highlighted how steady temperature gradients play a
fundamental role in crack propagation, resulting tense not only for the
volumetric expansion of the ice contained within, but also because of opposite
deformations (contraction in the lower, colder part and expansion in the upper
warmer part) of the rock matrix that contains the defect (see 4.2.3).
According to the results obtained with the numerical model, the temperature
interval that would maximize the frost cracking mechanism in the rock sample,
has been chosen: -12°C on the lower surface, +3°C on the upper surface.

Numerical models of these experiments have been performed using the FEM
code CODE_BRIGHT, at the Department of Geotechnical Engineering and
Geosciences, UPC Barcelona (see 4.1). Fully coupled thermo-hydro-mechanical

simulations were carried out by coupling a description of transient heat and mass transfer in porous, freezing media described by Nishimura (Nishimura et al., 2009). These studies have addressed the mechanics of ice growth, particularly the role of the premelted films in lens growth, in order to do some prediction of the timing and depth of potential macrocrack originating perpendicular to the water flow from ice segregation processes. It was then decided that the test would last three months.

8.1.1 Freezing set up

In order to simulate permafrost and claiming to maintain the temperature gradient through the specimen equal to $1°C/cm$, the gneiss block have been placed on the basal cooling plate described in 5.3, providing effective direct-contact cooling: the thermoelectric controller has been set at -12°C (Figure 8.2a)). The temperature distribution has been assessed by a set of 9 Pt100 platinum resistance thermometers, described in 5.3.1. Eight sensors have been located adjacently to a vertical face of the specimen at different depths: 1.5, 3, 4.5, 6, 8, 10, 12, 14 cm; one sensor were placed on the upper surface of the specimen. A thermal compound has been used to fill the air-gaps between the thermosensors and the imperfectly flat and smooth rock sample surface, such as increasing the the thermal conductivity at the interface (Figure 8.2b)). All the resistors were connected with shielded three-wire conductors the acquisition system, made of an acquisition board (PC10 - AOIP product), which allows measurement, monitoring and storage of digital and analogue signals issued from electrical and physical sensors (see section 5.3.1).

All the lateral surfaces have been coated with a silicone layer, to maintain the sample saturated during the test and allowing water to be drawn from the saturated zones to the frozen rock (Figure 8.2c)). Then they have been covered by 10 cm of insulating material to minimize lateral heat transfer and ensuring a mono directional thermal gradient. The polyurethane foam has been sprayed inside a wooden box surrounding the sample and equipped with a suitable hole in the center, to allow placing the sample directly on the cooling plate (Figure 8.2d)).

As the presence of a nearby moisture source plays a fundamental role in ice segregation ([92] Matsuoka, 2001), a controlled supply of water have been guaranteed. A squared water pool has been fixed to the free upper surface of the sample and constantly kept full of water, so that a continuous downward water percolation could be available, ensuring a long-term, slow freezing test

under an open-system condition.

Finally an IR lamp have been installed at a distance of 55 cm from the top of the sample to reach a surface temperature of +3°C.

The cross section describing the sample configuration is shown in Figure 8.3.
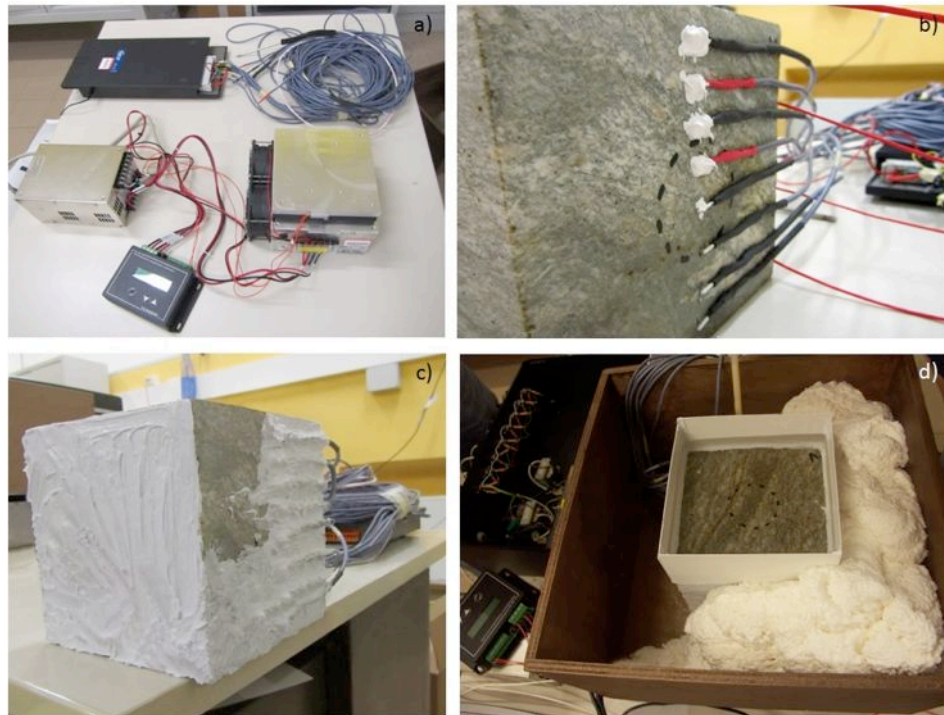
Figure 8.2: a) Cooling plate with thermoelectric controller and Pt100 thermometers connected to the acquisition board; b) Eight Pt100 thermometers located at different depths on a vertical face of the specimen (1.5, 3, 4.5, 6, 8, 10, 12, 14 cm), covered by thermal compound; c) preparation of the silicone layer; d) polyurethane foam sprayed in the wooden box surrounding the sample.
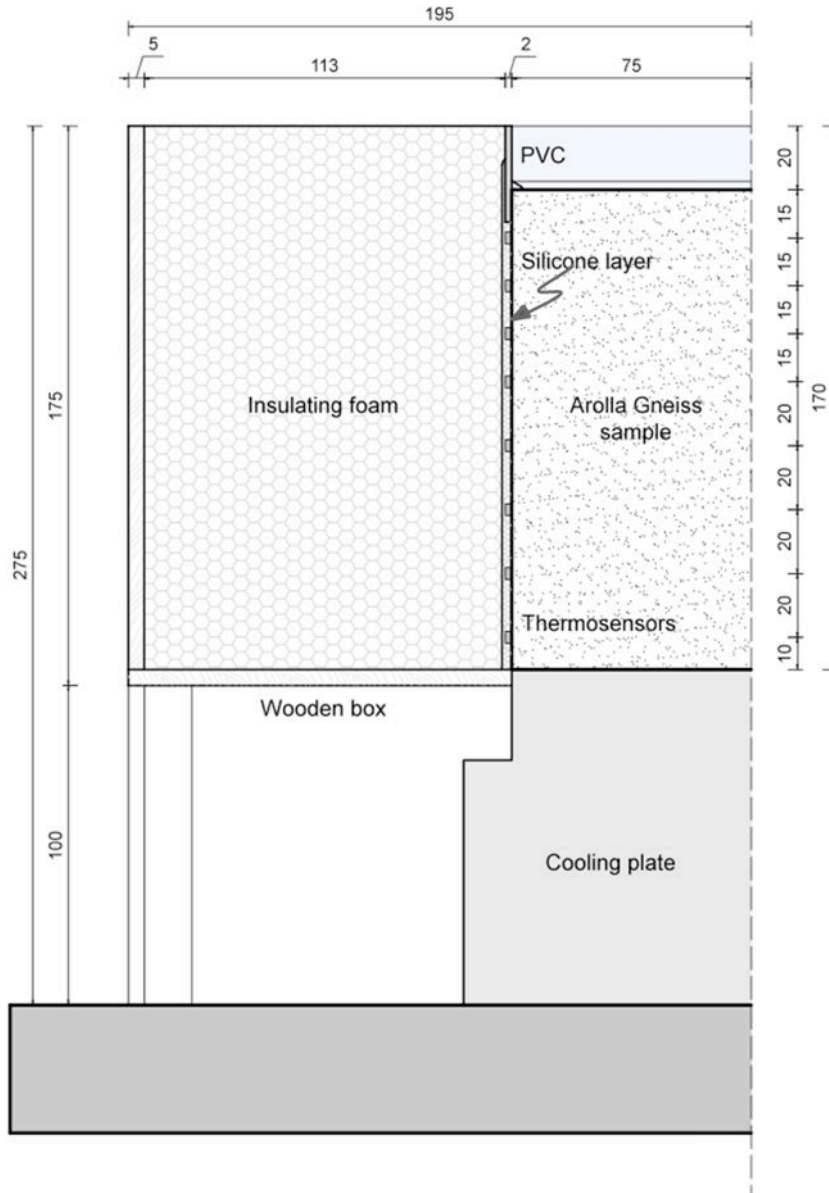
Figure 8.3: Cross section describing the sample configuration.

140

8.1.2 Results: fracture and segregated ice

At the end of three months testing, ultra-sonic measurement has been carried out on the sample, placing a P-wave transmitter-receiver on the upper surface of the cubic block: pulse transit time was recorded along the z-axis (normal to the isotherms). Figure 8.4a) shows the waveforms recorded when the sample was subjected to linear temperature gradient, simulating the active-layer and the permafrost body. It is possible to note a reflection in the profile, at about 20 μs: considering that the upper part of the sample was thawed, the depth of the reflecting element has been derived using a wave-velocity value equal to 4300 m/s (see 6.4.1). Finally, the corresponding depth was about 4.3cm.

The same procedure was repeated freezing completely the sample to -15°C. In fact, the reflection could have been caused by the pore water phase change at the interface active layer-permafrost, since that was just the lower limit of the frozen fringe, as derived from numerical models (see 4.1.2) and experimental temperature measurements. Also in this case a reflection at about 27 μs has been noted (Figure 8.4b)): the corresponding depth was about 4.1 cm, using a wave-velocity value equal to 5500 m/s (see 6.4.1).

The interface across which there was such a change in the elastic properties corresponding to the reflection in the waveform profiles, could have been a millimeter-scale fracture due to near-surface weathering of the gneiss sample, as a consequence to ice segregation phenomena induced during the test.

The sample was then cleaned and freed from the insulating polyurethane layer and from the silicone sealing, to examine ice-filled macro-crack and weathering features.

The block was found to have three distinct layers (see Figure 8.5). The upper and the lower thirds of the gneiss cube lacked visible cracks; the lower part contained only pore ice, whilst the upper part was water saturated. On the contrary, the middle third was fractured and rich in segregated ice, at average depth of 4.5 cm beneath the block surface (its top and bottom at average depths of 2.8cm and 5.1cm respectively).

Microcracks propagated horizontally through the gneiss, resulting in a continuous and thick macro-crack near the base of the artificial active layer of the simulated permafrost, as shown in Figure 8.6a).

In some cases, filling of ice was visible inside the crack, despite the cleaning procedure of the sample has melted the ice close to the rock surface: the ice was generally pure and white (bubble rich), as shown in Figure 8.6c), d). Such bubbles are common in natural segregated ice (i.e. [100] Murton et al., 2001), and they are parallel to the direction of heat and water flow during ice
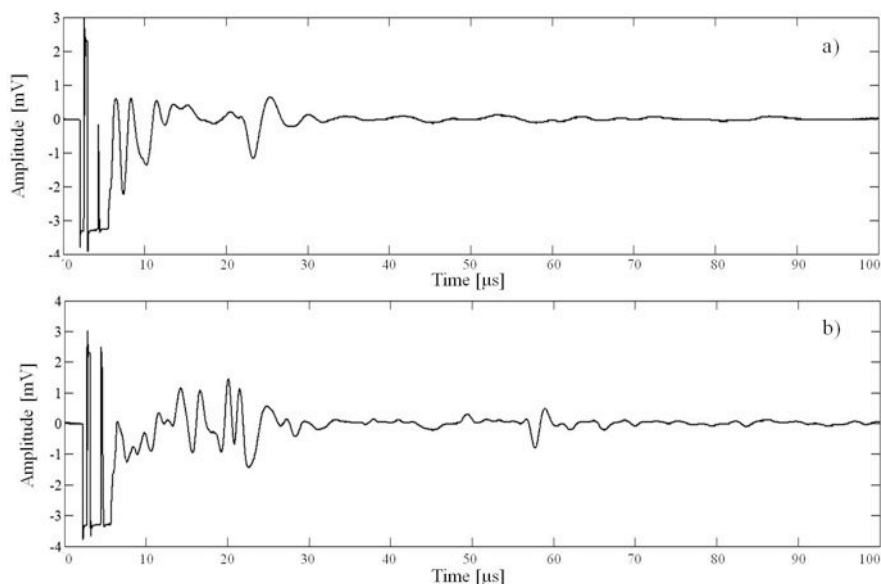
Figure 8.4: Waveform recorded during ultra-sonic measurements: a) sample subjected to linear temperature gradient: +3°C on the upper surface, -15°C on the lower surface; b) frozen sample at -15°C.

segregation.

The fracture was more or less horizontal, flat and parallel or sub-parallel to the cooling surfaces (i.e. the -2°C isotherm): the ice-lens growth was inferred within an approximate temperature range of -0.5°C to -2.5°C. This temperature range is consistent with Walder and Hallet theory (1985): although they proposed ice segregation temperature below -5°C for hard rocks characterized by low porosity (e.g. granite), this value entirely depends on the tensile strength of the rock, with weaker rocks (tensile strength around 2 MPa), breaking closer to 0°C. Considering the peculiarity of the thermally micro-cracked material that has been tested, (see 6), the rock temperature range for the ice lens growth agrees with literature data. Also the fracture depth is located in the layer between approximately 2.5 and 6 cm in depth and identified with the CODE_BRIGHT numerical model as "frozen fringe", where a considerable amount of water remains unfrozen, although the subfreezing

temperature. The temperature at the cold side of the frozen fringe is effective freezing temperature (below -3°C), and the the pore space is completely ice-filled; above the frozen fringe, the rock is instead unfrozen. In this thickness of 3.5 cm physical conditions that lead to the segregation ice occurrence are maximized, as explained in detail in 4.1.2 (see Figure 8.7).

143
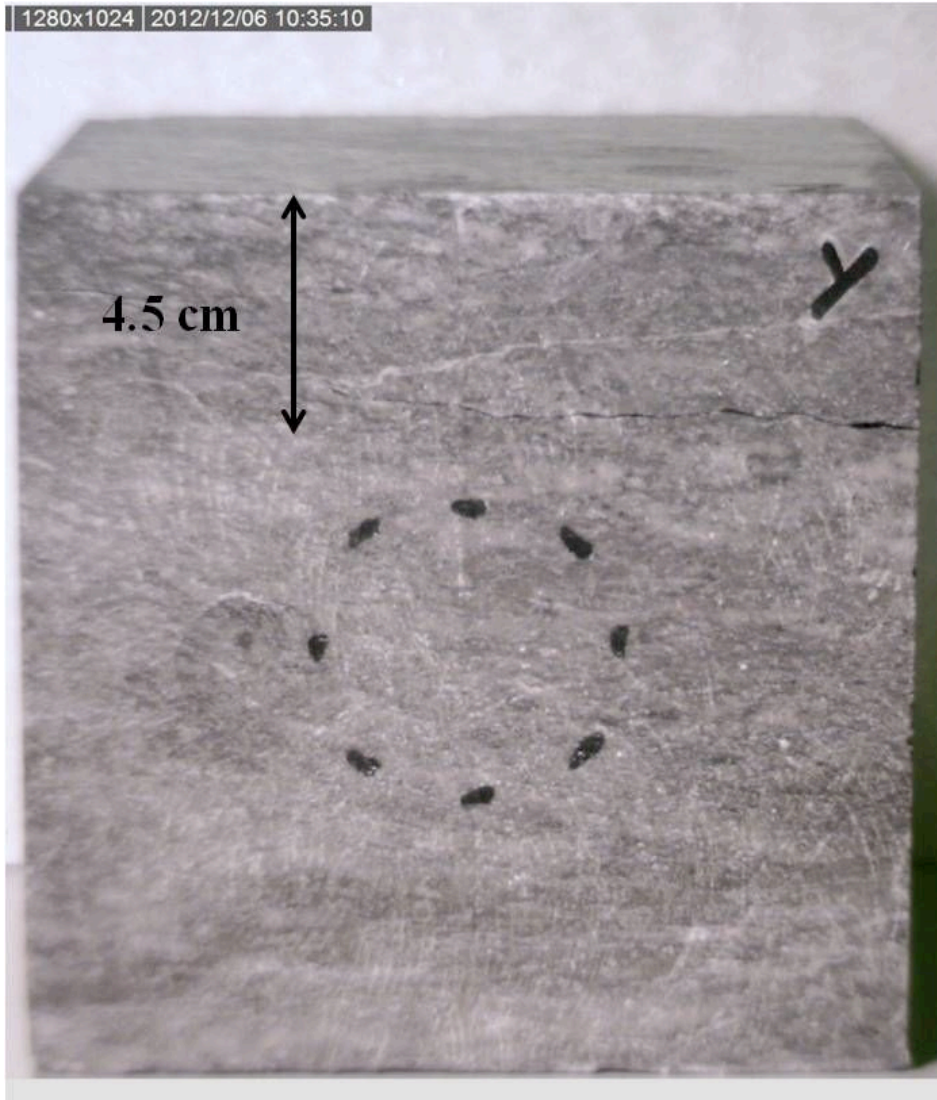
Figure 8.5: A crack on the specimen surfaces after three months of test: the fracture depth is at the base of the active layer.
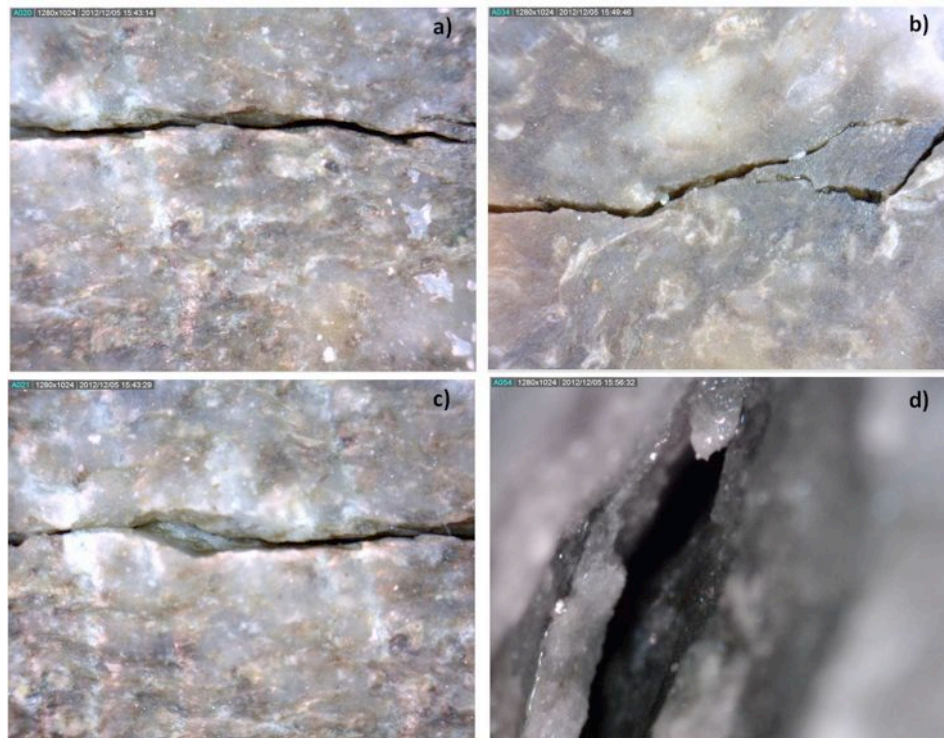
Figure 8.6: Microphotographs showing cracks on the specimen surfaces after three months of testing, simulating permafrost: a) continuous crack parallel to the cooling surface, 2 mm thick; b) progressive failure of micro rock bridges; c) ice-filled crack; d) thawed white bubble-rich ice, filling a crack.
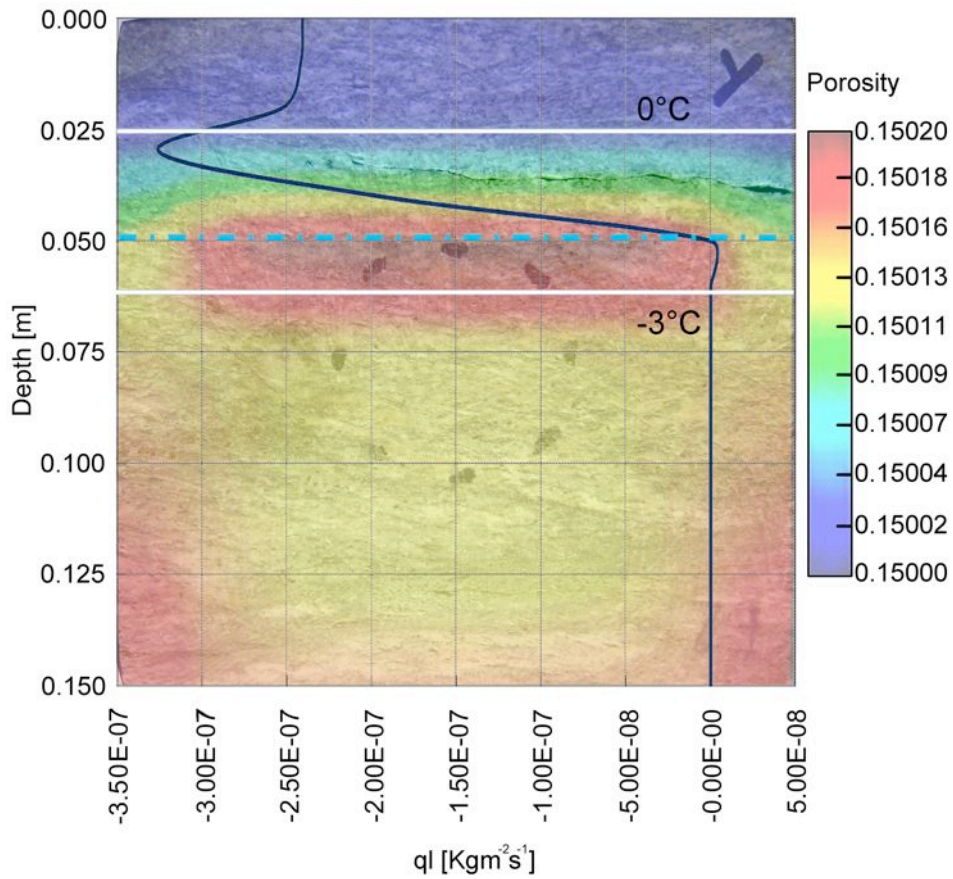
Figure 8.7: Superficial macro-crack located in the layer identified with the CODE_BRIGHT numerical model as "frozen fringe": this critical zone, is relatively permeable (the fluid flow reaches the maximum value equal to 3.25E-07 $Kgm^{-2}s^{-2}$) and the increase of porosity from the initial value demonstrates how the accumulation of freezing pore water is maximum in this critical zone.

146

8.2 Verification of ice segregation growth in microcracks using acoustic emissions.

In this section AE results from a second unidirectional freezing test will be presented. As the experimental results showed in 8.1.2 provided strong support for the segregation ice model of frost weathering, a system specifically designed to monitor the microfracture activity in the rock specimen under fixed temperature gradient has been used, to permit direct comparison with the theoretical model (see Figure 8.11).

An array of 8 AE sensors has been utilized to count and to determine the approximate location and amplitude of microfracture events. As a matter of fact, conventional measures of frost damage do not provide enough information about the magnitude, timing and location of frost-induced deterioration. Monitoring AE has been considered a suitable investigation tool for studying frost weathering experimentally, because it permits continuous, non destructive determination of the approximate location of microfracture events caused by ice growth in rocks. Furthermore, the rate of microcrack propagation can be assessed ([63] Hallet et al., 1991).

8.2.1 Sample configuration

The rock sample used in the test has been again a cubic block of thermally microcracked gneiss $15 \times 15 \times 15$ cm, as explained above; its characteristics are described in detail in Chapter 6. The specimen has been placed on the basal cooling plate, surrounded by the wooden box and then instrumented with eight Physical Acoustic sensors, model NANO30 (FN 54-61): AE sensor characteristics are stored in Table D.1.

The importance of a correct receiver array distribution and the details of the adopted solution for the experimental design have been evidenced in chapter 7.2. In order to select the optimum array geometry, the procedure presented in section 7.2.2 has been followed, choosing the configuration with the lowest condition number which would minimize source location errors due to the receiver array. The 5 free surfaces of the sample have been discretized with a new grid: in fact the lower part of the investigated volume (5 cm) has not been considered, since the depth of the AE activity due to ice segregation processes, was bracketed by the position of the -3 to -6°C isotherms, as experienced during the first freezing test (see 8.1.2); velocity values for saturated and frozen rock have been used (see 6.4.1 and 6.4.1). The **K**-matrix

has been computed, containing the condition numbers obtained combining all the possible octets of sensors identified on the grid nodes and potential source positions following 7.2.2. The eight sensors represented on the flat cubic sample in Figure 8.8 have been chosen as the optimal configuration for the second test (this configuration ensures a mean condition number for all source locations equal to 2.7).
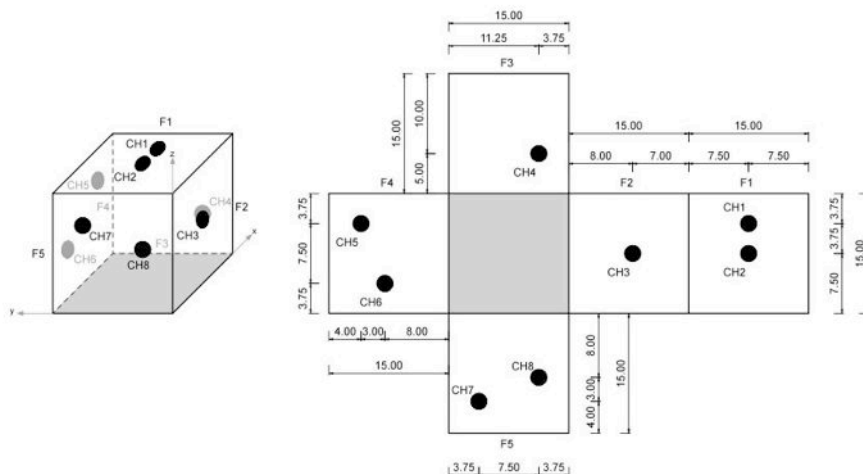
Figure 8.8: Optimal sensor position for the experimental test represented on the flat cubic sample.

Finally, each sensor has been collocated into a specifically designed and manufactured brass housing (Figure 8.9a)), which has been glued to the sample with X60 2-component fast curing adhesive (Figure 8.9b)); the coupling of each sensor to the rock surface has been preserved thanks to a stainless steel screw, opportunely turned. Then the lateral surfaces of the sample have been sealed with silicone to prevent water loss.
A rigid plexiglass cladding has been placed around the gneiss block: it has

148

been built with manually milled holes for the sensors, in order to ensure that they would remain attached to the sample surface (Figure 8.9c), d), e)). Everything has been surrounded by M12 screw bars to tighten the plexiglass against the rock (Figure 8.9f)), to avoid detachments due to expansion of ice on the sample surfaces or apparatus, as observed at some stages during the preliminary pilot tests (see Chapter 5). The gap at the interface between the siliconized rock surfaces and the plexiglass, has been filled with silicone grease to prevent condensation.
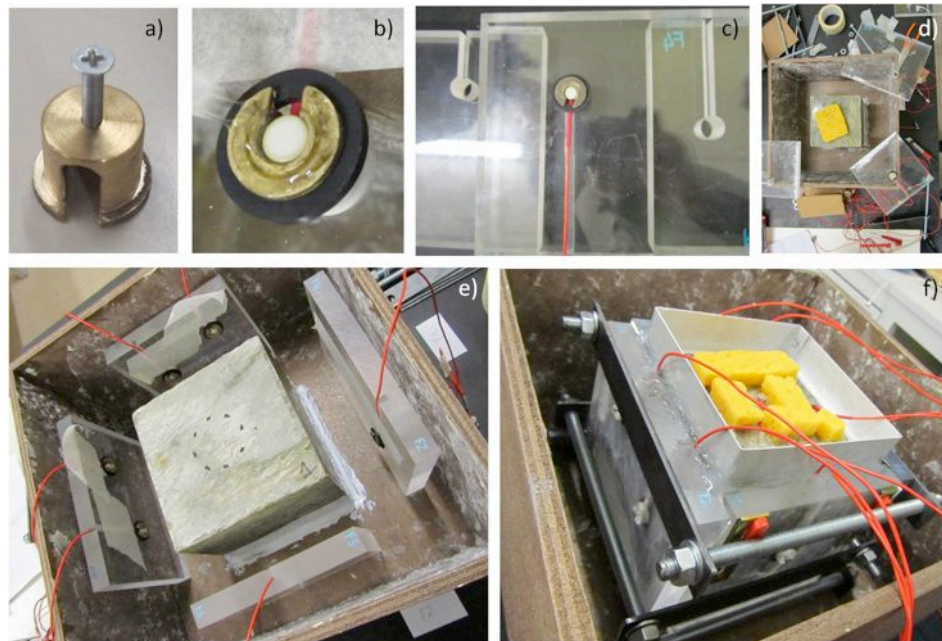
Figure 8.9: AE sensors installation: a) a sensor brass housing; b) X60 2-component fast curing adhesive to glue the brass housing on the rock-sample surface; c) plexiglass sheets with milled holes for the sensors; d) the wooden box surrounding the sample, with a suitable hole in the center, to allow placing the sample directly on the cooling plate: building up the plexiglass cladding; e) plexiglass sheets equipped with the sensors; f) M12 screw bars to tighten the plexiglass against the sample.

To provide lateral thermal insulation, Nesocell cellulose fiber has been

compacted in the wooden box, ensuring heat flow only in the vertical direction (Figure 8.10a), b), c)). Since the test setup provides the onset of a linear temperature gradient across the sample, and having monitored the temperature distribution during the first test, in this second trial thermal sensors have not been incorporated. The rock sample thermal regime has been controlled through the cooling plate thermocouple and checking the upper surface temperature with an infrared thermometer.

A controlled supply of water have been assured by a stainless quadratic pool glued on the top of the specimen, so that a continuous downward water percolation has been be available.

Around the pool, the space filled with cellulose was plugged with 8cm thick polystyrene sheets (Figure 8.10d)). The entire apparatus has been then covered by a transparent plexiglass sheet to avoid water evaporation, and a MDF sheet, drilled in the center to permit pool inspection (Figure 8.10e)).

Finally the IR lamp have been installed at a distance of 20 cm from the top of the sample (Figure 8.10e)), to induce a surface temperature of $+5°C$ and the cooling plate thermoelectric controller has been set at $-12°C$; in this way, the area of maximum AE activity would be lowered with respect to the previous test, so as to minimize the location inaccuracies due to boundary effects.

In order to reduce as much as possible mechanical vibrations from surrounding equipment that could trigger spurious events, a styrene-butadiene rubber (SBR) sheet has been placed on the test table, where all the equipment has then been built.

The cross section describing the sample configuration is shown in Figure 8.11.

Figure 8.10: Thermal insulation: a) sample of cellulose fiber provided by Nesocell; b) cellulose fiber compacted in the wooden box; c) stainless quadratic pool glued on the top of the specimen; d) 8cm thick polystyrene sheets around the pool; e) transparent plexiglass, MDF sheets and IR lamp installation.
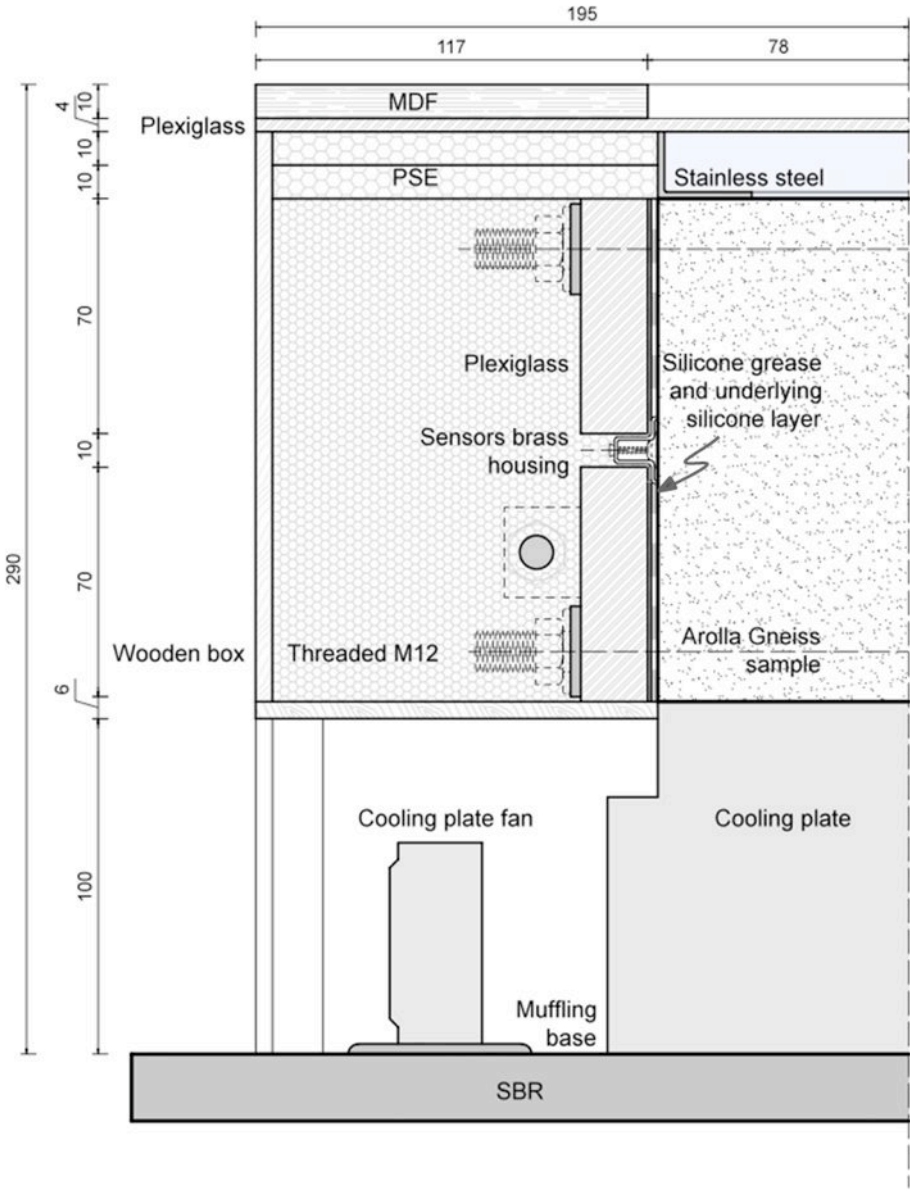
Figure 8.11: Cross section describing the sample configuration.

152

8.2.2 The AE detection system

The eight AE sensors, placed on the sample according to the optimal configuration shown in Figure 8.8, have been directly connected to eight differential preamplifiers, designed and manufactured specifically for this test, with fixed gain (40 dB) and fixed filter bandwidths (50 kHz - 30 MHz); the plug-in filter is in the Band Pass (BP) configuration, to optimize sensor selectivity and noise rejection (see Figure F.1a) and b) in Annex F). The circuit diagram is attached in Annex F. Each amplifier has been connected to the power supply through three pin cable (Figure F.1c)). Finally, they have been connected via the output signal BNC with BNC cables, to the Graphtech acquisition board (Figure F.1d)), whose characteristics are listed in Table E.1, attached in Annex E.
A diagram and a picture of the entire apparatus are presented in Figure 8.12 and Figure 8.13 respectively.
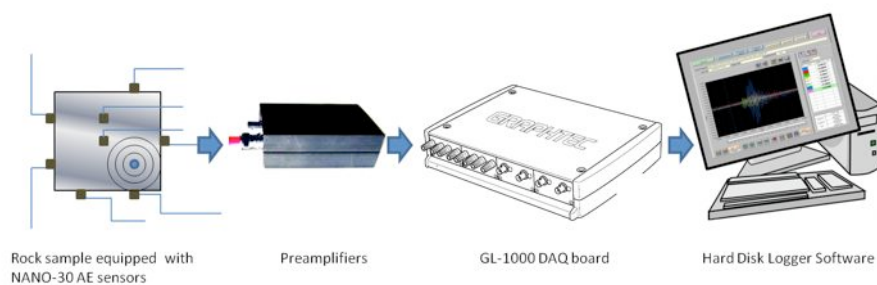
Figure 8.12: Acoustic emission monitoring system apparatus.

Hard Disk Logger Software has been installed on a central computer: recorded data have been registered in a compressed binary format files directly into the internal memory and daily transferred to an hard disk.A simplified scheme of the system functionality (revised from the Graphtec user's manual) is attached in Annex E, Figure E.1.

Figure 8.13: Laboratory equipment.

8.3   AE data analysis

The signals collected during the experiment monitoring AE activity, have been analyzed to determine the location of microfracture events caused by ice growth in the rock specimen.
In order to obtain an accurate location of AE events, two factors are important to know: velocity of the wave in the specimen and arrival time. The two aspects will be discussed in detail in paragraphs 8.3.1 and 8.3.2 respectively.

8.3.1   Pencil-break calibration test

In order to properly configure and calibrate AE instrumentation and sensors, an accurate and reproducible means of generating AE signals at known position, has been necessary.
A number of source simulation techniques including pencil lead or glass capillary fractures, pulsed transducers, spark sources, pulsed lasers, and gas jets have been investigated in literature ([120] Prosser et al., 1994). The pencil lead fracture is probably the most widely used method because of its simplicity, reproducibility, and good time response. A rapid rise time for the simulated source is desired to reproduce the broad bandwidth of signals observed from real AE events ([155] Vahaviolos, 1999).
This test consists of breaking a 0.5 mm diameter pencil lead approximately 3 mm from its tip by pressing it against the surface of the sample (see Figure 8.14). This generates an intense acoustic signal, quite similar to a natural AE source, that the sensors detect as a strong burst ([124] Roberts & Talebzadeh, 2003).
Pencil-break calibration test ensured that the transducers were in good acoustic contact with the rock block being monitored and it checked the accuracy of the source location setup, determining the actual value of the acoustic wave velocity.
The acquisition threshold is another important setting for the measurement of AE signals: signals whose peak amplitude is not large enough to cross the threshold are not detected. Setting the threshold too high will prevent potentially important signals from being recorded. Setting the threshold too low will cause the background noise to cross the threshold and will result in a great deal of unwanted data to be recorded.
A data acquisition time of 1 s and a sample frequency of 1 MHz have been selected; several attempts have been done, trying to configure a proper trigger setting in the acquisition software.

155

Only signals that have crossed a pre-defined threshold level have been recorded, obtaining a beginning identification and differentiation between signal and noise. The range has been set equal to 1 V and trigger threshold value chosen specifically for each channel selected:

- ch 1: 1%, i.e. 10mV;

- ch 2: 1%, i.e. 10mV;

- ch 3: 2.5%, i.e. 25mV;

- ch 4: 10%, i.e. 100mV;

- ch 6: 2.5%, i.e. 25mV.

Signal pre-trigger has been determined and set equal to 3s, in order to record a number of points to be included in the data capture prior to the trigger time: so every time that a signal on these given channels crossed the threshold value, measured points have been stored into the internal memory of the Graphtech acquisition board.

Using the velocity obtained from US measurement made on the frozen sample, equal to 5500 m/s (see section 6.4.1), pencil-break simulated sources have been re-localized, using "least-squares" solution approach explained in section 7.1.
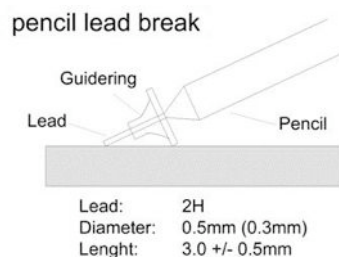
Figure 8.14: Pencil-break technique for calibration test.

Figure 8.16 shows signals selected as significant examples, corresponding to typical measurements situations.

8.3.2   Arrival time picking

Current AE analysis methods require to have an understanding of the relationship between the source and the resulting waveform characteristics,

Table 8.1: Pencil-break calibration test.

	X [mm]	Y [mm]	Z [mm]
Pencil lead source	85	112	150
Localized source	91	122	144
Absolute error	6	10	6
Pencil lead source	75	75	150
Localized source	82	61	160
Absolute error	7	14	10
Pencil lead source	47	103	150
Localized source	49	92	119
Absolute error	2	11	31

and then analyze the signals by visual inspection to classify and choose the arrival times. Considering that the sample frequency was fixed to 1 MHz, providing a time resolution of 1 μs, it corresponds to a potential position sensitivity of about 5.5 mm for 5500 m/s wave velocity. As the data recorded by AE sensors were affected by internal noise due to the electronics, sensor coupling, and background noise, signals were often partially or even completely swamped by noises, making it difficult to identify the actual arrival times of incoming signals.

The onset time is usually manually picked as the point where the difference from the background noise first occurs (Leonard, 2000): this could be very tricky when the difference between the noise and the signal is small, i.e. when the Signal to Noise Ratio (SNR) is low.

In the past few years, different approaches were used for phase arrival determination such as exceeding of threshold level, ratio of short-time average (STA) to long-time average (LTA) published by Baer and Kradolfer (1987), seismic wave polarity assumption published by Jurkevic (1988), neural networks published by Zhao and Takano (1999) and wavelet transform published by Anant and Dowla (1997). Saragiotis et al. (2002) published the high-order statistics based approach to automatically determine P-phase arrival of radiated seismic signals by skewness and kurtosis values of the recorded seismic waves.

An automatic method for objective onset-time picking has been applied to laboratory data in order to estimate arrival times: important aspects of data
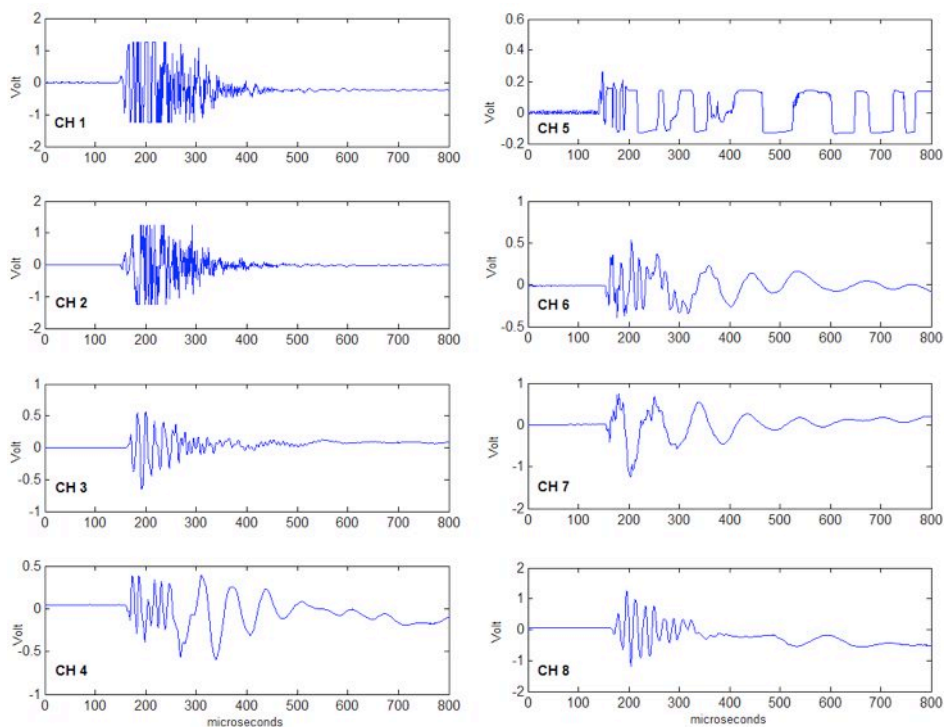
Figure 8.15: Seismograms divided by channel, derived from recorded data of the pencil-break calibration test 20121220_183306.

processing, filtering and de-noising, will be discussed in the following.

The main purpose of this work was to develop an automated procedure to pick the first wave arrival from large volumes of raw AE signals, supporting the visual inspection of each signal, that could fail in low SNR conditions.

The logical structure of the process could be divided into a blocks structure, through which the raw signals (first block) have been processed to extract arrival information (see Figure 8.17). The second block corresponds to the pre-processing section and includes filtering procedure of experimentally-recorded signals. The third block corresponds to optimal de-noising step using wavelet transform method, in order to obtain signals

158
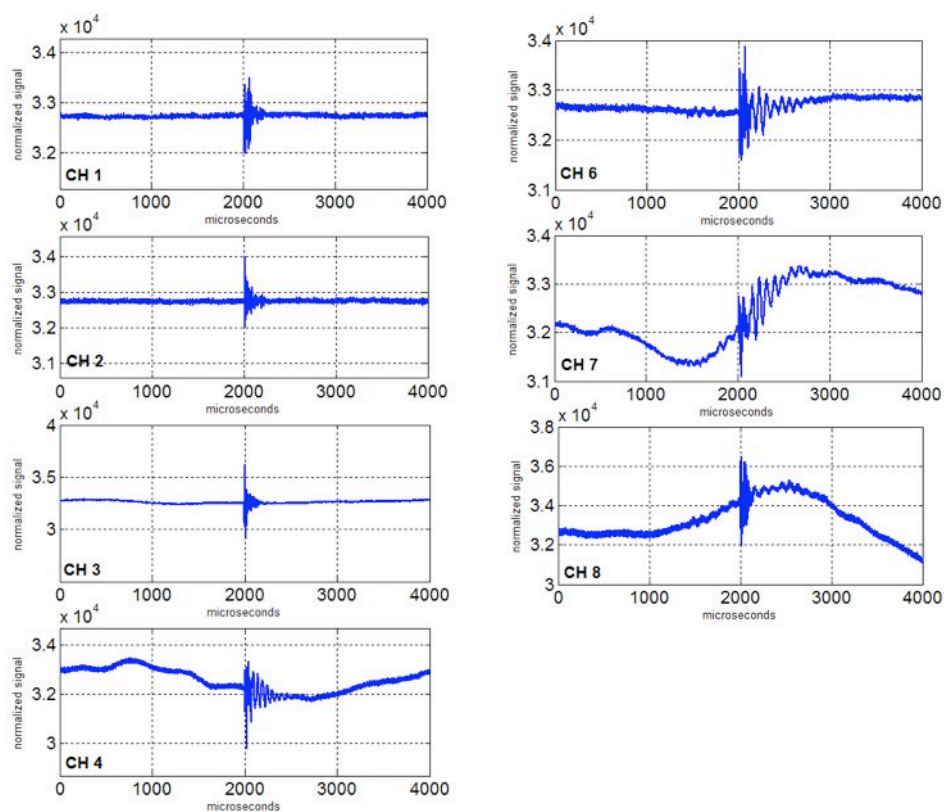
Figure 8.16: Seismograms divided by channel, derived from recorded data and registered in a compressed .GDT (event 20130106_162026).

with high SNR, which have clear arrivals and lower background noise. The fourth block is used to finally make the determination of the arrival time (output) on the best-quality signals (highest signal/noise ratio) by means of the Akaike Information Criterion (AIC), or doing purely manual picking.

The primary task in data processing has been to filter background noise. This has required a detailed study of the frequency distributions for both signals and noise. As a matter of fact, if the dominant frequency range for signals is different from that of noise, signals from background noise could be separate by

159
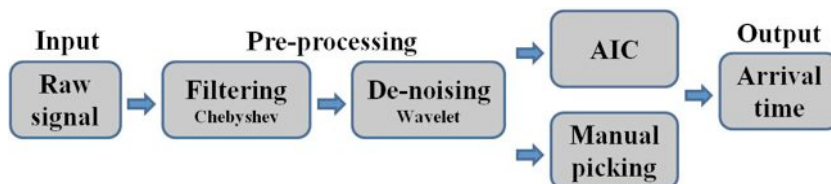
Figure 8.17: Block diagram of the semi-automated procedure to pick the first wave arrivals.

using a set of required filters.

A detailed study has been carried out on the characteristics of AE signals and noise, including a manual inspection of all waveforms from the database.

A Chebyshev Type I bandpass filter has been chosen, confining the signals in the range of 150-290 KHz, in order to preserve the important informations: it has been seen that these frequencies are exalted by accelerometers, considering the AE sensor calibration certificates attached in Annex G.

By using Chebyshev Type I bandpass filter, most of background noise has been filtered out. Figure 8.18 shows an example: 8.18a) is the original waveform, where the signal is present, but its arrival is buried by the background noise and cannot be determined. The filtered signal is shown in 8.18b).

The filtered signals have been then de-noised using wavelet transform method: as wavelet transform can be considered as a series of bandpass filters, whose results could be regarded as different mixtures of independent source signals ([140] Shao et al., 2011), the wavelet method has been use to drastic increase of the filtered signal to noise ratio.

Classically, the Fourier transform is used to analyze the frequency content of a given signal. However, it only gives a global representation of the signal in a given time-interval but does not allow to analyze its local frequency content or its regularity at a given point of the interval, especially when the signal is non-stationary ([134] [134] Sarout et al., 2009). It is well-suited for stationary signal analysis and allows for an ideal resolution in the frequency domain. But its resolution is poor in the time domain since the Fourier sine and cosine basis functions are stationary and have infinite duration.

In contrast, wavelet transform is a more general transformation to analyze more adequately transient signals ([134] Sarout et al., 2009). The proper choice of the wavelet family allows for an optimal filtering of the recorded signals in the time and frequency domains. This choice depends on the specific

160
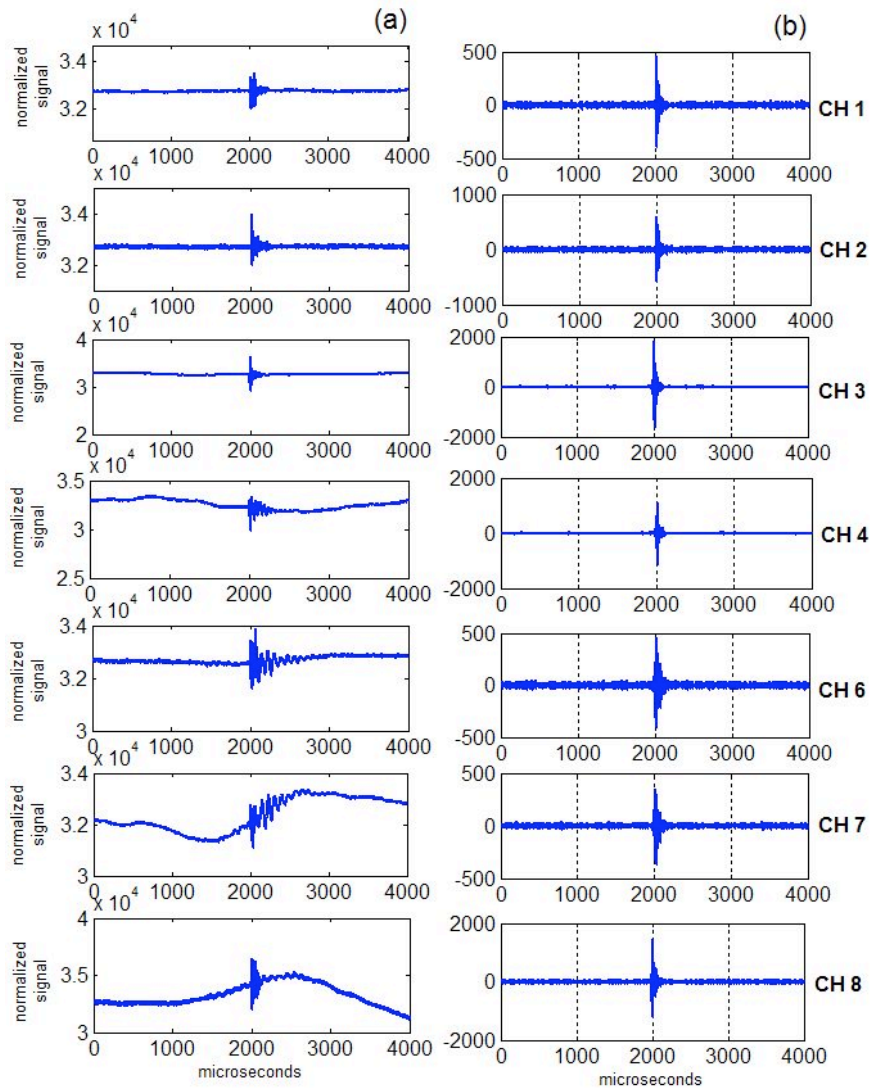
Figure 8.18: Event 20130123_131223: a) raw signals; b) filtered signals.

properties of the wavelet used in the analysis (type and scales) ([134] Sarout et al., 2009).

Therefore, the advantage of the wavelet transform over the Fourier transform, is its ability to characterize the structure of the transient signal locally with a detail matched to its scale (by stretching or squeezing a given wavelet). It allows for tunable resolutions in both time and frequency domains, depending on the type of wavelet family chosen for the analysis of a given time signal (decomposition basis). For instance, the wavelet time support (time interval of nonzero values of the wavelet) controls the resolution in the time domain, while frequency content of this wavelet (its "shape") controls the resolution in the frequency domain ([118] Peterson, 1997 and [167] Zhang et a., 2003).

An example of the de-noising performance with Daubechies wavelet dB3 at level 4 for a sample register, in shown in Figure 8.19.

Figure 8.19a) presents the raw seismogram time series; the filtered and the de-noised data in the time domain are shown in Figure 8.19c) and in Figure 8.19c) respectively.

After the pre-processing, a classification of the signals based on the signal-to-noise ratio has been made. SNR is defined as the amplitude ratio between a signal and the background noise: it is a measure that represents the difference between the level of signal and the level of noise, and it is normally represented in dB following the equation

$$SNR = 20 log_{10} \left(\frac{A_{signal}}{A_{noise}} \right) \tag{8.1}$$

where A is root mean square (RMS) amplitude.

The processed signals have been classified according to the following criterion:

* good signals: like the one presented in Figure 8.20, (SNR >15dB) which have clear arrivals, low background noise;

* medium signals: (SNR in the range between 10 and 15 dB), signals with a manual arrival picking distorted by the noise and normally incorrect.

* bad signals: are signals completely obscured by noise, with no possibility to extract an arrival or any other useful information (SNR < 10 db).

On the best-quality signals (highest signal/noise ratio) obtained from filtering and de-noising procedures explained above, the absolute arrival-time has been determined by means of the Akaike Information Criterion (AIC).

The Akaike Information Criterion belongs to the family of autoregressive (AR) methods ([142] Sleeman & van Eck, 1999 and [167] Zhang et a., 2003) based on statistical concepts (variance) ([134] Sarout et al., 2009).

Such methods are based on the assumption that the waveform may be divided into locally stationary segments (autoregressive process): AIC method ([76] Kitagawa & Akaike, 1978) is known to be effective for geophysical applications, either at the field scale ([167] Zhang et a., 2003) or at the laboratory scale ([83] Kurz et al., 2005).

Akaike showed through statistical considerations that a time series can be divided into two independent, and locally stationary, segments. For a given autoregressive process, the point at which the AIC function is minimum is the onset-time separating the preceding noise from the actual arriving phase, in a prescribed time window ([134] Sarout et al., 2009).

For a waveform $V_i(t)$ of length N, the AIC value at each sampling point j is defined as

$$AIC(j) = j\log\left[\text{var}\left(V_i\left[1,j\right]\right)\right] + (N - j - 1)\log\left[\text{var}\left(V_i\left[j + 1,N\right]\right)\right] \qquad (8.2)$$

where j ranges through all the waveform sampling points, and $\text{var}(\cdot)$ denotes the variance of signal data on the prescribed interval $[1,j]$ or $[j+1,N]$.

The AIC picker defines the onset point as the global minimum. For this reason, it has been necessary to choose a time window that includes only the waveform segments of interest ([134] Sarout et al., 2009): if the time window is chosen properly, the AIC picker is likely to find the sought phase arrival time accurately and in a repeatable (objective) way.

To accomplish this analysis, an appropriate time window has been chosen, taking 80 points before and 40 points after the trigger point and assuming that the window before contains noise and the window after contains the real signal.

An initial location of events recorded during the first two months of testing, has been performed to validate the automatic time picking technique explained above.

A homogeneous velocity model has been used in this preliminary phase: wave velocity was set equal to 5500 m/s, which is the value obtained from US measurement made on the frozen sample (see section 6.4.1).

AE sources have been then localized, using "least-squares" solution approach explained in section 7.1, using a specifically implemented MATLAB-base code. Figure 8.22 shows the localization results obtained from manual (red dots) and automatic (blue dots) time picking. As regards the manual time picking, the "high-quality" signals were discriminated visually, while using automatic time picking, "good" events have been classified on the basis of the SNR: in Figure

163

8.22, just signals with SNR>10 have been plotted.

Both the distribution of the localized AE sources, either the number of events classified suitable for the location, are comparable with the two techniques, confirming the robustness of the automatic method.

164
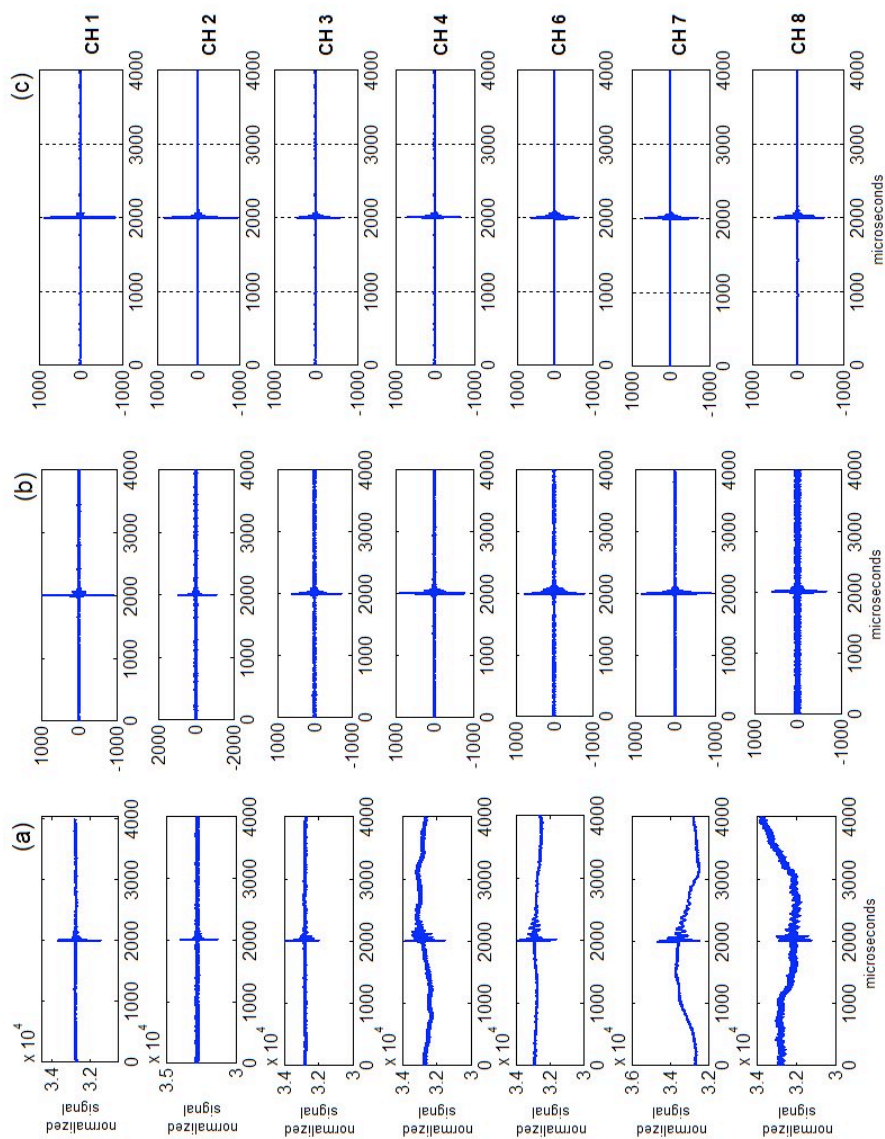
Figure 8.19: Event 20130222_092933: a) raw signals; b) filtered signals; c) de-noised signals.
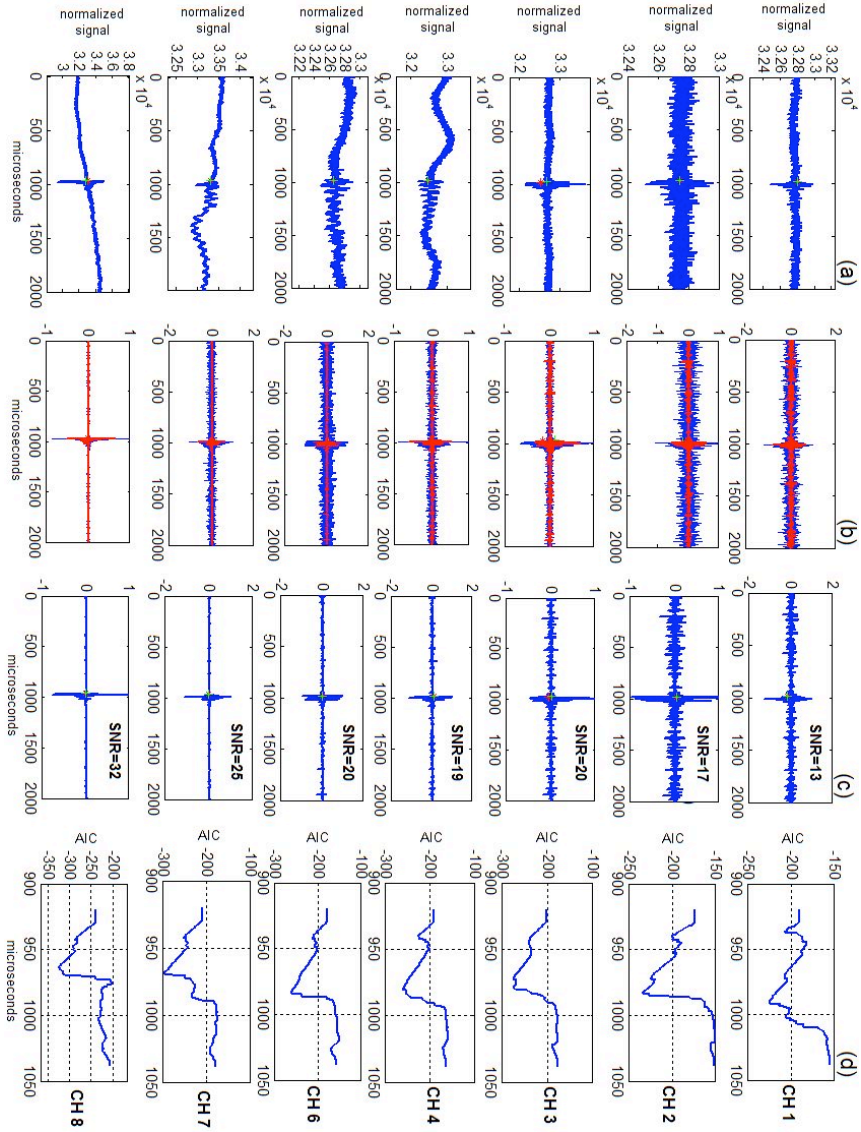
Figure 8.20: Event 20130224_034548: a) raw signals; b) filtered signals (blue solid line) and de-noised signals (red solid line); c) de-noised signals with the corresponding SNR; d) AIC functions. Green crosses correspond to onset points.
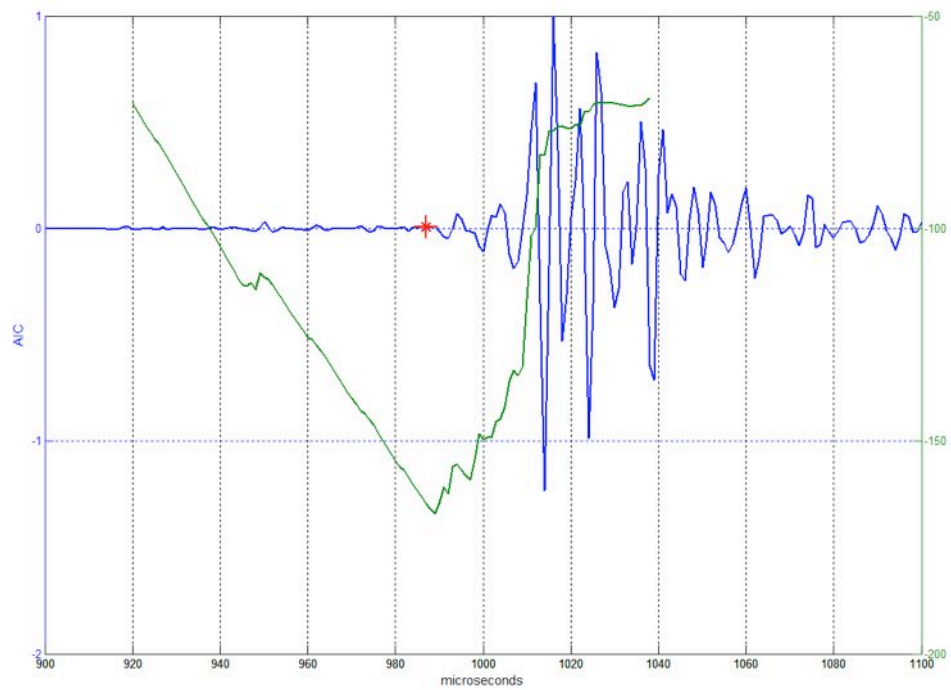
Figure 8.21: Event 20130302_200959: AIC picker (red cross) finding the onset point on channel 4 de-noised signal (blu line); AIC function has been plotted on the same graph (green line).
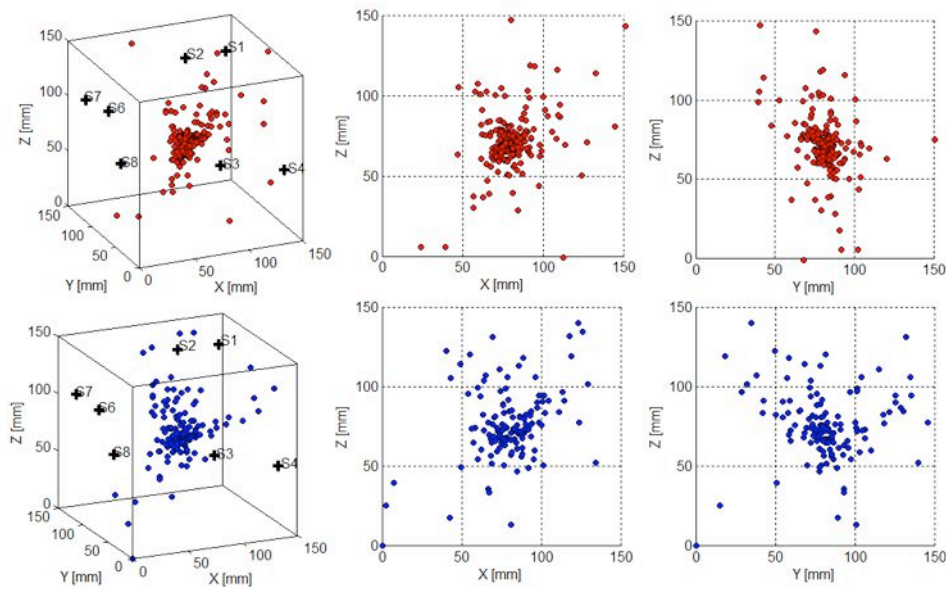
Figure 8.22: AE source location after two months of testing, using "least-squares" solution approach and homogeneous velocity model: red dots indicate the source location derived from manual time picking, blue dots indicate the source location derived from automatic time picking. Sensor position is plotted on the 3D graphs (black crosses).

168

8.3.3 Results: fracture and AE source location

At the end of three months of testing, the sample was cleaned to examine weathering features. The block was found to have microcracks propagated horizontally through the gneiss, resulting in discontinuous and thin macro-cracks near the base of the artificial active layer (Figure 8.23); the fracture depth was located approximately between 4.5 and 7.5 cm, layer that corresponds to the frozen fringe, in agreement with the experimental results described in section 8.1.2. The deepening of this band has been increased compared to the first test, since this time the surface temperature was set equal to +5°C (instead of +3°C), lowering the position of 0°C isotherm. Consequently, also the cracked area was located at greater depths, affecting the central part of the sample. Figure 8.24 shows the pattern of the macrocracks detected on the sample surfaces, while Figure 8.25 shows microphotographs depicting details of fractures induced by ice segregation mechanisms.

The following will show the results of AE source location due to the propagation of microcracks in the gneiss sample, compared with the experimental evidence.

Events recorded during three months of testing, have been filtered and de-noised according to the method explained in 8.3.2; on the best-quality signals (highest signal/noise ratio), arrival-time has been determined with the Akaike Information Criterion; the events have been localized using "least-squares" solution approach explained in section 7.1. All the procedure has been implemented in a specific MATLAB-base code, using a homogeneous wave velocity value equal to 5500 m/s (see section 6.4.1). The location of 227 events recorded during three months of testing and characterized by SNR>10, is shown in Figure 8.26. Histogram in Figure 8.27 shows the depth where the maximum AE activity was concentrated, i.e. the central zone of the sample (70-80 mm).

Although the location using the homogeneous velocity model has identified sources within the domain, the results evidenced the necessity of representing the heterogeneity of the material. The sample was in fact in a particular temperature regime, simulating permafrost and active layer, and the temperature distribution has determined the pore-water phase. By US measurements (see section 6.4.1), it was possible to obtain a wave velocity value at temperatures above the freezing point (i.e. when the water filling the microcrack was completely liquid), and at -12°C: at this temperature, water was completely frozen, as shown in Figure 4.5. Observing the water saturation
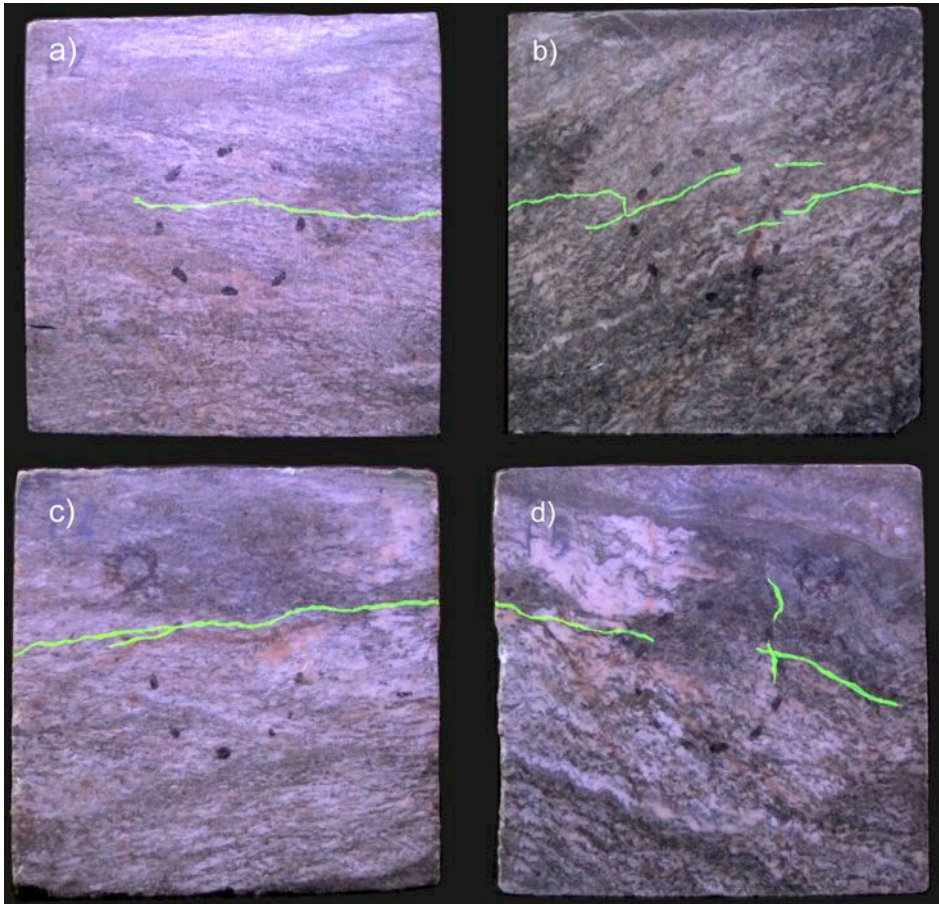
Figure 8.23: Pattern of the superficial cracks traced with fluorescent paint and photographed after exposing the sample to the Wood's lamp: a) surface F2; b) surface F3; c) surface F4; d) surface F5.

degree curve, obtained simulating an upward freezing problem with CODE_BRIGHT (see section 4.1.2), it is possible to recognize a transition zone, the "frozen fringe", where considerable amount of water remains unfrozen, although the subfreezing temperature.

170
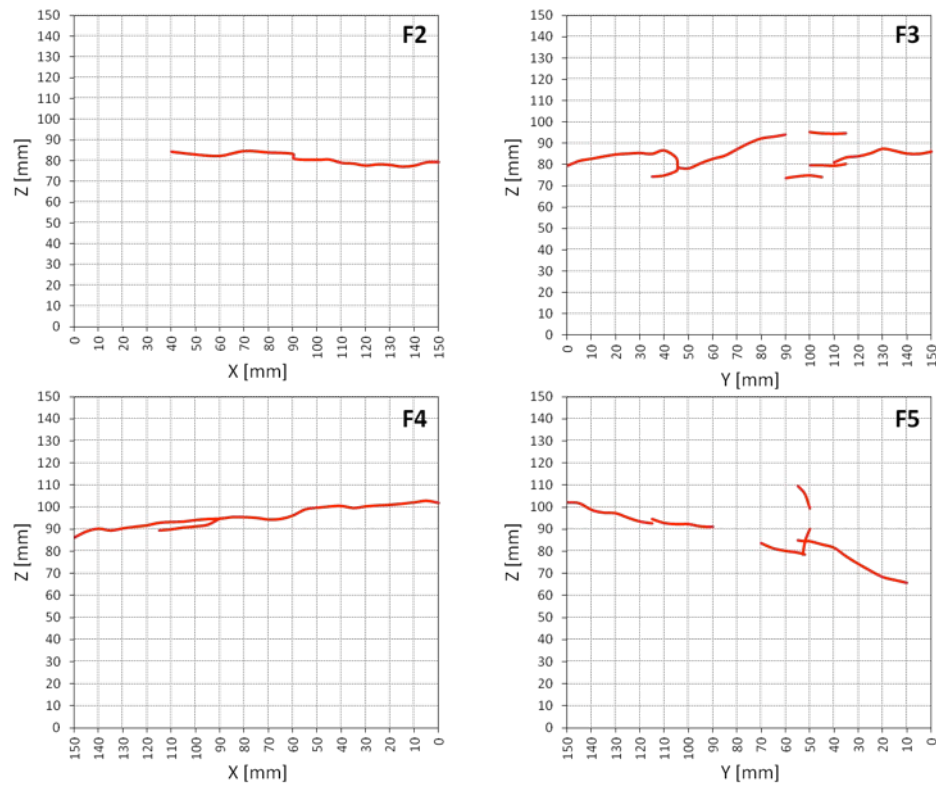
Figure 8.24: Pattern of the cracks detected on the sample surfaces after three months of testing.

Therefore, correlating the ultrasonic velocity with the thermal regime within the sample, and the resulting proportion of liquid water contained in the pores, it has been possible to recognize three layers of different thickness (as shown in Figure 8.28:

- the upper layer has been identified between the isotherm $+5°C$ (upper temperature boundary) and the isotherm $0°C$ (which was located at 4.5cm deep, assuming the temperature distribution with a linear gradient). This layer has been characterized by a wave velocity of 4300 m/s;

- the central layer, corresponding to the frozen fringe, has been identified

171
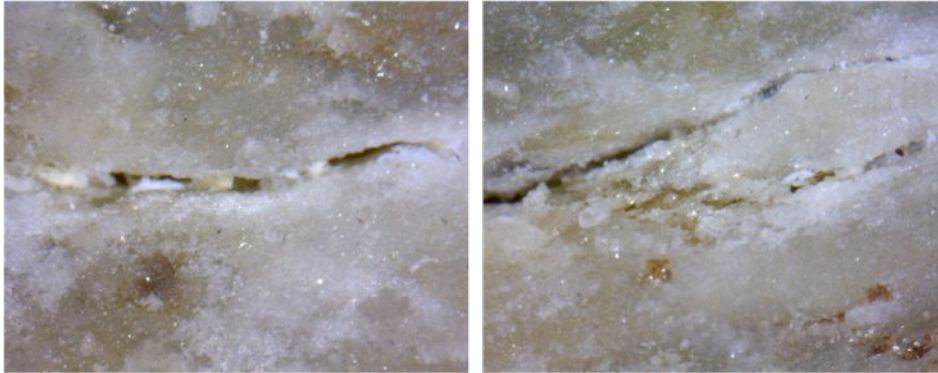
Figure 8.25: Microphotographs showing cracks on the specimen surfaces after three months of testing.
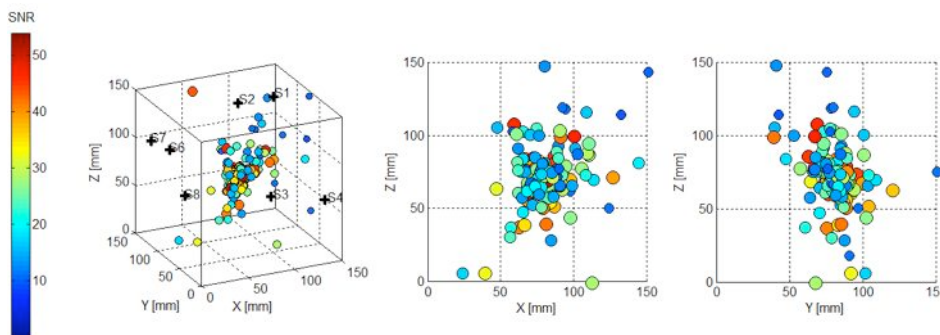
Figure 8.26: AE source location using "least-squares" solution approach, with a homogeneous velocity model, after three months of testing; each source (dot) has a color derived from the SNR that characterized the corresponding signal.

between 0°C and -3°C isotherms. Wave velocity has been supposed to vary linearly from 4300 m/s at 4.5 cm deep, to 5500 m/s at 7.5 cm deep;

- the lower layer has been characterized again by a homogeneous velocity value, equal to 5500 m/s, as temperature at the cold side of the frozen fringe was below -3°C and the pore space was completely ice-filled.

172
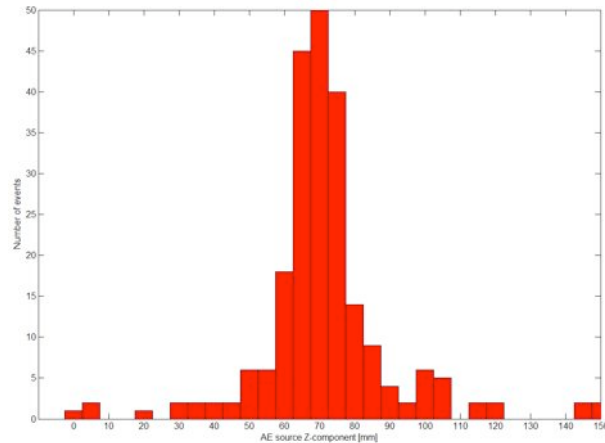
Figure 8.27: Histogram showing that the maximum AE activity is concentrated at 70-80 mm deep (AE source location obtained using "least-squares" solution approach, with a homogeneous velocity model).
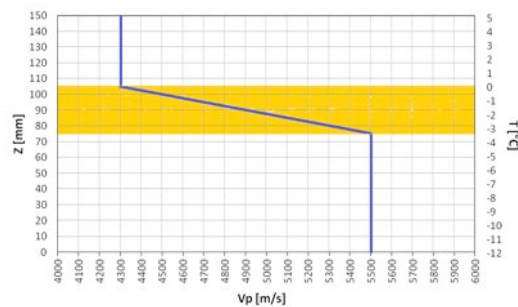
Figure 8.28: Horizontally layered velocity model: the orange band corresponds to the frozen fringe layer, where wave velocity varies linearly as a function of the water saturation degree curve.

NonLinLoc software has been chosen to be a suitable numerical code for AE source location applying a layered velocity model. NonLinLoc software package has been developed for probabilistic, Non-Linear, global-search earthquake Location, by Anthony Lomax ([86] Lomax, 2005).

The NLLoc program produces a misfit function, "optimal" hypocenters, an estimate of the posterior probability density function (PDF) for the spatial, x,y,z hypocenter location using different sampling algorithms, as described on the on line guide (http://alomax.free.fr/nlloc/). Metropolis-Gibbs sampling algorithm has been used for this analysis: it gives an estimate of the optimal hypocenter and an image of the PDF for hypocenter location ([87] Lomax et al., 2000).

The location algorithm used in NonLinLoc follows the inversion approach of Tarantola and Vallette ([147] Tarantola & Vallette, 1982). This formulation relies on the use of normalized and unnormalized probability density functions to express the knowledge about the values of known parameters (observed data).

The program was set on the non-global mode (allowing the location in a gridded rectangular-Cartesian volume). The location volume, inside which the software performs the iterations, was set as a cube of 15 cm side. This volume has been discretized into 1 mm side cubic cells. Arrival time at each AE sensor and AE sensor positions were the input parameters.
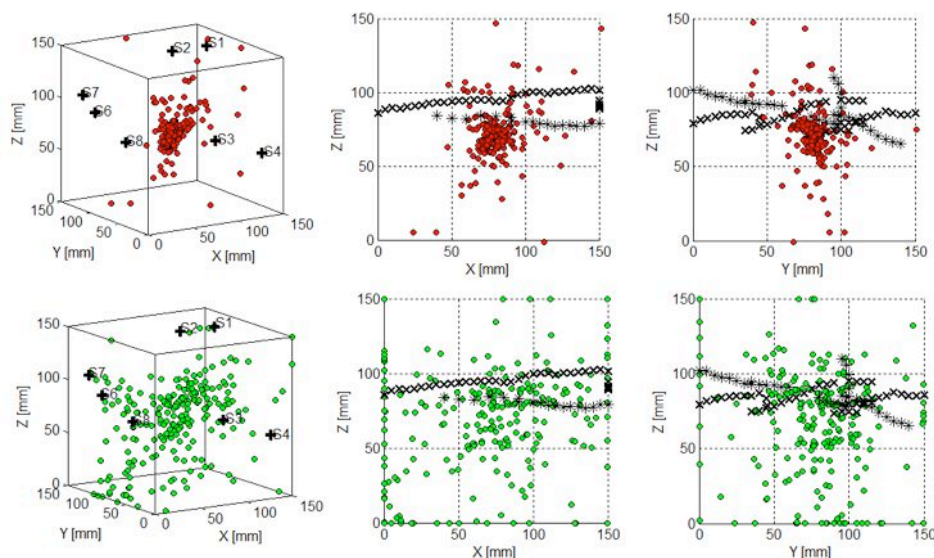
Figure 8.29: Hypocenter location of 227 high-quality events recorded during 3 months of testing. Red dots: AE sources localized using "least-squares" solution approach, with a homogeneous velocity model. Green dots: AE sources localized using NonLinLoc software and applying a layered velocity model. Black crosses: fracture patterns.

The first location analysis (homogeneous velocity model), allowed to identify high-quality events in the whole dataset and their corresponding arrival times: in such a way, sets of seismic phase arrival times for each high-quality event has been created, and they were used as input parameters in the NonLinLoc analisys.

Figure 8.29 shows the hypocenter location of 227 high-quality events recorded during 3 months of testing: red dots are AE sources localized using "least-squares" solution approach, with the homogeneous velocity model (v=5500 m/s); green dots are AE sources localized using NonLinLoc software and applying the layered velocity model described above. The pattern of fractures detected at the end of the test is also plotted (black crosses).

It is possible to observe how the second model better spread the AE sources in X and Y direction, obtaining a central band in the sample where most of the

175
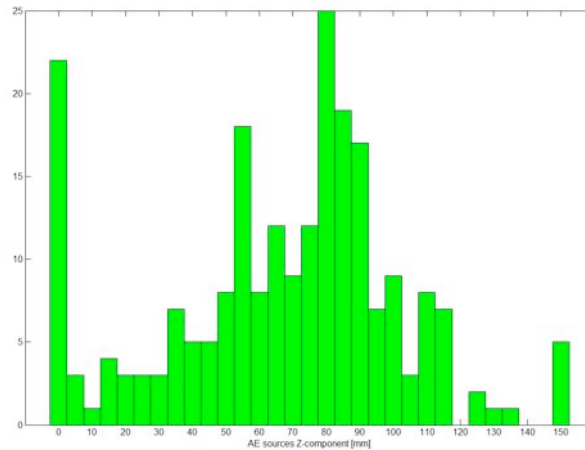
Figure 8.30: Histogram showing that the maximum AE activity is concentrated at 80-90 mm deep (AE source location obtained using NonLinLoc software and applying a layered velocity model).

AE activity is concentrated; further, some hypocenters fit quite well fractures detected. The sources alignment to a particular depth, can be seen also from the histogram in Figure 8.30: the maximum of AE activity is concentrated in the range between 80 and 90 mm deep, in agreement with the presence of fractures at that depth, as can be seen in Figure 8.24.

In order to study the temporal sequence of AE events caused by ice growth occurred during the laboratory test, hypocentres have been plotted for each month: the results are reported in Figure 8.32; histograms in Figure 8.31 shows the AE source Z-component distributions month by month.

During the first month, AE sources were scattered throughout the rock sample volume, probably because the ice formed during freezing induced microcrack propagation, but the mechanisms involved was only volume expansion due to water phase change. During the second month instead, it is possible to observe that the hypocenters started to have some tendency to concentrate in the central part of the gneiss block, and in the last month, some AE sources were aligned to the cracks detected.

Ice segregation mechanism has allowed the migration of liquid water to the frozen fringe and in this way, crack propagation has continued over time, until

176

the onset of macrofractures visible on the outer sample surfaces. Monitoring AE, the persistence of this activity during the test has been observed, identifying a band 40 mm thick (i.e. between 4.5 and 8 cm deep), where hypocenters location tended to concentrate. This layer matches roughly with the frozen fringe, where unidirectional steady heat transfer and water transport, induce fracture propagation by slow-continuous freezing and fixed temperature gradient.

However, even during the last month of testing, some recorded events were scattered and not concentrated only in the cracking band. It is possible to think that the micro-criosuction phenomenon occurs in an area not so precisely identifiable on the basis of theoretical isotherms, which should characterize the thermal regime of the sample, but in a wider area, due to the inhomogeneity of the material. Moreover, the events out of the frozen fringe, might just be of thermo-mechanical nature.

Further work should be also necessary to have a number of precisely localized events, that alone would justify the presence of macro-cracks. During this experimental trial instead, many events induced by micro-fracture propagation have not been recorded, probably because they were below the sensitivity of the AE sensors.

Although requiring these insights, the results seem to confirm the hypothesis that monitoring AE could be an useful complementary tool to study frost-induced deterioration phenomena in rock.
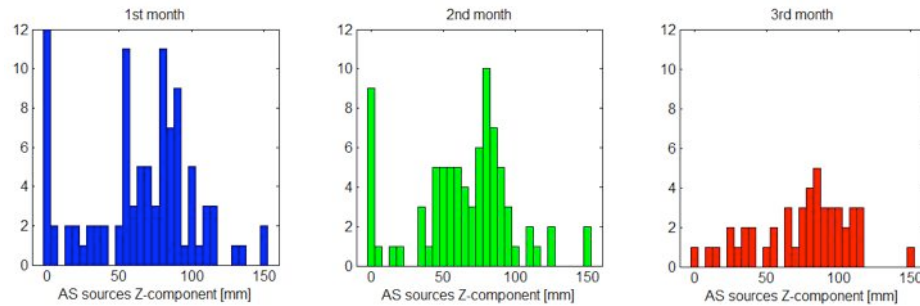
Figure 8.31: Histograms showing AE source Z-component distributions month by month.
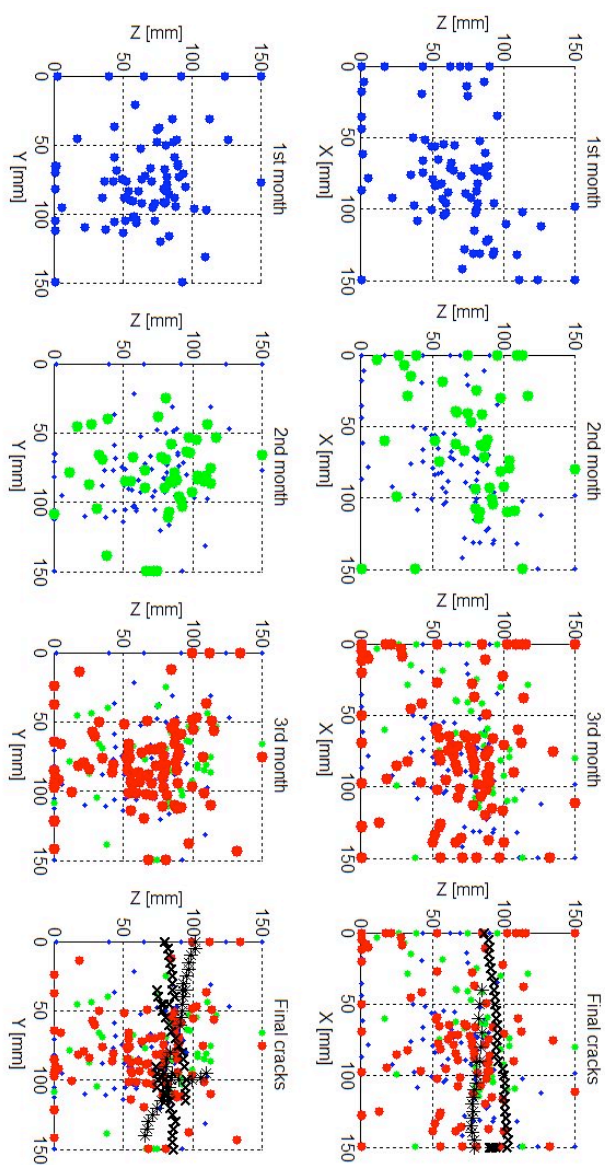
Figure 8.32: Temporal sequence of AE events occured during the laboratory test. Blue dots: first month AE events; green dots: second month AE events; red dots: third month AE events; black crosses: superficial macrocracks.

178

Chapter 9

Conclusions

An increasing number of hazardous rockfalls and rock slides of all magnitudes observed in the Alpine environment during the last decade, is one of the events recognized as consequences of the climate change. Warming can reduce the stability of permafrost in steep areas and thus could increased rock falls. Large events involving rock volumes over 1 million m^3 took place in the Alps during the last decade.

Focusing on the Italian Alpine region, the Matterhorn (4478 m a.s.l., NW Italian Alps), a rock pyramid made of highly fractured gneisses and gabbros, has suffered rock deformation and rock-falls since summer 2003.

The presence of massive ice in the Cheminée rockfall detachment zone, has been interpreted as a signal of ice segregation mechanism involved in high mountain bedrock degradation. Here, a monitoring system composed by geophones and thermometers was installed at the Carrel hut, assuring the possibility of performing crossed analysis between geophysical data and thermal analysis.

A simplified heat-transfer numerical model has been computed, in order to assess if the superficial source location obtained from geophysical monitoring could be correlated to the bedrock thermal regime.

Comparing the two spatial-temporal distributions of temperature and microseismic activites, it has been possible to verify that the geophysical recorded data could be be correlated with thaw and solidification mechanism. The thermal profile obtained from the numerical model showed that the rockwall located at 3829 m a.s.l. experiences seasonal frost/thaw penetration to 2 m in depth, and the microseismic source location has revealed that these

were concentrated in the active layer. In particular, the hypocenters of a selected class of nine events, which may belong to a discontinuity system, seemed to be localized close to the permafrost boundary, a layer characterized by ice-rich fracturated zones and ice-filled cracks.

These results could confirm the hypothesis of ice segregation as a mechanism leading to steep bedrock degradation and its associated instability: this process could contribute to the destabilization of much larger volumes of rock than would expected due to volumetric expansion.

In order to deepen the study of ice segregation phenomenon and resulting crack growth in hard, intact rock, a down scaled physical simulation of this frost weathering mechanism has been designed and set up, to monitor the microfracture activity in rock specimens under fixed temperature gradient; upsizing of physical modeling experiments and monitoring natural unweathered bedrock, would provide valuable insights into permafrost landscape evolution and engineering geology.

Long-term freezing tests have been set up on "Arolla gneiss" cubic shape and fully saturated samples, measuring $15 \times 15 \times 15$ cm: this large size was necessary to provide sufficient depth to permit freezing and thawing of a thin artificial active layer above permafrost.

The role of the premelted water films in lens growth and fracturing mechanism in frozen rock under steady temperature gradients, have been studied through numerical FEM technique, owing to the non-linearity of the governing equations. Models have been developed and implemented with differing degrees of sophistication, in order to validate the experimental procedure as well as to evaluate some predictions.

A series of two-dimensional upward freezing simulations was performed, in order to study the interactions between frozen rock, thermal, hydraulic and mechanical processes. A fully coupled thermo-hydro-mechanical model has been implemented in the FEM code CODE_BRIGHT, trying to predict the approximate depth of maximum cracking for the upward freezing experiment. Observing the computed trend of the liquid water saturation degree, it was possible to recognize a range between -3°C and 0°C, in which considerable amount of water remains unfrozen, although the subfreezing temperature: this layer is defined "frozen fringe". The computed liquid flux has demonstrated how the accumulation of freezing pore water drives the ice segregation process: the unfrozen pore water is drawn into the frozen fringe, and here the flux reaches the maximum value equal to 3.25E-07 Kg $m^{-2}s^{-2}$. Finally it was possible to deduce that freezing at fixed temperature gradient allowed the localization of increasing porosity below the zero-isotherm depth, which should

180

therefore be the preferential place for the ice lenses formation.

This aspect has also been studied performing uncoupled numerical analyses with the FEM code ABAQUS: they highlighted how steady temperature gradients play a fundamental role in crack propagation, resulting tense not only for the volumetric expansion of the ice contained within, but also because of opposite deformations (contraction in the lower, colder part and expansion in the upper warmer part) of the rock matrix that contains the defect. According to the results obtained with the numerical model, the temperature interval that would maximize the frost cracking mechanism in the rock sample, has been chosen: -12°C on the lower surface, +3°C on the upper surface.

Due to the complexity of the phenomena involved, a pilot trial has been necessary in order to test the methodology and to identify the difficulties connected with the application of thermal cycles to a saturated rock sample, monitoring microcrack activities. Experimental laboratory prototype have been modeled and set up, the Arolla gneiss samples have been charaterized and thermally microcracked to be comparable with the material which characterizes the Matterhorn at 3835 m a.s.l.

A sensitive point of the laboratory procedure was to monitor with acoustic emission techniques the microcracks propagation induced by ice growth. As a matter of fact, conventional measures of frost damage do not provide enough information about the magnitude, timing and location of frost-induced deterioration.

Monitoring AE has been considered a suitable investigation tool for studying frost weathering experimentally, because it permits continuous, non destructive determination of the approximate location of microfracture events caused by ice growth in rocks.

In order to obtain an accurate location of AE events, ultrasonic measurements have been carried out in different thermal regime within the sample, obtaining wave velocity values for temperatures above and below the freezing point.

The importance of a correct receiver array distribution has been examined in detail, and an optimum array geometry has been chosen, following a procedure that would minimize source location errors.

Finally two long-term freezing tests have been carried out: the first was aimed to reproduce the ice lens growth mechanism due to the onset of ice segregation processes at the interface active layer-permafrost table, building up a physical model. During three months of testing, microcracks propagated horizontally through the gneiss sample, resulting in a continuous and thick macro-crack near the base of the artificial active layer of the simulated permafrost. The fracture was more or less horizontal, flat and parallel or sub-parallel to the

181

cooling surfaces (i.e. the -2°C isotherm): fractures depth was located in the layer between approximately 2.5 and 6 cm in depth, and the ice-lens growth was inferred within an approximate temperature range of -0.5°C to -2.5°C. Thus, the experimental results provided strong support for the segregation ice model of frost weathering.

During the second trial, acoustic emission monitoring system has been installed, to study the processes operating in evolving fault zone due to the ice lens growth. Localizing recorded events, a 40 mm thick band (i.e. between 4.5 and 8 cm deep) have been identified, where most of the hypocenters were concentrated. This layer matches roughly with the frozen fringe, where unidirectional steady heat transfer and water transport, induce fracture propagation by slow-continuous freezing and fixed temperature gradient.

Although requiring insights, the results seem to confirm the hypothesis that monitoring AE could be an useful complementary tool to study frost-induced deterioration phenomena in rock.

Appendix A

Thermosensors technical specifications

Table A.1: Characteristics of the Pt100 elements used for the temperature measuring.

General specifications	
Type	Wire wound Pt100 element (code578-081)
Maker	TC Direct s.r.l.
Dimensions	15 mm (length) - 1.6 mm (diameter)
Nominal resistance	100 ohms at 0°C, 138.5 ohms at 100°C
Tolerance class	1/5
Temperature range	-200°C to 600°C
Leads	10mm long (resistance value taken at 5mm from sensor)

Table A.2: Thermosensors technical characteristics.

Type	Range	Resolution	High Accuracy	
			90 days	1 year
K	-120°C to 1300°C	0.1	0.01% L + 0.1°C	0.02% L + 0.1°C
T	-100°C to 400°C	0.1	0.01% L + 0.2°C	0.02% L + 0.2°C
J	-120°C to 1100°C	0.1	0.01% L + 0.1°C	0.02% L + 0.1°C
S	550°C to 1768°C	0.5	0.01% L + 0.5°C	0.02% L + 0.5°C
B	900°C to 1820°C	0.5	0.01% L + 0.5°C	0.02% L + 0.5°C
N	0°C to 1300°C	0.1	0.01% L + 0.2°C	0.2% L + 0.2°C
E	-250°C to 1000°C	0.1	0.01% L + 0.2°C	0.2% L + 0.1°C
C	-20°C to 2320°C	0.2	0.01% L + 0.4°C	0.2% L + 0.4°C
R	550°C to 1768°C	0.5	0.01% L + 0.5°C	0.2% L + 0.5°C
L	-200°C to 900°C	0.1	0.01% L + 0.2°C	0.2% L + 0.2°C
PI	-100°C to 1400°C	0.1	0.01% L + 0.3°C	0.2% L + 0.3°C

Thermocouples

With the built-in CJC, add 0.5°C uncertainty

Appendix B

Acquisition board technical characteristics for temperature monitoring

Table B.1: Characteristics of PC10 acquisition board for temperature monitoring.

General specifications	
Type	PC10
Maker	AOIP
Dimensions	$330 \times 170 \times 38$ mm
Weight	950 g
Power supply	9-48 V
Communication	RS232, RS485, Ethernet
Operating conditions	-10 to 50°C; 10-80% HR w/o condensation
Configuration-data processing	software LTC10
Real time monitoring-traceability	software VISULOG TM
Options	Built in radio modem (wireless application)
Accuracy: high	Speed: 14 meas/s - Resolution 700000 cts
Accuracy: medium	Speed: 100 meas/s - Resolution 70000 cts
Accuracy: low	Speed: 250 meas/s - Resolution 7000 cts

Table B.2: Characteristics of PC10 acquisition board for temperature monitoring.

Technical specifications (+23 °C / - 5 °C)

10 to 30 universal inputs; 2 relay inputs; removable screening connector;
modbus, ethernet interfaces; 100000 data memory; generating e-mails when alarms appear;
configuration and data processing software LTC10; real time monitoring and traceability software: VISULOG

DC Voltage accuracy

Range [mV]	High		Medium		Low
	90 days	1 year	90 days	1 year	1 year
50	0.01% + 5µV	0.02% + 7µV	0.05% + 20µV	0.1% + 22µV	0.20% + 45µV
500	0.01% + 5µV	0.02% + 7µV	0.05% + 20µV	0.1% + 22µV	0.2% + 205µV
5000	0.01% + 0.5mV	0.02% + 0.7mV	0.05% + 2mV	0.1% +7 mV	0.20% + 15mV
50*10³	0.01% + 0.5mV	0.02% + 0.7mV	0.05% + 2mV	0.1% + 7mV	0.20% + 25mV
10*10⁴	0.01% + 5mV	0.02% + 7mV	0.05% + 20mV	0.1% + 22mV	0.20% + 205mV

Maximum voltage between channels: 150 V

DC Current accuracy

Range [mA]	High		Medium		Low
	90 days	1 year	90 days	1 year	1 year
20	0.01% + 10µA	0.02% + 20µA	0.05% + 40µA	0.1% + 60µA	0.20% + 40µA

The use of 50 Ohm (0.1%) shunt per channel is necessary

186

Table B.3: Characteristics of PC10 acquisition board for temperature monitoring.

Resistance accuracy

Range [$k\Omega$]	High		Medium		Low	
	90 days	1 year	90 days	1 year	90 days	1 year
0.1	$0.02\% + 5m\Omega$	$0.04\% + 7m\Omega$	$0.05\% + 50m\Omega$	$0.07\% + 70m\Omega$	$0.2\% + 500m\Omega$	$0.40\% + 700m\Omega$
1	$0.02\% + 50m\Omega$	$0.04\% + 70m\Omega$	$0.05\% + 500m\Omega$	$0.07\% + 700m\Omega$	$0.2\% + 2\Omega$	$0.40\% + 5\Omega$
3	$0.02\% + 500m\Omega$	$0.04\% + 700m\Omega$	$0.05\% + 5\Omega$	$0.07\% + 7\Omega$	$0.2\% + 5\Omega$	$0.40\% + 7\Omega$
100	$0.02\% + 5\Omega$	$0.04\% + 7\Omega$	$0.05\% + 50\Omega$	$0.07\% + 70\Omega$	$0.2\% + 200\Omega$	$0.40\% + 500\Omega$
200	$1\% + 10\Omega$	$2\% + 50\Omega$	$2\% + 100\Omega$	$4\% + 200\Omega$	$4\% + 1k\Omega$	$5\% + 1.5k\Omega$

Add 5 $m\Omega$ for a three wires configuration and 50 $m\Omega$ for a two wires configuration

RTD's specifications for a 4 wires configuration

Range	High		Medium		Low	
	90 days	1 year	90 days	1 year	90 days	1 year
Pt 100	$0.02\% + 0.03°C$	$0.04\% + 0.05°C$	$0.05\% + 0.1°C$	$0.07\% + 0.2°C$	$0.2\% + 1°C$	$0.40\% + 1°C$
Pt 1000	$0.02\% + 0.3°C$	$0.04\% + 0.5°C$	$0.05\% + 0.5°C$	$0.07\% + 0.2°C$	$0.1\% + 1°C$	$0.40\% + 1°C$
Ni 100	$0.02\% + 0.03°C$	$0.04\% + 0.05°C$	$0.05\% + 0.1°C$	$0.07\% + 0.2°C$	$0.2\% + 1°C$	$0.40\% + 1°C$
Cu 10	$0.02\% + 0.3°C$	$0.04\% + 0.5°C$	$0.05\% + 0.5°C$	$0.07\% + 1°C$	$0.2\% + 1°C$	$0.40\% + 1°C$

Appendix C

Cooling plate general specifications

Cooling plate general specifications	
Weight [kg]	4.2
TE Power (typical)	24 VDC at 9.2 A
TE Power (maximum)	24 VDC at 11.1 A
Hot-side Fan Power (total)	24 VDC at 0.46 A

Table C.1: Characteristics of the cooling plate. TE Power (typical): current is rated at $+25°$C ambient, $+25°$C cold plate, maximum heat removal. At $-23°$C cold plate, the typical current is 8.9 A; TE Power (maximum): current, at steady-state operation under-worst case conditions, is rated at $-12°$C ambient, $+70°$C cold plate, maximum heat removal.

Appendix D

AE sensor characteristics

Table D.1: AE sensor characteristics

General specifications	
Sensor type	NANO30
Maker	Euro Physical Acoustics SA
Sensor S/N	FN54 - FN61
Dimensions (diameter × height)	8 × 8 mm
Weight	8 g
Operating temperature	-65°C to 177°C
Shock limit	10000 g
Case material	Stainless steel
Face material	Ceramic
Connector type	BNC
Connection location	Side
Peak sensitivity	62 dB (ref. 1V/(ms))
Operating frequency range	125 - 720 kHz
Resonant frequency	140 kHz
Directionality	±1.5 dB
Seal type	Epoxy

Operating specifications	
Dynamic	
Peak Sensitivity, Ref $[V/(m/s)]$	62 dB
Peak Sensitivity, Ref $[V/\mu bar]$	-72 dB
Operating Frequency Range	125 - 750 kHz
Resonant Frequency, Ref $[V/(m/s)]$	140 kHz
Resonant Frequency, Ref $[V/\mu bar]$	300 kHz
Directionality	$+/-$ 1.5 dB
Environmental	
Temperature Range	-65 to 177°C
Shock Limit	500 g
Completely enclosed crystal for RFI/EMI immunity	
Physical	
Dimensions	0.3"OD X 0.3"H
	8 mm OD X 8 mm H
Weight	2 grams (8 with cable and connector)
Case Material	Stainless steel
Face Material	Ceramic
Connector	BNC
Connector Locations	Side

Table D.2: Operating specifications of the AE sensors.

Appendix E

Technical specifications of GL-1000 AE acquisition board
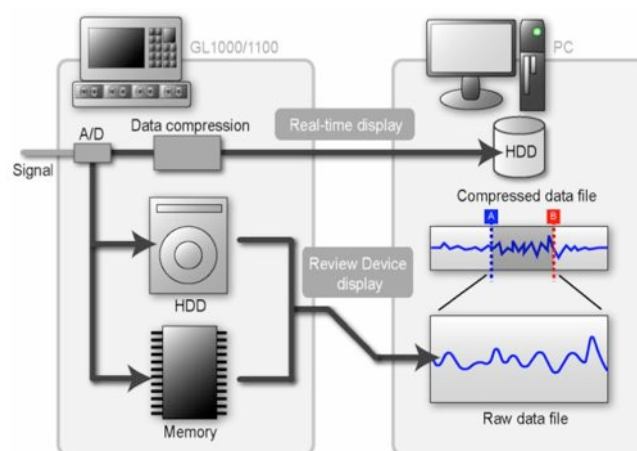
Figure E.1: General scheme of the functionality of the AEs' acquisition board (revised from the Graphtec user's manual).

GL-1000 AEs acquisition board basic specifications	
Analog input	Number of slots 8-channel model: 4
Logic input	Number of slots: 1 8 channels/unit (option)
PC interface	LAN, USB
Memory capacity	512 kword per channel
Internal memory	40 GB 2.5-inch hard disk
Isolation voltage	Between the AC power supply and casing: 1 minute at 1,500 V AC
Insulation resistance	Between the AC power supply and casing: 20 MΩ at 500 V DC
Operating environment	0°C to 40°C
Operating noise levels	Standby: 60 dBA maximum
Rated power supply	AC adapter (100 V to 240 V AC)
Power consumption	8-channel: approx. 90 VA
External dimensions	8-channel: 300mm(W)×222mm(D)×57mm(H)
Weight (approximate)	8-channel: 2.4 kg

Table E.1: Basic specifications of the GL-1000 AEs acquisition board (8 channels model), revised from the Graphtec user's manual.

Appendix F

Preamplifiers

Figure F.1: Specifically designed and manufactured preamplifiers: a) amplifier circuit; b) shielding cases; c) power supply; d) connection between sensors-amplifiers and acquisition board (on the right).

C1=C4 = 10 pF

C2=C5 = 100 nF

C3=C6 = 100uF 63V

R1=R2 = 1MOhm NON IND

R3 = 511 Ohm 1%

R4 = 50 Ohm NON IND

C7 = 10uF 50V Non POL.

BR1 = WL02

IC1 = INA 111 ONLY MILTARY

GRADE
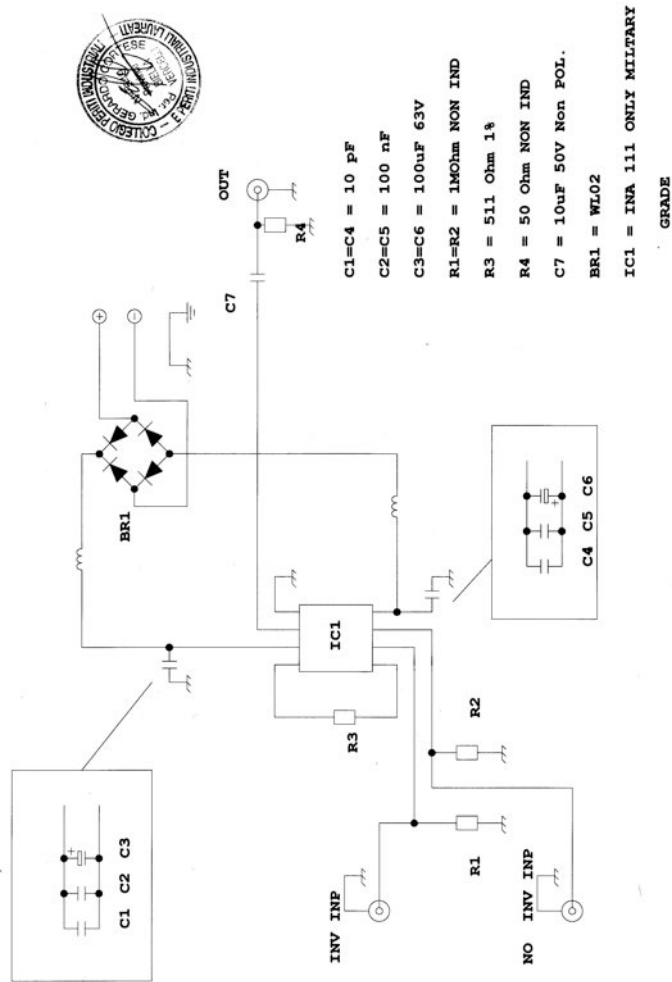
Figure F.2: Preamplifiers circuit diagram.

196

Appendix G

AE sensor calibration certificates

Table G.1: AE sensor peak frequencies.

NANO-30 peak frequencies	
Channel	Peak Frequency [kHz]
Ch1	249.02
Ch2	195.31
Ch3	268.55
Ch4	229.49
Ch5	224.51
Ch6	200.20
Ch7	214.84
Ch8	253.91

198
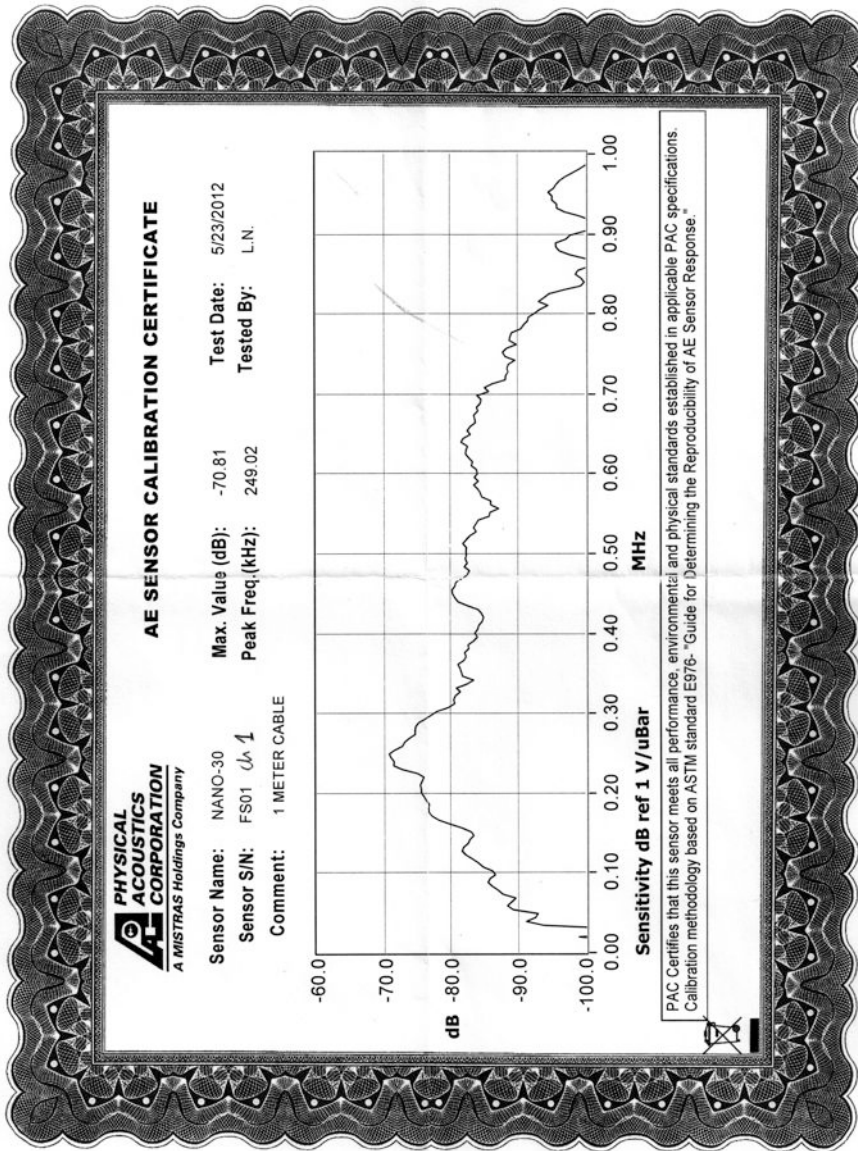
Figure G.1: AE sensor calibration certificate (CH 1).

Bibliography

[1] ABAQUS User's Manual, 2011.

[2] Alvaro A. O. - Automatic picking and classification of acoustic emission event arrivals, Ph.D. Thesis, University of Oklahoma, Oklahoma, 2010.

[3] Akagawa S., Fukuda M. - Frost heave mechanism in welded tuff, Permafrost and Periglacial Processes, 2: 301-309, 1991.

[4] Akagawa S., Nishisato K. - Tensile strength of frozen soil in the temperature range of the frozen fringe, Cold Regions Science and Technology, 57: 13-22, 2009.

[5] Amitrano D. - Rupture by damage accumulation in rocks, International Journal of Fracture, 139: 369-381, 2006.

[6] Amitrano D., Arattano M., Chiarle M., Mortara G., Occhiena C., Pirulli, M. Scavia, C. - Microseismic activity analysis for the study of the rupture mechanisms in unstable rock masses, Natural Hazards and Earth System Science, 10 (4): 831-841, 2010.

[7] Amitrano D., Hantz D. - Acoustic emission of jointed and intact rocks during triaxial compression test, International Conference on. Mechanics of Jointed and Faulted Rock, Rossmanith, 375-380, Balkema, Vienna, 1998.

[8] Anant S.K., Dowla F.U. - Wavelet transform methods for phase identification in three-component seismogram, Bulletin of the Seismological Society of America, 87: 1598-1612, 1997.

[9] Andren A. - Degradation of rock and shotcrete due to ice pressure and frost shattering, Research report, Lulea University of Technology, 2006.

[10] Andersland O.B, Ladanyi B. - Frozen ground engineering, The American Society of Civil Engineers and John Wiley & Sons, Hoboken, New Jersey, 2004.

[11] Arenson L.U. - Unstable alpine permafrost: a potentially important natural hazard-variations of geotechnical behaviour with time and temperature, Ph.D. Thesis, Swiss Federal Institute of Technology, Zurich, 2002.

[12] Baer M., Kradolfer U. - An automatic phase picker for local and teleseismic events, Bulletin of the Seismological Society of America, 77: 1437-1445, 1987.

[13] Bellopede R. - La misura della velocitá dell'impulso ultrasonico nella diagnostica e nel monitoraggio dello stato di conservazione delle pietre naturali, Ph.D. Thesis, Politecnico di Torino, Italy, 2005.

[14] Beniston M. - The 2003 heat wave in Europe. A shape of things to come? Geophysical Research Letters, 31, L02022, 2004.

[15] Beniston M. - Climatic change in mountain regions: a review of possible impacts, Climatic Change, 59: 5-31, 2003.

[16] Black P. B., Tice A. R. - Comparison of soil freezing curve and soil water curve data for Windsor Sandy Loam, Water Resources Research, 25 (10): 2205-2210, 1989.

[17] Bonifaz E.A. - Cohesive zone modeling to predict failure processes, Canadian Journal on Mechanical Sciences & Engineering, 2 (3), 2011.

[18] Bonner J. L., Leidig M. R., Sammis C., Martin R. J. - Explosion Coupling in Frozen and Unfrozen Rock: Experimental Data Collection and Analysis, Bulletin of the Seismological Society of America, 99: 830-851, 2009.

[19] Borgesson L., Hernelind J. - Coupled thermal-hydro-mechanical calculations of the water saturation phase of a KBS-3 deposition hole. Influence of hydraulic rock properties on the water saturation phase, SKB report TR-99-41, Stockholm, 1999.

[20] Bost M. - Altération par le gel des massifs rocheux : etude expérimentale et modlisation des mécanismes de génération des contraintes dans les fissures, Ph.D. Thesis, Ecole Nationale des Ponts et Chaussée, 2008.

[21] Bjornson J., Lauriol B. - Microgelivation versus macrogelivation: towards bridging the gap between laboratory and field frost weathering, Permafrost and Periglacial Processes, 12 (3): 299-313, 2001.

[22] Brown R.J.E., Kupsch W.O. - Permafrost terminology, Associate Committee on Geotechnical Research, Technical Mem., n.111, N.R.C.C., Ottawa, 1974.

[23] Brunetti M., Maugeri M., Monti F., Nanni T. - Temperature and precipitation variability in Italy in the last two centuries from homogenised time series, International Journal of Climatology, 26: 345-381, 2006.

[24] Burn C., Smith C. - Observation of the "thermal offset" in near-surface mean annual ground temperatures at several sites, Artic, 41: 99-104, 1988.

[25] Cengel Y. A. - Heat transfer: a practical approach, University of Nevada-Reno, McGraw-Hill Higher Education, 2003.

[26] CENSICRO - PERMAdataROC - Approfondamenti sulla ricerca degli elementi caratterizzanti le aree soggette a crolli in alta montanga. Relazione finale, 2009.

[27] Cerutti A. - Dalla Piccola Etá Glaciale all'attuale. Musumeci Editore, Aosta, 2006.

[28] Chaki S., Takarli M., and Agbodjan W.P. - Influence of thermal damage on physical properties of a granite rock: porosity, permeability and ultrasonic wave evolutions, Construction and Building Materials, 22 (7): 456-1461, 2008.

[29] Chen T.C., Yeung M.R., Mori N. - Effect of water saturation on deterioration of welded tuff due to freeze-thaw action, Cold Regions Science and Technology, 38: 127-136, 2003.

[30] Côté J., Konrad J.M. - A generalized thermal conductivity model for soils and construction materials, Canadian Geotechnical Journal, 42: 443-458, 2005.

[31] Coussy, O. - Poromechanics of freezing materials, Journal of the Mechanics and Physics of Solids, 53 (8): 1689-1718, 2005.

201

[32] Davies M.C.R., Hamza O., Harris C. - The effect of rise in mean annual temperature on the stability of rock slopes containing ice-filled discontinuities, Permafrost and Periglacial Processes, 12: 137-144, 2001.

[33] Daubechies I. - The wavelet transform, time-frequency localization and signal processing, IEEE Transactions on Informormation Theory, 36: 961-1005, 1990.

[34] Deline P. - Recent Brenva rock avalanches (Valley of Aosta): new chapter in an old story? Supplementi di Geografia Fisica e Dinamica Quaternaria, 5: 55-63, 2001.

[35] Deline P., Jaillet S., Rabatel A., Ravanel L. - Ground-based LiDAR data on permafrost-related rock fall activity in the Mont-Blanc massif, Proceedings of the 9th International Conference on Permafrost 2008, Institute of Northern Engineering, University of Alaska, Fairbanks, 349-354, 2008.

[36] Dong Y., Lai Y., LI J., Yang Y. - Laboratory investigation on the cooling effect of crushed-rock interlayer embankment with ventilated ducts in permafrost regions, Cold Regions Science and Technology, 61: 136-142, 2010.

[37] Draebing D., Krautblatter M. - P-wave velocity changes in freezing hard low-porosity rocks: a laboratory-based time-average model, The Cryosphere Discussions, 6: 793-819, 2012

[38] Dyke L D. - Frost heaving of bedrock in permafrost regions, Bulletin of Engineering Geology and the Environment, 21: 389-405, 1984.

[39] Dzhurik V., Leshchikov F. N. - Experimental investigations of seismic properties of frozen soils, 2nd International Conference on Permafrost, USSR Contribution, Yakutsk, USSR, 485-488, 1973.

[40] Feih S. - Development of a user element in ABAQUS for modelling of cohesive laws in composite structures, Risø-R Report 1501(EN), RisøNational Laboratory Roskilde, Denmark, 2005.

[41] Fish A., Zaretsky Y. - Ice strength as a function of hydrostatic pressure and temperature, Cold Regions Research and Engineering Laboratory, Hanover N.H., 1997.

[42] Fish J., Belytschko T. - A first course in finite elements, John Wiley & Sons, Chichester, England, 2007.

[43] Fredlund D.G., Xing A. - Equations for the soil-water characteristic curve, Canadian Geotechnical Journal, 31 (4): 521-532, 1994.

[44] French H.M. - Active layer processes, Advances in Periglacial Processes, John Wiley & Sons, Chichester, England, 1988.

[45] Fischer L., Huggel C. - Methodical design for stability assessments of permafrost-affected high-mountain rock walls, Ninth International Conference on Permafrost, 439-444, 2008.

[46] Fischer L., Amann F., Moore J.R., Huggel C. - Assessment of periglacial slope stability for the 1988 Tschierva rock avalanche (Piz Morteratsch, Switzerland), Engineering Geology, 116: 32-43, 2010.

[47] Gassmann F. - Elasticity of porous media. Uber die elastizitat poroser medien: Vierteljahrsschrift der Naturforschenden Gesselschaft, 96: 1-23, 1951.

[48] Ge M., Hardy H. R. - The mechanism of array geometry in the control of AE/MS source location accuracy, Proceedings 29th U.S. Symposium on Rock Mechanics, Minneapolis, MN, A.A. Balkema, Rotterdam, 343-348, 1988.

[49] Ge M., Mottahed P. - An automated AE/MS source location technique used by Canadian mining industry, Proceedings 12th International Acoustic Emission Symposium, Sappora, Japan, Japanese Society for Nondestructive Inspection, Tokyo, 101-118, 1994.

[50] Gens A., Garcia-Molina A. J., Olivella S., Alonso E. E., Huertas F. - Analysis of a full scale in situ test simulating repository conditions, International Journal for Numerical and Analytical Methods in Geomechanics, 22 (7): 515-548, 1998.

[51] Golub G., KahanW. - Calculating the singular values and pseudo-inverse of a matrix, Journal of the Society for Industrial and Applied Mathematics - Series B: Numerical Analysis, 2: 205-224, 1965.

[52] Grant S. A., Sletten R. S. - Calculating capillary pressures in frozen and ice-free soils below the melting temperature, Environmental Geology, 42 (2-3): 130-136, 2002.

[53] Gruber S. - Mountain permafrost: transient spatial modelling, model verification and the use of remote sensing, Ph. D. Thesis, Universität Zürich, 2005.

[54] Gruber S., King L., Kohl T., Herz T., Haeberli W., Hoelzle M. - Interpretation of geothermal profiles perturbed by topography: the alpine permafrost boreholes at Stockhorn plateau, Switzerland, Permafrost and Periglacial Processes 15: 349-357, 2004.

[55] Gruber S., Haeberli W. - Permafrost in steep bedrock slopes and its temperature related destabilization following climate change, Journal of Geophysical Research, 112, 2007.

[56] Gruber S., Hoetzle M., Haeberli W. - Permafrost thaw and destabilization of alpine rock walls in the hot summer of 2003, Geophysical Research Letters, 2004.

[57] Guglielmin M. - Il permafrost alpino (concetti, morfologia e metodi di individuazione), Quaderni di Geodinamica Alpina e Quaternaria, Milano, 1997.

[58] Guglielmin M. - Observations on permafrost round thermal regimes from Antarctica and the Italian Alps, and their relevance to global climate change, Global and Planetary change, 2004.

[59] Guglielmin M. - Il permafrost nelle alpi Italiane e la stabilitá dei versanti, Terra Glacialis, Annuali di Cultura Glaciologica (Anno IX), Servizio glaciologico Lombardo, Milano, 2006.

[60] Gunzel F.K. - Shear Strength of Ice-Filled Rock Joints, Ninth International Conference on Permafrost, 581-586, 2008.

[61] Haeberli W., Wegmann M., von der Mühll D. - Slope stability problems related to glacier shrinkage and permafrost degradation in the Alps, Eclogae Geologicae Helvetiae, 90: 407-414, 1997.

[62] Hales T. C., Roering J. - Climatic controls on frost cracking and implications for the evolution of bedrock landscapes, Journal of Geophysical, 112, 2007.

[63] Hallet B., Walder J. S., Stubbs C. W. - Weathering by segregation ice growth in microcracks at sustained subzero temperatures: Verification

from an experimental study using acoustic emissions, Permafrost and Periglacial Processes, 2: 283-300, 1991.

[64] Hardy H. R. - Acoustic emission/microseismic activity - Principles, Techniques and Geotechnical Applications, A. A. Balkema, Lisse, The Netherlands, 2003.

[65] Harris C., Davies M.C.R., Etzelmuller B. - The assessment of potential geotechnical hazards associated with mountain permafrost in a warming global climate, Permafrost and Periglacial Processes, 12: 145-156, 2001.

[66] Harris C., Kern-Luetschg M., Murton J., Font M., Davies M., Smith F. - Solifluction processes on permafrost and non-permafrost slopes: results of a large-scale laboratory simulation, Permafrost and Periglacial Processes 19: 359-378, 2009.

[67] Harris C., Vonder Muhll D., IsakseN K., Haeberli W., Sollid J., King L., Holmlund P., Dramis F., Guglielmin M., Palacios D. - Warming permafrost in European mountains, Global and Planetary Change, 39: 215-225, 2003.

[68] IPCC - Climate change 2007, 4th Assessment Report. Working Group I - Report "The Physical Science Basis", 2007.

[69] Jones G.A., Nippress S.E.J., Rietbrock A., Reyes-Montes J.M. - Accurate Location of Synthetic Acoustic Emissions and Location Sensitivity to Relocation Methods, Velocity Perturbations, and Seismic Anisotropy, Pure and Applied Geophysics, 65: 235-254, 2008.

[70] Jurkewicz A. - Polarization analysis of three-component array data, Bulletin of the Seismological Society of America, 78 (5): 1725-1743, 1988.

[71] Kaab A., Frauenfelder R., Roer I. - On the response of rock-glacier creep to surface temperature increase, Global and Planetary Change, 56: 172-187, 2007.

[72] Kahraman S. - The correlations between the saturated and dry P-wave velocity of rocks, Ultrasonics 46: 341-348, 2007.

[73] King M. S. - Acoustic velocities and electrical properties of frozen sandstones and shales, Canadian Journal of Earth Sciences, 14: 1004-1013, 1977.

[74] King M. S., Zimmermann R. W., Corwin R. F. - Seismic and electrical properties of unconsolidated permafrost, Geophysical Prospecting, 36: 349-364, 1988.

[75] King M. S., Pettitt W. S., Haycox J. R., Young R. P. - Acoustic emissions associated with the formation of fracture sets in sandstone under polyaxial stress conditions, Geophysical Prospecting, 60 (1): 93-102, 2011.

[76] Kitagawa G., Akaike H., A procedure for the modeling of non- stationary time series, Annals of the Institute of Statistical Mathematics, 30: 351-363, 1978.

[77] Kohl T., Signorelli S., Rybacj L. - Three-dimensional (3-D) thermal investigation below high alpine topography, Physics of the Earth and Planetary Interiors, 126: 195-210, 2001.

[78] Koopmans R. W. R., Miller R. D. - Soil freezing and soil water characteristics curves, Soil Science Society of America Journal, 30 (6): 680-685, 1996.

[79] Krautblatter M. - Detection and quantification or permafrost change in alpine rock walls and implication for rock instability, Ph. D. Thesis, Universität Bonn, 2009.

[80] Krautblatter M., Verleysdonk S., Flores-Orozco A., Kemna A. - Temperature calibrated imaging of seasonal changes in permafrost rock walls by quantitative electrical resistivity tomography (Zugspitze, German/Austrian Alps), Journal of Geophysical Research-Earth Surface 115, F02003, 2010.

[81] Krautblatter M., Funk D., Günzel F.K. - Why permafrost rocks become unstable: a rock-icemechanical model in time and space, Earth Surface Processes and Landforms, for Peer Review.

[82] Kukkonen I.T., Safanda J. - Numerical modelling of permafrost in bedrock in northern Fennoscandia during the Holocene, Global and Planetary Change, 29: 259-273, 2001.

[83] Kurz J.H., Grosse C.U., Reinhardt H.W. - Strategies for reliable automatic onset time picking of acoustic emissions and of ultrasound signals in concrete, Ultrasonics, 43: 538-546, 2005.

[84] Lautrido, J. P., Letavernier G., Linde, K., Etlicher B., Ozouf J. C. - Porosity and frost susceptibility of flints and chalk: laboratory experiments, comparison of glacial and periglacial surface texture of flint material, and field investigations, Proceedings of the 4th International Flint Symposium, Cambridge University Press, Cambridge, 269-282, 1987.

[85] Lockner D.A. - The role of acoustic emission in the study of rock fracture, International Journal of Rock Mechanics and Mining Science Geomechanics Abstracts, 30 (7): 883-899, 1993.

[86] Lomax A. - A Reanalysis of the Hypocentral Location and Related Observations for the Great 1906 California Earthquake, Bulletin of the Seismological Society of America, 95: 861-877, 2005.

[87] Lomax A., Virieux J., Volant P., Berge C. - Probabilistic earthquake location in 3D and layered models: Introduction of a Metropolis-Gibbs method and comparison with linear locations, in: Advances in Seismic Event Location Thurber, C.H., and N. Rabinowitz (eds.), Kluwer, Amsterdam, 101-134, 2000.

[88] Lunardini V.J. - Heat Transfer in Cold Climates, Van Nostrand Reinhold Company, Toronto, 1981.

[89] Matsuoka N. - The rate of bedrock weathering by frost action: field measurements and a predictive model, Earth Surf. Process, Landforms, 15: 73-90, 1990.

[90] Matsuoka N. - Mechanisms of Rock Breakdown by Frost Action - an Experimental Approach, Cold Regions Science and Technology, 17: 253-270, 1990.

[91] Matsuoka N. - A model rate of frost shattering: application to field data for Japan, Svalbard and Antarctica, Permafrost Periglacial Processes, 2: 271-281, 1991.

[92] Matsuoka N. - Microgelivation versus macrogelivation: towards bridging the gap between laboratory and field frost weathering, Permafrost Periglacial Processes, 12: 299-313, 2001.

[93] Matsuoka N., Murton J. - Frost weathering: recent advances and future directions, Permafrost Periglacial Processes, 19: 195-210, 2008.

[94] Matsuoka N., Sakai H. - Rockfall activity from an alpine cliff during thawing periods, Geomorphology, 28: 309-328, 1999.

[95] Mavko G., Mukerji T., Dvorkin J. - Rock physics handbook: Tools for seismic analysis in porous media: Cambridge University Press, 1998.

[96] Mellor M. - Phase composition of pore water in cold rocks, CRREL Res. Rep. 292, U.S. Army Corps of Engineers, Hanover, N. H., 1970.

[97] Miller R. D. - Frost heaving in non-colloidal soils, Proceedings of the 3rd International Conference on Permafrost, Edmonton, 708-713, 1978.

[98] Mottaghy D., Rath. V. - Latent heat effects in subsurface heat transport modelling and their impact on palaeotemperature reconstructions, Geophysical Journal International, 164: 236-245, 2006.

[99] Murton J. B. - Near-surface brecciation of chalk, isle of thanet, south-east England: a comparison with ice-rich brecciated bedrocks in Canada and Spitsbergen, Permafrost Periglacial Processes, 7: 153-164, 1996.

[100] Murton J.B., Coutard J.P., Lautridou J.P., Ozouf J.C., Robinson D.A., Williams R.B.G. - Physical modelling of bedrock brecciation by ice segregation in permafrost, Permafrost Periglacial Processes, 12: 255-266, 2001.

[101] Murton J.B., Coutard J.P., Lautridou J.P., Ozouf J.C., Robinson D.A., Williams R.B.G., Guillemet G., Simmons P. - Experimental design for a pilot study on bedrock weathering near the permafrost table, Earth Surface Processes and Landforms, 25: 128-1294, 2000.

[102] Murton J.B., Peterson R., Ozouf J.C. - Bedrock Fracture by Ice Segregation in Cold Regions, Science, 314 (5802): 1127-1129, 2006.

[103] Nelson P.A., Yoon S.H. - Estimation of acoustic source strength by inverse methods: part I, conditioning of the inverse problem, Journal of Sound and Vibration, 233 (4): 643-668, 2000.

[104] Nishimura S., Gens A., Olivella S., Jardine R.J. - THM-coupled finite element analysis of frozen soil: formulation and application, Géotechnique, 59 (3): 159-171, 2009.

[105] Noetzli J. - Transient three-dimensional temperature fields in mountain permafrost, Ph.D. Thesis, Universität Zürich, 2008.

208

[106] Noetzli J., Gruber S. - Transient thermal effects in Alpine permafrost, The Cryosphere, 3: 85-99, 2009.

[107] Noetzli J., Gruber S., Friedel S. - Modeling transient permafrost temperatures below steep alpine topography, Excerpt from the Proceedings of the COMSOL Users Conference, Grenoble, 2007.

[108] Noetzli J., Gruber S., Kohl T., Salzmann N., Haeberli W. - Three-dimensional distribution and evolution of permafrost temperatures in idealized high-mountain topography, Journal of Geophysical Research, 112, 2007.

[109] Noetzli J., Hoelzle M., Haeberli W. - Mountain permafrost and recent Alpine rock-fall events: a GIS-based approach to determine critical factors, Proceedings of the 8th International Conference on Permafrost, Zürich, Switzerland, 827-832, 2003.

[110] Nur A., Simmons G. - The effect of saturation on velocity in low porosity rocks, Earth and Planetary Science Letters, 7: 183-193, 1969.

[111] Occhiena C. - Microseismic activity in rock masses: identification, analysis and interpretation, Ph.D. Thesis, Politecnico di Torino, Italy, 2011.

[112] Olivella S., Carrera J., Gens A., Alonso E. E. - Nonisothermal multiphase flow of brine and gas through saline media, Transport in Porous Media, 15 (3): 271-293, 1994.

[113] Olivella S., Gens A., Carrera J., Alonso E. E. - Numerical formulation for a simulator CODE_BRIGHT for the coupled analysis of saline media, Engineering Computations, 13 (7): 87-112, 1996.

[114] Ondrasina L., Kirchner D., Siegesmund S. - Freeze-thaw cycles and their influence on marble deterioration: a long-term experiment, Geological Society of London, Special Publications, 205: 9-18, 2002.

[115] Pandit B. I., King, M. S. - A study of the effects of pore-water salinity on some physical properties of sedimentary rocks at permafrost temperatures, Canadian Journal of Earth Sciences, 16: 1566-1580, 1979.

[116] Pearson C., Murphy J., Hermes R. - Acoustic and Resistivity Measurements on Rock Samples Containing Tetrahydrofuran Hydrates - Laboratory Analogs to Natural-Gas Hydrate Deposits, Journal of Geophysical Research: Solid Earth, 91: 14132-14138, 1986.

[117] Pelfini M., Vanuzzo C. - Assessing area and volume changes from deglaciated areas, Valle d'Aosta, Italy, Annals of Glaciology, 28: 129-134, 1999.

[118] Peterson M. - A method for increased accuracy of the measurement of relative phase velocity, Ultrasonics, 35: 17-29, 1997.

[119] Prick A. - The critical degree of saturation as a threshold moisture level in frost weathering of limestones, Permafrost Periglacial Processes, 8: 91-99, 1997.

[120] Prosser W.H., Gorman M.R., Dorighi J. - Extensional and Flexural Waves in a Thin-Walled Graphite/Epoxy Tube, Journal of Composite Materials, 26 (14): 2016-2027, 1994.

[121] Ravanel L., Allignol F., Deline P., Gruber S., Ravello M. - Rock falls in the Mont Blanc Massif in 2007 and 2008, Landslides, 7:493-501, 2010.

[122] Ravanel L., Deline P. - Climate influence on rockfalls in high-Alpine steep rockwalls: The north side of the Aiguilles de Chamonix (Mont Blanc massif) since the end of the 'Little Ice Age', The Holocene, 21(2) 357-365, 2012.

[123] Remy J. M., Bellanger M., Homandetienne, F. - Laboratory Velocities and Attenuation of P-Waves in Limestones During Freeze-Thaw Cycles, Geophysics, 59: 245-251, 1994.

[124] Roberts T.M., Talebzadeh M. - Acoustic emission monitoring of fatigue crack propagation, Journal of Constructional Steel Research, 59: 695-712, 2003.

[125] Romanovsky V., Osterkamp T. - Interannual variations of the thermal regime of the active layer and near surface permafrost in northern Alaska, Permafrost Periglacial Processes, 6: 313-335, 1995.

[126] Rotonda T. - Influenza della microfessurazione termica sulle caratteristiche di deformabilitá e resistenza delle rocce, Ph. D. Thesis, Universitá La Sapienza, Roma, 1991.

[127] Ryzhkin I.A., Petrenko V.F. - Physical mechanism responsible for ice adhesion, The Journal of Physical Chemistry B, 101: 6267-6270, 1997.

[128] Saad A., Guedon S., Martineau F. - Microstructural weathering of sedimentary rocks by freeze-thaw cycles. Experimental study of state and transfer parameters, Comptes Rendus Geoscience, 342: 197-203, 2010.

[129] Salsa S. - Partial Differential Equations in action. From modelling to theory, Springer-Verlag Italia, Milano, 2008.

[130] Salzmann N., Noetzli J., Gruber S., Hauck C., Hoelzle M., Haeberli W. - Ground surface temperature scenarios in complex high-mountain topography based on regional climate model results, Journal of Geophysical Research, vol. 112, 2007.

[131] Sancho J.M., Planas J., Cendón D.A., Reyes E., Gálvez J.C. - An embedded crack model for finite element analysis of concrete fracture, Engineering Fracture Mechanics, 74: 75-86, 2007.

[132] Santamarina J.C., Fratta D. - Discrete Signals and Inverse Problems: an Introduction for Engineers and Scientists, John Wiley & Sons, Chichester, UK, 2005.

[133] Saragiotis C.D., Hadjileontiadis L.J., Panas S. M. - PAI-S/K: A robust automatic seismic P-phase arrival identification scheme: IEEE Transactions on Geoscience and Remote Sensing, 40: 1395 - 1404, 2002.

[134] Sarout J., Ferjani M., Guéguen Y. - A semi-automatic processing technique for elastic-wave laboratory data, Ultrasonics, 49: 452-458, 2009.

[135] Sarris E., Papanastasiou P. - The influence of the cohesive process zone in hydraulic fracturing modeling, International Journal of Fracture, 167: 33-45, 2011.

[136] Sass O. - Rock moisture fluctuations during freeze-thaw cycles - preliminary results derived from electrical resistivity measurements, Polar Geography, 28 (1): 13-31, 2004.

[137] Scheider I. - Cohesive model for crack propagation analyses of structures with elastic-plastic material behavior, GKSS research center Geesthacht, 2001.

[138] Schulson M., Duval P. - Creep and fracture of ice, Cambridge University Press, Cambridge, 2009.

[139] Senfaute G., Merrien-Soukatchoff V., Morel J., Gourry J. C. - Microseismic monitoring applied to prediction of chalk cliffs collapse and contribution of numerical modelling, Proceedings of International Conference on fast Slope Movements, Naples, 2003.

[140] Shao H., Shi X., Li L. - Power signal separation in milling process based on wavelet transform and independent component analysis, International Journal of Machine Tools & Manufacture, 51: 701-710, 2011.

[141] Skinner B. J. - Thermal expansion, Handbook of Physical Constants, Geological Society of America Memorials, 97: 75-96, 1966.

[142] Sleeman R., van Eck T. - Robust automatic P-phase picking: an on-line implementation in the analysis of broadband seismogram recordings, Physics of the Earth and Planetary Interiors, 113: 265-275, 1999.

[143] SMS - Cambiamenti climatici in Valle d'Aosta, Ed. SMS, Bussoleno, 2006.

[144] Sondergeld C. H., Rai, C. S. - Velocity and resistivity changes during freeze-thaw cycles in Berea sandstone, Geophysics, 72: E99-E105, 2007.

[145] Swanson P. L., Estey L. H., Boler F. M., Billington S. - Accuracy and precision of microseismic event locations in rock burst research studies, U.S. Department of the Interior, Bureau of Mines, Report of Investigation 9395, 1992.

[146] Takeuchi S., Simmons G. - Elasticity of Water-Saturated Rocks as a Function of Temperature and Pressure, Journal of Geophysical Research: Solid Earth, 78: 3310-3320, 1973.

[147] Tarantola A., Vallette B. - Inverse problems = quest for information, Journal of Geophysical Research, 50: 159-170, 1982.

[148] Thill R.E., Bur T.R. - An automated ultrasonic pulse measurement system, Geophysics, 34: 101-105, 1969.

[149] Tijssens M.G.A., Sluys B.L.J., van der Giessen E. - Numerical simulation of quasi-brittle fracture using damaging cohesive surfaces, European Journal of Mechanics - A/Solids, 19: 761-779, 2000.

[150] Timur A .- Velocity of compressional waves in porous media at permafrost temperatures, Geophysics, 33: 584-595, 1968.

[151] Todd T.P. - Effect of cracks on elastic properties of low porosity rocks, Ph.D. Thesis, B.S. University of Toronto, 1969.

[152] Toksöz M. N., Cheng C. H., Timur, A. - Velocities of Seismic-Waves in Porous Rocks, Geophysics, 41: 621-645, 1976.

[153] Valenti G. - Il permafrost in Ticino. Dati, statistiche e societá. I ghiacciai del Ticino, Ustat, 2, 2006.

[154] van Genuchten M.T.- A closed-form equation for predicting the hydraulic conductivity of unsaturated soils, Soil Science Society of America Journal, 44: 892-898, 1980.

[155] Vahaviolos S.J. - Acoustic emission: standards and technology update, ASTM special technical publication, Philadelphia, 1999.

[156] Walder J. S., Hallet B. - A theoretical model of the fracture of rock due to freezing, Geological Society of America Bulletin, 96 (3): 336-346, 1985.

[157] Walder J. S., Hallet, B. - The physical basis of frost weathering: toward a more fundamental and unified perspective, Arctic and Alpine Research, 18: 27-32, 1986.

[158] Whalley W.B., Bruce B.R., Rainey M.M. - Weathering, blockfields, and fracture systems and the implications of long-term landscape formation: some evidence from Lingen and Oksforddjokelen areas in North Norway, Polar Geography, 28: 93-119, 2004.

[159] Walsh J.B. - A new analysis of attenuation in partially melted rocks, Journal of Geophysical Research, 74 (17): 4333-4337, 1969.

[160] Wang C., Lin W., Wenk H. - The effects of water and pressure on velocities of elastic waves in a foliated rock, Journal of Geophysical Research, 80: 1065-1069, 1975.

[161] Williams P.J., Smith M.W. - The Frozen Earth, fundamentals of geocryology, Cambridge University Press, Cambridge, 1989.

[162] Wyllie M.R.J., Gregory A.R., Gardner G.H.F. - An experimental investigation of factors affecting elastic wave velocities in porous media, Geophysics, 23: 459-493, 1958.

[163] Yang Z.J., Su X.T., Chen J.F., Liu G.H. - Monte Carlo simulation of complex cohesive fracture in random heterogeneous quasi-brittle materials, International Journal of Solids and Structures, 46: 3222-3234, 2009.

[164] Yu W., Lai Y., Zhang X., Zhang S., Xiao J. - Laboratory investigation on cooling effect of coarse rock layer and fine rock layer in permafrost regions, Cold Regions Science and Technology, 38: 31-42, 2004.

[165] Zemp M., Paul F., Hoelzle M., Haeberli W. - Alpine glacier fluctuations 1850-2000: an overview and spatio-temporal analysis of available data and ist representativity, University of California Press, 2007.

[166] Zhang M., Lai Y., Li S., Zhang S. - Laboratory investigation on cooling effect of sloped crushed-rock revetment in permafrost regions, Cold Regions Science and Technology, 46: 27-35, 2006.

[167] Zhang H., Thurber C., Rowe C. - Automatic p-wave detection and picking with multiscale wavelet analysis for single-component recordings, Bulletin of the Seismological Society of America, 93 (5): 1904-1912, 2003.

[168] Zhao Y., Takano K. - An artificial neural network approach for broadband seismic phase picking, Bulletin of the Seismological Society of America, 89: 670-680, 1999.

[169] Zhou Jin-shenga, Zhou Guo-qing, Zhang Qi, Liu Zhi-qiang, Zhao Guang-si - Experimental research on evolving rules of segregation ice in artificial frozen soil, Procedia Earth and Planetary Science, 1: 544-549, 2009.

List of figures

215

218

220

221

222

List of tables

225

226